5-12-2014

Basis Function Approaches for Two Dimensional Cochlear Models

Lihua Li
University of Missouri-St. Louis, ll9n8@mail.umsl.edu

Basis Function Approaches for Two Dimensional Cochlear Models

Lihua Li
M.Phil., Computer Science, City University of Hong Kong, 2010
B.S., Computer Science, Wuhan University, 2008

A Thesis Submitted to the Graduate School a the University of Missouri – St. Louis
in Partial Fulfillment of the Requirements for the Degree
Doctor of Philosophy in Applied Mathematics

May 2014

Advisory Committee
Charles K. Chui, Ph.D.
Chairperson

Wenjie He, Ph.D.
Henry Kang, Ph.D.
Uday Chakraborty, Ph.D.

Abstract

The human cochlea possesses the amazing ability of analyzing audio signals. The structures and mechanisms behind its characteristic response to sound stimuli has been an active area of research for decades. It has been demonstrated that mathematical cochlear modeling poses a promising alternative to discover the elusive activities in an *in vivo* cochlea. However, despite the successful application of numerical methods such as the Wentzel–Kramers–Brillouin (WKB) method, finite difference method (FDM) and finite element method (FEM), the critical effects of the choice of basis functions have not been studied exclusively for the numerical solutions of cochlea models. This work presents the numerical solution procedures to two types of cochlear models using the basis function collocation approach. Accuracies and effectiveness of basis functions are evaluated by comparing simulation results with past experiment and physiological data. The time-domain solutions in response to various audio inputs are also shown. The cochlear model demonstrates sound processing abilities which are qualitatively comparable to physiological data. It is hoped that the results in this work would help in laying the foundation for future cochlear model solutions and cochlea-based audio signal processor.

Acknowledgement

First and foremost, I would like to express my deep gratitudes to my dissertation supervisor Dr. Charles K. Chui. As a prestigious professor in Applied Mathematics, you have persistently provided me research thoughts and technical insights on my dissertation topic. Without your help, my Ph.D. research would be mission impossible.

Second, I would like show my great appreciations to the professors and secretaries of the Mathematics and Computer Science department, for giving me helps on my academic journey. In particular I would like to thank Dr. Wenjie He for the years of support on my study and life.

Third, I am deeply indebted to Dr. Jie Chen from the Argonne National Laboratory in Chicago, for offering me the summer intern opportunities. I learned at lot in new math tools and programming skills from you.

Fourth, I would like to thank my friends during my stay in St. Louis. Special thanks go to Michael Young, for the sincere friendship you offered over these years.

Last but not least, I would like to thank my mother for her continued guidance and support.

List of Abbreviations

The following table describes the list of abbreviations and acronyms used throughout the thesis. The page number on which each one is defined or first used is also given.

Abbreviation	Meaning	Page
WKB	Wentzel–Kramers–Brillouin (method)	i
FDM	finite difference method	i
FEM	finite element method	i
OHC	outer hair cell	1
OW	oval window	6
RW	round window	6
BM	basilar membrane	6
RM	Reissner's membrane	6
SV	scala vestibuli	6
ST	scala tympani	6
SM	scala media	7
OC	organ of Corti	7
IP	inner pillar cell	7
OP	outer pillar cell	7
IHC	inner hair cell	7
TM	tectorial membrane	8
CP	characteristic place	9
2TS	two-tone suppression	15
FF	feed-forward	17
RBF	radial basis function	22
MQRBF	multiquadric radial basis function	23
GRBF	Gaussian radial basis function	26
QS	quadratic spline	29
CS	cubic spline	29

Table 1: Abbreviations

Contents

List of Tables

List of Figures

Chapter 1

Introduction

The sense of hearing for human is extraordinary, for its ability to perceive sounds with wide range of magnitude, to distinguish individual frequencies, and to maintain satisfactory performance in adverse situations. It is believed that the cochlea plays an crucial role in the exceptional performance of the human auditory system. Resided in the bony labyrinth, the cochlea converts the fluctuation in mechanical sound pressure into electrical spikes in the auditory nerve, decomposing the audio signal by frequency, boosting up weak signals, attenuating high-level sounds, and creating interferences between different frequencies. For decades, physiological researches have been conducted to reveal the elusive mechanism behind the sound analysis capability of the cochlea. However, medical experiments often encounter great difficulties for the minuscule scale and the delicate structure of the cochlea.

Mathematical cochlear models provides a promising alternative to unlock the mysteries of the biological cochlea. Combining results in recent physiological measurements, and numerical techniques such as the WKB method and the finite difference method, a large extent of the cochlea mechanics have been revealed. In the mammalian cochlea, different frequencies of the input signal incites different locations of the basilar membrane to vibrate. The vibrations are then enhanced and reshaped by the nonlinear cochlear amplifier, resulting in sensitive audio perception and acute frequency selectivity. It is commonly believed that the cochlear amplifier originates from the the electro-motilities of the outer hair cells (OHCs) residing in the organ of Corti. Active cochlear models that incorporate OHC feedback mechanisms are proposed to give responses qualitatively matching to physiological data.

As a variety of numerical techniques has been applied to find the solutions of mathematical cochlear models, the effects of different basis functions to simulation results are rarely studied despite their critical role in spatial discretization. By the proper

selection of basis functions and the corresponding discretization scheme, efficient solutions can be obtained while the numerical errors of the models are minimized. Such research lays the foundation for future studies of cochlear modeling where complex domain geometry and convoluted physical mechanisms are incorporated.

The contribution of this work is two-fold. First, finding out the best strategy of selecting the basis functions and the discretization scheme for solving cochlear models. Various basis functions are applied in the solution of the spatial cochlear model, and properties such as solution accuracy and stability are evaluated to determine the suitability of each basis functions. Second, investigating the output of the cochlear model in response to different types of audio signals. The dynamic and static states of the system are studied, and the results are compared to past simulation and physiological data.

1.1 Road Map

The following describes the organization of this thesis.

1.1.1 Chapter 2: Background

Chapter 2 is dedicated to introducing the background of the present work. The first part describes the anatomy structure and the mechanics of the human cochlea. The general work mode, the micro-structures, and the characteristic behaviors of the cochlea are shown. The second part is focused on the past efforts in cochlear modeling and the solutions to cochlear models. Classical cochlear models such as the passive model and the OHC feedforward model are discussed, and solutions obtained by various numerical methods are listed.

1.1.2 Chapter 3: Objectives and Approaches

Chapter 3 describes the objectives and approaches for this research. The first part states the objectives of this research, defining the scope of the thesis. The second part describes the types of basis functions used in the solutions of cochlear models. Their way of construction, numerical properties, and the corresponding discretization scheme are explained. The third part describes the temporal discretization technique used in time domain experiments.

1.1.3 Chapter 4: Cochlear Models and Simulations

Chapter 4 presents the mathematical cochlear models and their experiment results. The first part gives the formulation of two types of cochlear models: the spatial model and the temporal-spatial model. The second part presents the experiment results of the spatial model, where the discussions are focused on the effects of different basis functions and spatial discretization schemes. The third part shows the experiment results of the temporal-spatial model, with an emphasis on comparing the model performance to physiological data.

1.1.4 Chapter 5: Future Work

Chapter 5 discusses possible directions for future development of the present work.

1.1.5 Chapter 6: Conclusion

Chapter 6 concludes the thesis with reviews on important findings.

Chapter 2

Background

2.1 The Cochlea

2.1.1 Cochlear Anatomy

The human peripheral auditory system contains three parts: the outer ear, the middle ear, and the inner ear (i.e. the cochlea). They play different roles in the process of sound before the audio signals reach the central auditory system located at the temporal lobe of the human brain.

The outer ear and the middle ear

The outer ear consists of the pinna and the external auditory canal that leads to the eardrum. The main function of the outer ear is to magnify sound pressure for later process. As sound waves approach the pinna, the energy is condensed and funneled down to the ear canal due to the conical shape of the pinna. And because the ear canal is basically a tube filled with air, the sound wave is further amplified as they resonate within the canal, similar to how sound resonates in musical wind instruments.

The middle ear resides behind the eardrum, which divides the middle ear from the outer ear. The middle ear cavity contains a chain of three tiny ear bones: malleus, incas, and stapes. These bones are also called the ossicles. The function of the middle ear is to overcome the difference of acoustic impedance between the eardrum and the sensor port of the inner ear. Acoustic impedance Z_{A} is defined as the ratio of acoustic pressure P to volume velocity VA, where V is the velocity and A is the cross-sectional area:

$$Z_A = \frac{P}{VA}$$

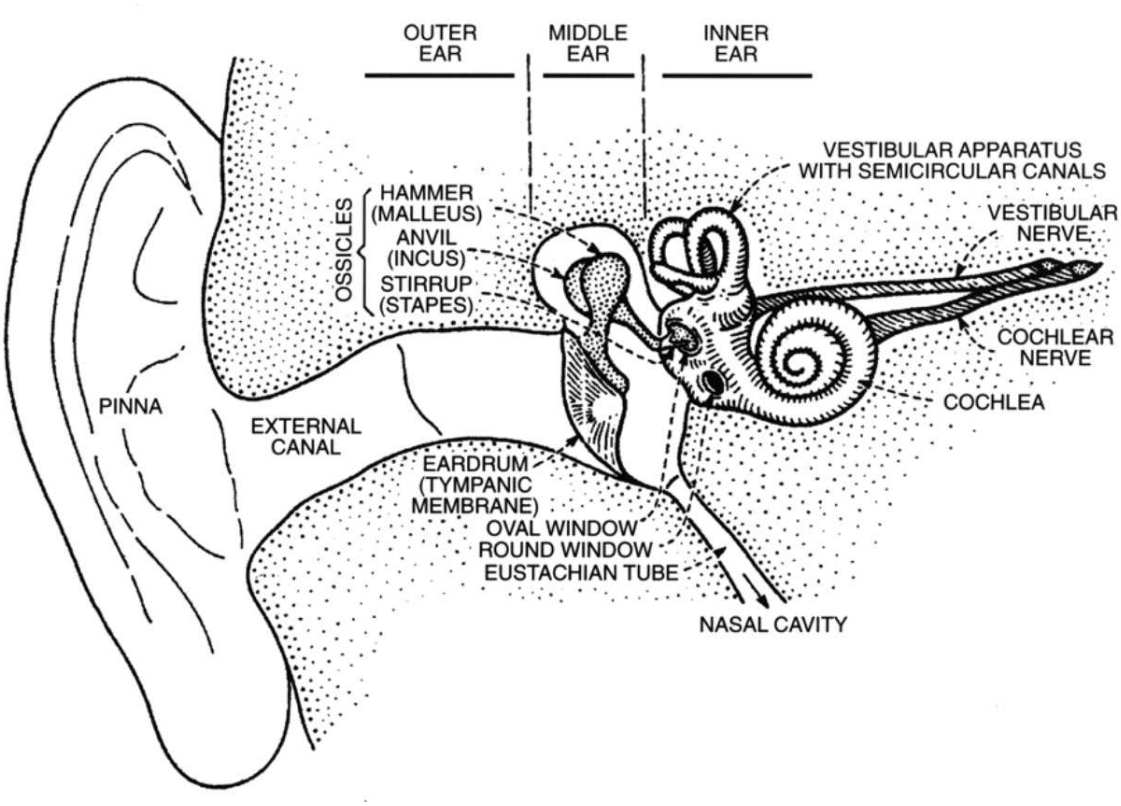

Figure 2.1: Human ear.
The human ear is generally divided into the outer, middle, and inner regions. The outer ear has the simplest structure of the three, containing only the pinna and the external auditory canal. The middle ear is slightly more complex. It comprises of the middle ear cavity, the Eustachian tube, and the ossicular chain that connects to the inner ear. The inner ear is a bony labyrinth filled with fluid. The auditory part of the inner ear is the cochlea, a snail-like structure that transduce mechanical vibrations to electrical signals to be transmitted to the brain. Image adapted from [20].

The passing of sound energy will be highly ineffective without matching the impedance of two conducting media. Especially when passing sound from air (ear canal) to water (cochlea). With a 1:3880 impedance ratio, most of the sound energy will be lost due to reflection. The impedance matching is done by the surface area discrepancy between eardrum and the stapes footplate: the stapes footplate is much smaller than the eardrum. If we assume the velocity of the eardrum and the stapes are the same, and the force acting on both are also equal, a 62:1 enhancement would be produced due to the area difference [26].

Apart from the enhancement of sound pressure magnitude, the outer ear and the middle ear also changes the energy distribution in sound frequencies. Studies of the energy transfer function can be found in [77].

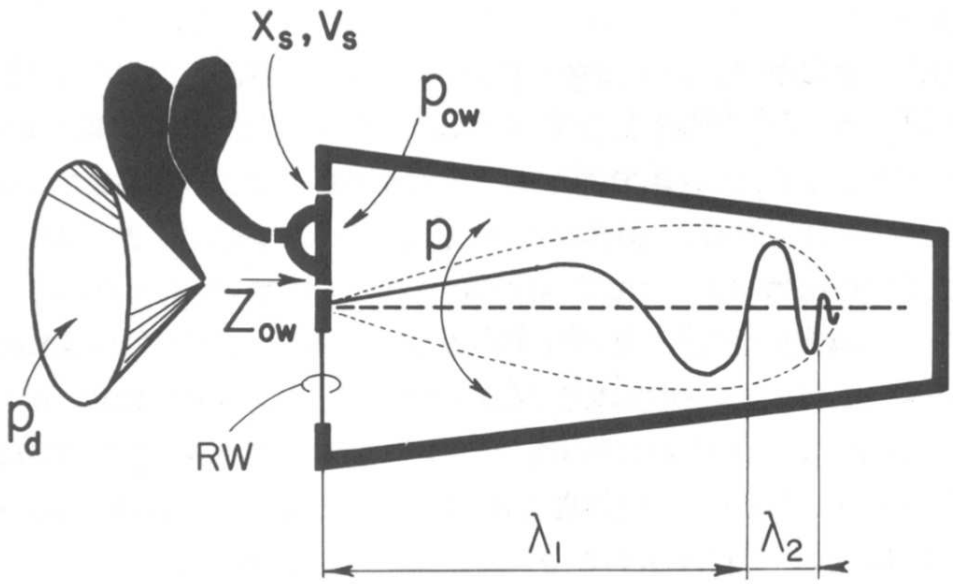

Figure 2.2: Sound propagation in the ear.
The air pressure at the eardrum (P_{d}) is passed down the ossicular chain to become the displacement (X_{s} and velocity V_s) of the stapes. The stapes is connected to the oval window of the cochlea. The motion of the stapes creates a pressure (P_{OW}) at its footplate matching the cochlea impedance Z_{OW}. The disturbance at the oval window generates a pressure difference P across the cochlear partition, which in turn creates a traveling wave in the cochlear fluid along the cochlear partition. This graph also depicts two full cycles of the traveling wave with different wavelengths, λ_1 and λ_2. The peak of the traveling wave is located at the short wavelength section. The fluid pressure in the cochlea is released at the round window, marked as RW. Image adapted from [10].

The Inner Ear

The inner ear consists of three parts: the semicircular canals, the vestibule, and the cochlea. The cochlea is a small spiral-shaped cavity in the bony labyrinth. It is the only part responsible for sound perception.

The cochlea is similar to a tube coiled increasing sharply on itself, turning approximately $2\frac{5}{8}$ times in humans. The cochlea terminates blindly in its third turn at the apex. If we uncoil the cochlea into a long tube, it is approximate 35 mm in length. The basic structure of the cochlea is shown in the cross-sectional sketch of a radial slice of a guinea pig, taken at the second turn (Figure 2.3). The cochlea fluid duct is separated into three chambers by the basilar membrane (BM) and the Reissner's membrane (RM). The scala vestibuli (SV, the upper chamber in Figure 2.3) runs from the oval window to the apex. The scala tympani (ST, the lower chamber in Figure 2.3) runs from the round window to the apex. SV and ST are connected to

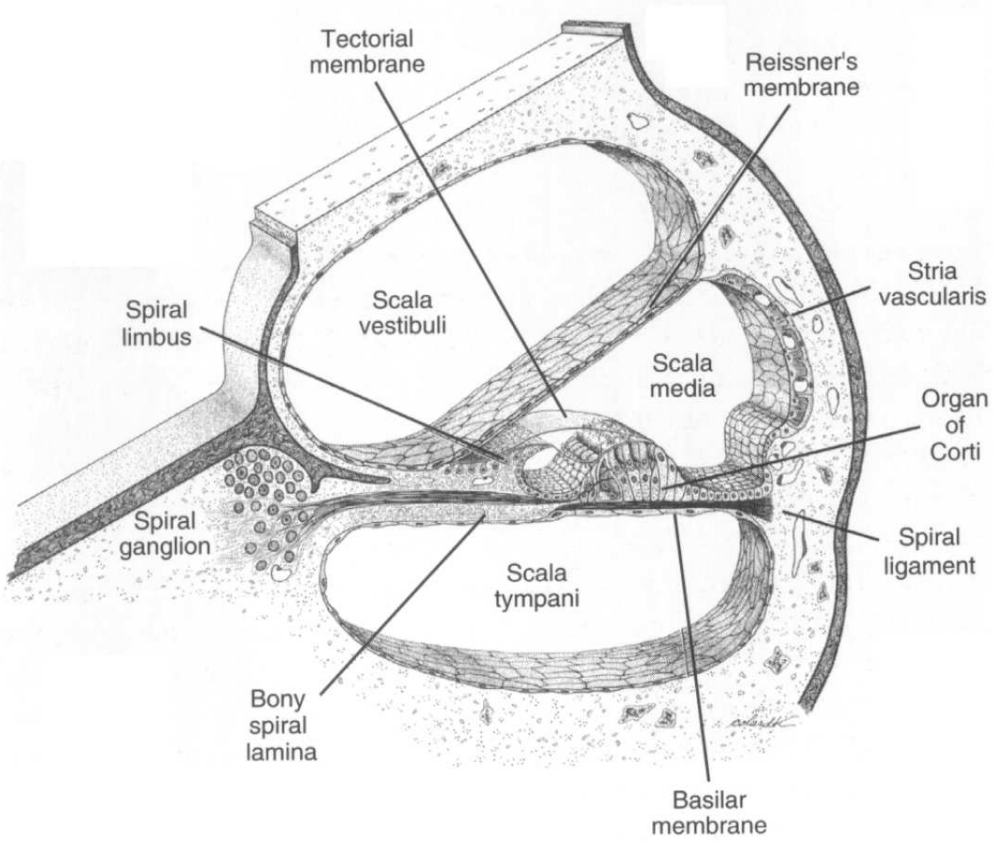

Figure 2.3: Radial segment of the cochlear duct.
The cochlear duct is divided into three fluid-filled chambers: scala vestibuli, scala media, and scala tympani — by the Reissner's membrane and the basilar membrane. The organ of Corti resides on the basilar membrane. To the left of this graph is the modiolus, the axis of the cochlear spiral. Image from [19].

each other at a small opening at the apex. The scala media (SM), also named the cochlear sac, is an enclosed chamber bounded by RM and BM. The organ of Corti (OC) resides on BM inside SM.

The organ of Corti is a sensory organ containing both sensory cells and supporting cells. The chief structural cells in the OC are the inner pillar cells (IP) and the outer pillar cells(OP). As shown in Figure 2.4, one IP cell and one OP cell, combined with a small portion of the BM, form a relatively rigid stricture called the Corti arch. The array of IP cells and OP cells runs longitudinally along the cochlear duct, thus the Corti arches form a tunnel through the cochlear sac, called the tunnel of Corti. Other structural cells include the Deiters' cells (D), Hensen cells (H), and Claudius(C) cells.

There are two types of sensory cells: the inner hair cells (IHCs) and the outer hair cells (OHCs). They serve very different purposes. The IHCs are responsible

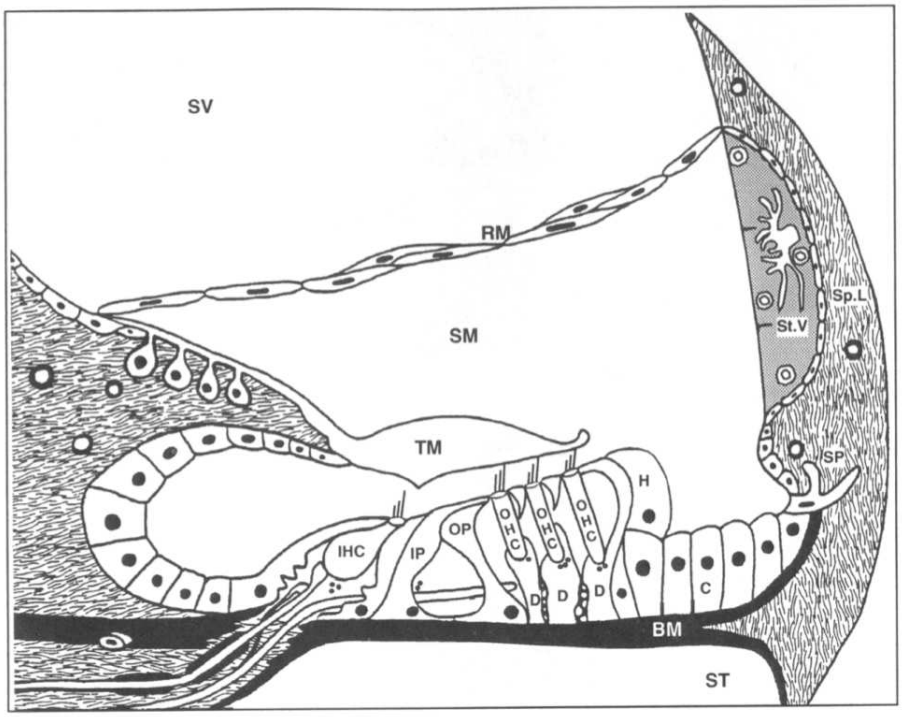

Figure 2.4: Organ of Corti.
The organ of Corti resides on the basilar membrane on the side of scala media. It contains both sensory and supporting cells. The array of inner pillar (IP) cell, outer pillar (OP) cell, and a small portion of the BM form the tunnel of Corti. Other supporting cells such as Deiters' cells (D), Hensen cells (H), and Claudius cells (C) are also shown in the graph. Image from [63].

for transducing the mechanical oscillation of the cochlea fluids into electrical signals. Information such as timing, intensity, frequency composition, and other physical properties are encoded to be transmitted to the central nervous system via afferent axons of spiral ganglion cells. Such process is triggered by the the movement of the stereocilia at the top of IHCs. The IHCs are encircled by supporting pillar cells, and thus they are immobile to the OC structures.

The OHCs are connected to the efferent axons originated from the brain stem. It is believed that the OHCs serve as the amplifier of BM movements. Unlike the IHCs whose stereocilia are surrounded by cochlear fluid, OHCs' stereocilia are embedded in the tectorial membrane (TM). Also, the OHCs are not contacted with other cells on their sides; they are only supported at their bases by Deiters' cells (D) and at their apexes by the reticular lamina. Such a structure is pertinent to the motility of OHCs.

2.1.2 Cochlear Mechanics

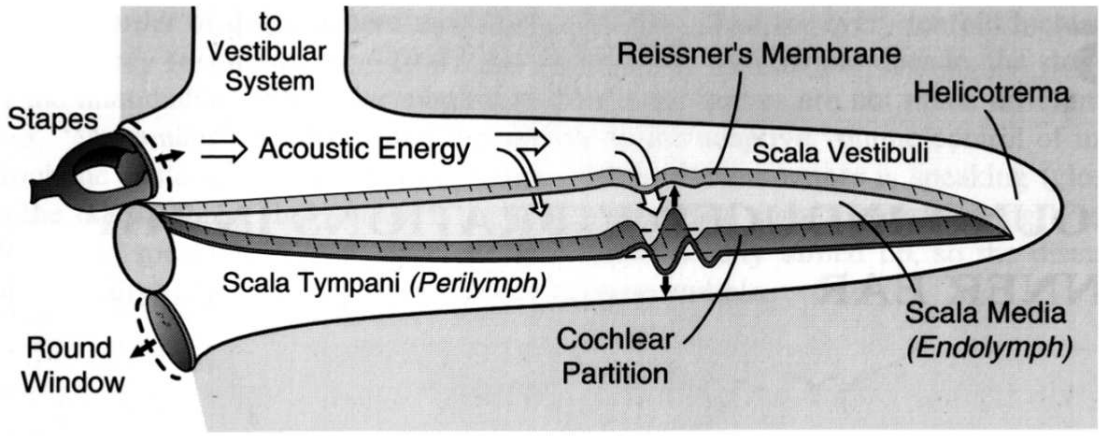

Figure 2.5: Basilar membrane vibration.
This graph illustrates how an uncoiled cochlea react to sound stimuli. The pressure input from the oval window (stapes footplate) travels to the apex and to the round window. Due to the incompressibility of cochlea fluids, the volume displacement of the round window is the same as that of the oval window. As the acoustic energy is carried along the cochlea duct, it is absorbed by the BM where the resistance to the pressure is minimum. As a result, the BM is driven up and down by the pressure diffrence across it. Image from [26].

Sound stimuli are forwarded to the cochlea via the stapes footplate at the oval window. Because the cochlear fluids are incompressible (they are mainly water in composition), the pressure travels along the cochlear duct to the apex, then back along the duct to the round window. The pressure difference between the two sides of the BM drives the membrane into motion. The BM is made of fibers aligned in radial directions. These transverse fibers are at one side inserted into the the bony spiral lamina, and at the opposite side into the spiral ligament; it is commonly believed that these fibers do not have strong longitudinal coupling [18]. The BM is narrower and thicker in the base than in the apex, resulting in a gradient of stiffness. Because of such physical property, the basal end of the BM resonates with sound stimuli of higher frequency, while the apical end of BM resonate with sound stimuli of low frequency. Given a sound input of certain frequency, the BM movement achieves the maximum amplitude at a certain fixed location corresponding to the input frequency. That location is called the characteristic place (CP) of the corresponding frequency; likewise, the corresponding frequency is called the characteristic frequency of that location [56, 66, 69]. Most of the acoustic energy carried by the cochlear fluids is absorbed by the cochlear partition close to the CP.

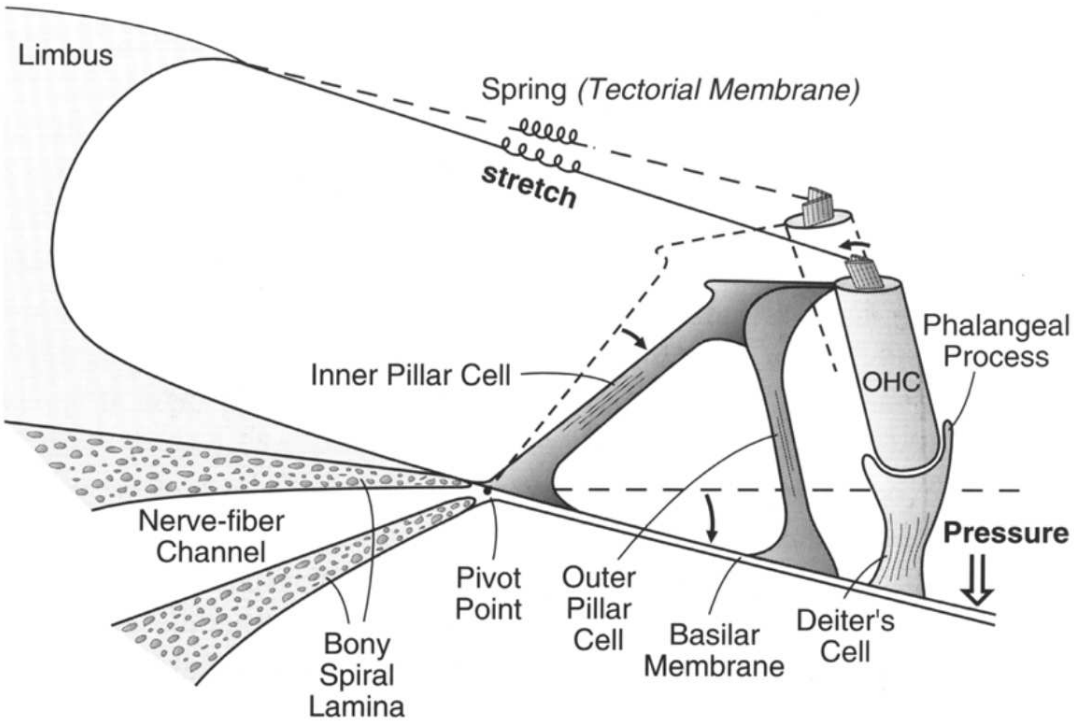

Figure 2.6: Deflection of OHC stereocilia.
The motion of the basilar membrane (BM) causes the sterocilia of the outer hair cells (OHCs) to deflect, as the organ of Corti (OC) is driven into motion with the BM. This diagram shows the effect of a downward BM motion. Because the rigid Corti arch formed by pillar cells, the downward BM motion cause the OHCs to rotate clockwise around the pivot point, leading to the deflection of the stereocilia in the counterclockwise direction and the hyperpolarization of the OHCs. Through a similar mechanism the upward BM motions cause the OHCs to depolarize. Image from [26].

By the observation of von Békésy in [72], sound stimuli cause a mechanical traveling wave to form both in the cochlear fluid and on the BM: a pressure wave in the cochlear fluids, and a displacement wave on the BM. Compared to the acoustic wave, which traverses the entire cochlea in just a few microseconds [57], the mechanical traveling wave is much slower. At the basal end, the traveling wave has a larger velocity and a longer wavelength. The velocity and wavelength is then greatly diminished as the wave approaches to the characteristic place. Soon after its magnitude peaks at the CP, the traveling wave sharply decays as most of its energy is acquired by the BM.

The up-and-down motion of BM causes the stereocilia to deflect through the structural organization of the organ of Corti. See Figure 2.6. The arches of Corti formed by relatively rigid, triangularly placed pillar cells retain its shape as the BM is

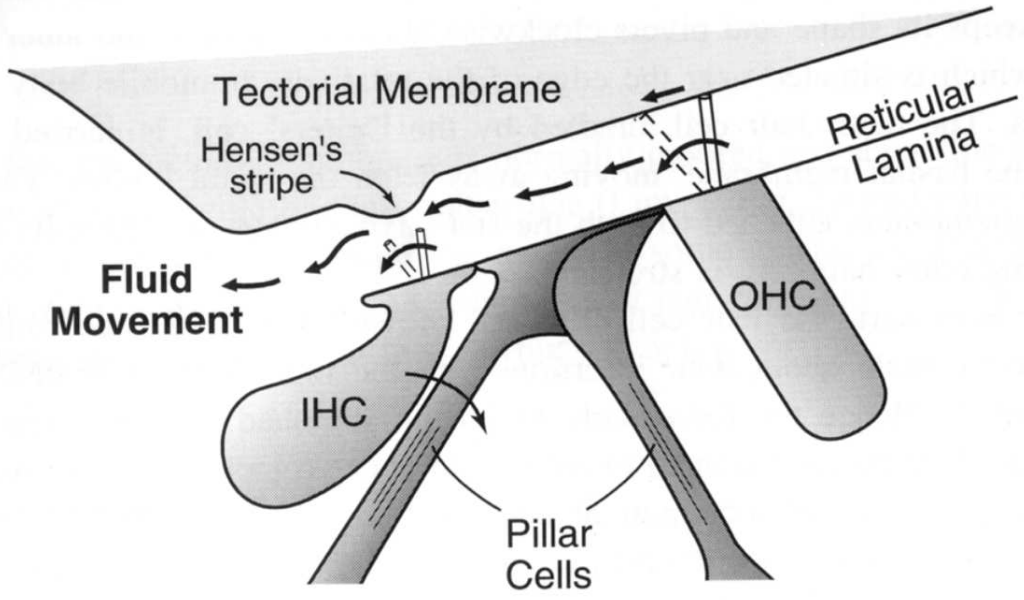

Figure 2.7: Deflection of IHC stereocilia.
As the stereocilia of the OHCs are deflected due to BM motion, the fluid in the gap between the stereocilia and the tectorial membrane is caused to flow, which deflects the stereocilia of the IHCs in the same direction as that of the OHCs. Image from [26].

pushed downward by fluid pressure, pivoting clockwise about the foot of the IP cells located close to the edge of the immobile bony spiral lamina. The OHCs, supported by the Deiters' cell, are displaced to move away from the spiral limbus. Because the OHCs have their stereocilia embedded in the tectorial membrane at the top of the organ of Corti, the displacement of OHCs causes a shear force between the recticular membrane and the tectorial membrane. As a result, the stereocilia are deflected counterclockwise with downward BM motion, resulting in a forward mechanoelectrical transduction where the mechanical forces creates a electrical transduction current in the OHCs. The OHCs are depolarized by the influx of tranduction current. The resultant change in transmembrane receptor potential provides input to OHCs motor activity.

Another transduction process takes place at the IHCs. See Figure 2.7. As the deflection of the stereocilia of OHCs causes displacements of fluids between the tectorial membrane and the recticula lamina, the stereocilia of the IHCs are bent with the fluid motion since they are not attached to the tectorial membrane [42]. Actually, the IHC stereocilia are lined up in a row perpendicular to the flow of fluid, helping the stereocilia to be effectively deflected by the uninterrupted fluid motions [26]. The stereociliary deflection result in a transduction current. However, unlike the

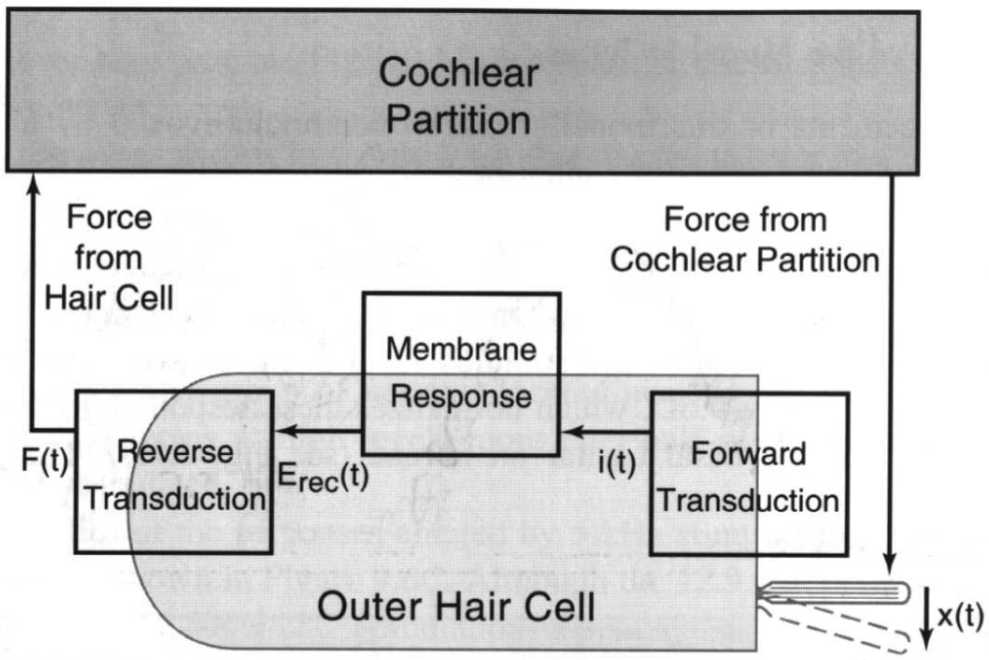

Figure 2.8: Feedback System with Outer Hair Cell Electromotility.
This figure illustrates the general feedback mechanism of BM due to the OHCs, also called the cochlear amplifier. The movement (or force) of the cochlear partition deflects the sterecilia of the OHCs, generating a transduction current $i(t)$. The current in turn creates the receptor potential $E_{\text{rec}}(t)$ which causes the OHCs to shrink or expand, changing its length. As a result, the length changes of the OHCs exerts a force $F(t)$ back onto the BM, completing the feedback loop. Image from [26].

transduction current in OHCs, the IHC transduction does not cause cell motility, but instead cause the neurotransmitter to release at the IHC-spiral ganglion cell synaptic interface.

Cochlear Amplifier

In vivo cochlea serves as a excellent frequency analyzer with remarkable acoustic sensitivity and high frequency selectivity. The measurements performed upon dead and living cochlear reveals a significant difference in vibration amplitude/velocity and frequency tuning, which strongly suggests the existence of a localized feedback mechanism inside the organ of Corti [9]. Such feedback mechanism, called the cochlear amplifier, enhances the sensitivity and tuning of the cochlea. The characteristics of a living cochlea is therefore a combined effect of the cochlear amplifier and the passive frequency tuning of the BM.

It is widely believed that the amplifying agent of the cochlear amplifier are the

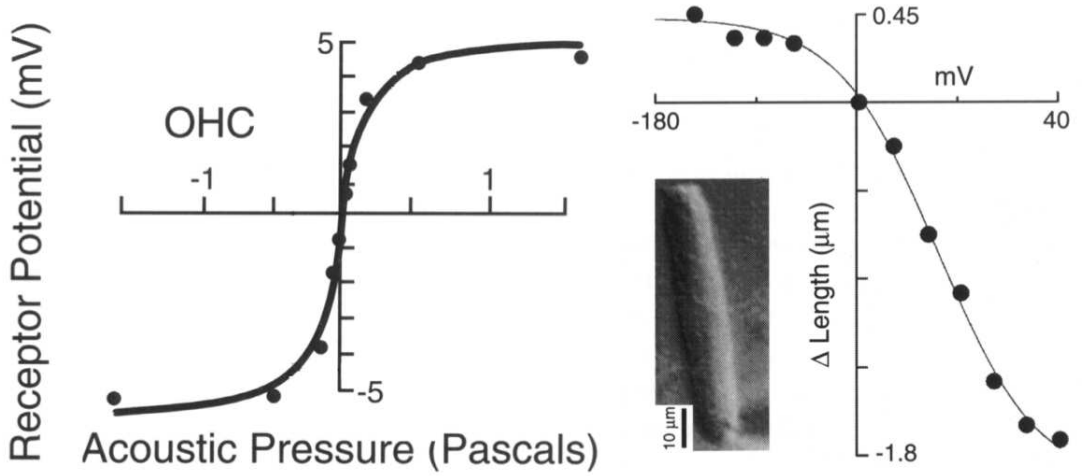

(a) (b)

Figure 2.9: OHC nonlinearity.
(a) The $\mathcal{S}$-shape curve showing the compressive growth rate of outer hair cells' receptor potential with respect to increase of acoustic pressure [59]. (b) The compressive relationship between changes of outer hair cell's body length with respect to various transmembrane voltage steps [61]. Hyperpolarization causes the cell to expand, while depolarization causes the cell to contract. Inserted image shows an outer hair cell with length reference.

OHCs, due to their ability to change cell lengths given acoustic stimuli [2]. The speed of OHC electromotility is observed to be as high as 24 kHz [7]. The magnitude of cell length change is a few percent of cell's full length, which is comparable to the magnitude of acoustic BM vibrations [26]. As the OHCs expand or contract due to electromotility, a fast motile force is exerted to the supporting Deiters' cells, which in turn carry the force onto the BM to change its motion.

The cochlear amplifier is commonly considered as a positive feedback system onto the BM motions. See Figure 2.8. The OHCs transduction process contains forward and reverse mode. Contrary to the forward transduction discussed in previous sections, the reverse transduction describes the induced mechanical forces by electrical cell membrane voltage—an electromechanical process. However, it is still largely unknown how exactly the OHC exert feedback motile force so that the BM exhibits amplification in magnitude and frequency selectivity.

Cochlear Nonlinearity

The OHCs have been discover to possess a saturation property, resulting in a nonlinear cochlear response. The measured receptor voltage for OHCs grows with the input

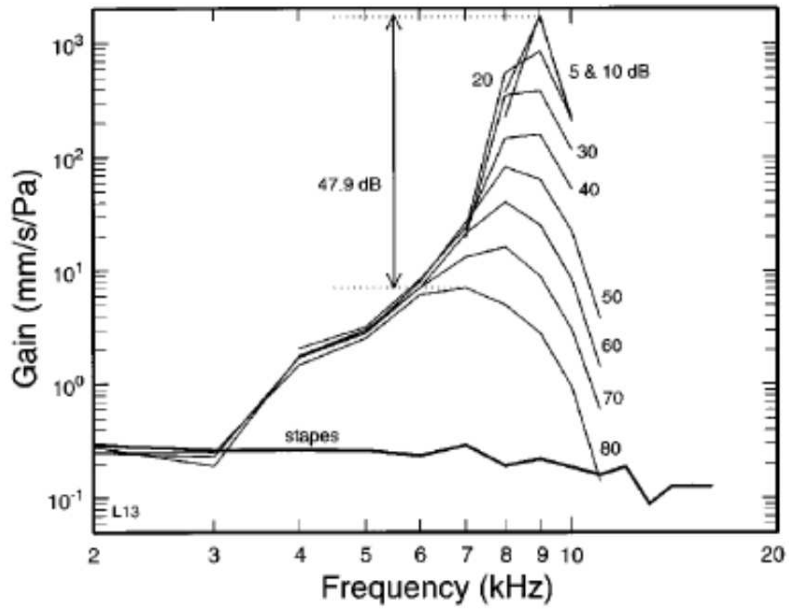

(a)

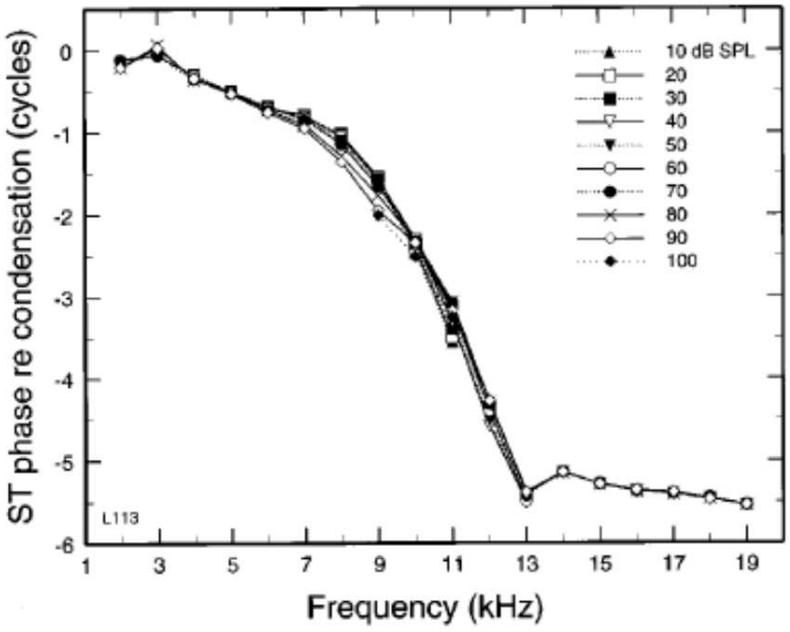

(b)

Figure 2.10: Nonlinear compression to input sound level.
The cochlear response to various input intensity is compressive. (a) Isointensity curves showing the response of the BM given input signals of various frequencies (abscissa) and intensity (parameter, in dB SPL). The average motion of the stapes is plotted as a line at the bottom. (b) Phases of the BM response towards various input frequencies. Image adapted from [58].

sound pressure in a compressive way, giving a $\mathcal{S}$-shaped curve in Figure 2.9a [60, 11]. Likewise, the change of OHC cell body lengths saturates with transmembrane potential in Figure 2.9b. If we assume the BM displacement is proportional to the input sound pressure, and the change in a OHC length is proportional to its receptor potential change, it can be derived that the OHC's electromotility force saturates with respect to the magnitude of the input sound stimuli.

The *in vivo* cochlea exhibits nonlinear responses to sound stimuli. One of the most significant nonlinear phenomena is the compression of high-level sounds. The human ear is capable of perceiving sound signals of a large range of magnitudes. According to [68], the lightest sound that human can perceive (0 dB) is six-order of magnitude smaller in sound pressure compared to a rock-and-roll concert (120 dB). It is observed that acoustic signal with small magnitude are greatly amplified by the cochlea—high amplification gain, while the high-level input are not amplified almost at all—low amplification gain. See Figure 2.10. The cochlear amplifier automatically attenuates the amplification gain as the input intensity increases.

Another nonlinear cochlear phenomenon is two-tone suppression (2TS), which means the cochlear response to one pure-tone signal (the probe, measured at the corresponding CP) is suppressed by the presence of another loud tone (the suppressor). One example for that phenomenon is a person would have difficulties hearing conversations if loud music is played at the background. 2TS can be detected in the BM's mechanical motion, in IHC receptor potential, and in the electrical discharges on the auditory nerve [58]. Although it is still debatable whether the 2TS phenomenon detected in IHCs and in the auditory nerve is a direct result of the suppressed BM motions, it is believed that the suppression in BM motions is resulted from the saturation of OHC motility forces [57].

Studies of 2TS reveal that the suppression is both dependent on intensity and frequency. See Figure 2.11. For a weak probe tone and a strong suppressor tone, the response to the probe tone is reduced further. Such a reduction is more insignificant when a strong probe tone is used. Consequently, the presence of a moderately strong suppressor tone linearizes the response to a probe tone.

2.2 Cochlear Modeling

The study of cochlear modeling has a long history [1, 13], and the existing models are constantly updated by experiment results. Since the discovery of OHC electromotility in mammalian cochlea [2], one of the main focus of cochlear modeling is to

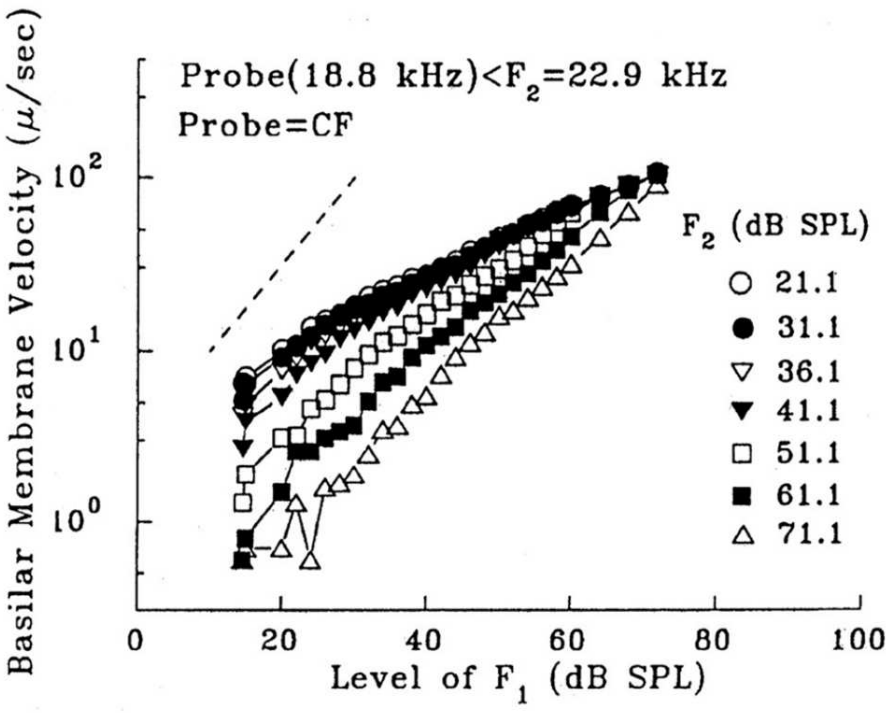

Figure 2.11: Two-tone suppression in live cochlea.
Two-tone suppression demonstrates nonlinear characteristics with varying suppressor intensity. The experiment was carried out with a probe tone $F_1 = 18.8$ kHz, and a suppressor tone $F_2 = 22.9$ kHz. As the the suppressor intensity is increased to 71.1 dB SPL, the BM response to the probe tone grows almost linearly. These data were measured from Guinea pig cochlea in [53].

incorporate the activeness of OHCs into the overall model so as to reproduce characteristic cochlear behaviors. However, due to the difficulties to perform medical experiments on live cochlea, the precise mechanism behind the cochlear amplifier is largely unknown. Another focus of cochlea modeling is to include mechanical properties produced by the micro-structures of the organ of Corti. The models for OHC motility and organ of Corti micro-mechanism are developed hand-in-hand, as it is commonly believed that the OHC motile forces are transmitted onto the BM via the complex organization of the organ of Corti. Despite many different cochlear models were raised over the decades, one goal is shared for all these individual developments: trying to simulate BM responses which are comparable to physiological data.

Cochlear models incorporating OHC motility are commonly called active cochlear models, whereas cochlear models without OHC motility are called passive cochlear models [49]. The analytical and numerical solutions of active cochlear models help

bridging the understanding of how the OHC motility force contributes to the amplifying and sharpening the traveling waves along the basilar membrane, as well as to the nonlinear response of the cochlear to different sound intensities. [27, 22, 46, 23, 33, 50, 25, 41, 67] describe a number of active cochlear models that combine the OHC motility into cochlear macro-mechanics.

It is commonly believed that the BM fibers only weakly couple to their adjacent neighbors through cochlear fluids due to their radial orientation towards the modiolus [12, 18]. See experiments performed by Voldrich [70], Neidu et. al. [47], and von Békésy [72] for medical researches on the longitudinal stiffness of the BM fibers. Most of the cochlear models neglect the longitudinal stiffness of the BM since it is insignificant compared to the transverse stiffness. Several cochlear models implemented the longitudinal coupling of BM fibers trying to produce more realistic cochlear responses; see the work of Hubbard [33] and Jaffer et. al. [34].

As pointed out by Voldrich [71], the OHCs are arranged so that motile force generated by a OHC is exerted to neighbor BM segments, effectively coupling the adjacent BM fibers longitudinally. Some cochlear models took into consideration the basal tilt of OHCs when modeling the feedback mechanism [27, 22, 46, 41, 67]. A example is the feedforward (FF) micro-mechanics OHC model proposed in [46], where the FF model is joined with a three-dimensional, fourth order plate model of the BM. In [27], the tectorial membrane was model as an additional resonant system altogether with the FF model to create more realistic BM motions as compare to physiological data.

The formation of the FF model is still debatable, as Karavitaki and Mountain pointed out that the feed-forward mechanism is in contradiction to experiment data, where the longitudinal component of OHC motion in apex is observed to be ten times smaller than the radial component [37]. Given the limitations in model complexity and the lack of understanding of the amplification mechanism, the FF model still offers a favorable compromise between modeling constraints and agreements to physiological data.

The cochlear nonlinearity is commonly attributed to the nonlinear behaviors of the OHCs [8]. OHC nonlinearity has been included in some cochlear models in order to reproduce nonlinear cochlear behaviors such as compressive growth to sound intensities, two-tone suppression, and otoacoustic emissions [26, 30, 24, 4, 32]. Most of the nonlinear cochlear models adopted nonlinear functions (such as the hyperbolic tangent) as a source of nonlinear elements.

2.2.1 Solutions to Cochlear Models

The cochlear models are usually given as a set of partial differential equations. Although analytical solutions can sometimes be derived out of simple cochlear models, the incorporation of OHC electromotility into the overall models drastically increase the complexity of cochlear models, rendering the analytical solutions very difficult to obtain. Numerical methods are commonly used in cochlear modeling and simulations. The following gives a general survey on three popular types of numerical methods: the WKB method, finite difference method, and finite element method.

The WKB method (WKB approximation) is a technique to approximate solutions to linear partial differential equation with spatially varying coefficients. Named after three physicists: Wentzel, Kramers, and Brillouin, the method was developed in 1926 as an approach to solve partial differential equations such as the Schrödinger equation. Steele and Miller applied the WKB method in solving a two-dimensional cochlear model [64]. Another example is the work of Lim and Steele in [46], where a three-dimensional nonlinear active cochlear model was studied. More application of the WKB methods can be found in [74, 65, 15, 46].

The finite difference method (FDM) approximates solutions to differential equations by constructing a linear system in which differential operators are replaced by finite difference equations. Such a technique works particularly well if the domain of the problem has a rectangular shape. Neely [48] solved a two dimensional, linear passive cochlear model using FDM. A model with added active element (negative damping) was later solved in [51], which demonstrates improved frequency selectivity. An alternative to FDM is the finite element method (FEM), which grants the flexibility to use arbitrary discretization mesh. An example of cochlear modeling using FEM is the work of Kolston and Ashmore [40]. More examples of the FDM and FEM methods can be found in [55, 65, 17, 73].

Chapter 3

Objectives and Approaches

3.1 Objectives

The objectives of our research in this thesis is outlined as follows:

1. First, we demonstrate the solutions to two types of two-dimensional cochlear models using basis function approaches. The cochlear models have been previously solved by techniques such as the WKB method, FDM, and FEM, where the focus was mainly on model and mesh specification. Although the types of basis function play a critical role in approximation scheme, their effects and constraints in application were rarely studied. In this work, basis function collocation methods are adopted as the solution technique. The detailed steps to derive numerical solutions with various types of bases are shown, and the strength and weakness of different basis functions are discussed by comparing with past experiments and physiological data. The results of this work should help in laying the foundation of future construction of cochlear model solutions, serving as guidelines for better selection of basis functions and proper solution scheme.

2. Second, we test the output of a cochlear model in response to different types of audio input signals. The cochlear model to be studied was presented in [39], which provides a drastic simplification of the human cochlear with assumptions to compromise between complex biological structure and limited computational constraints. Although the model was successfully solved by FDM, the performance of the solution is unknown when more generic selection of basis functions are applied. Likewise, physical phenomenon arise from the temporal-spatial solution requires proper interpretation. The study of this cochlear model sheds

lights to the intriguing characteristics of the biological cochlea, which in turn inspire future development of cochlear models to better comply with physiological observations.

3.2 Collocation Methods for Linear Boundary Value Problem

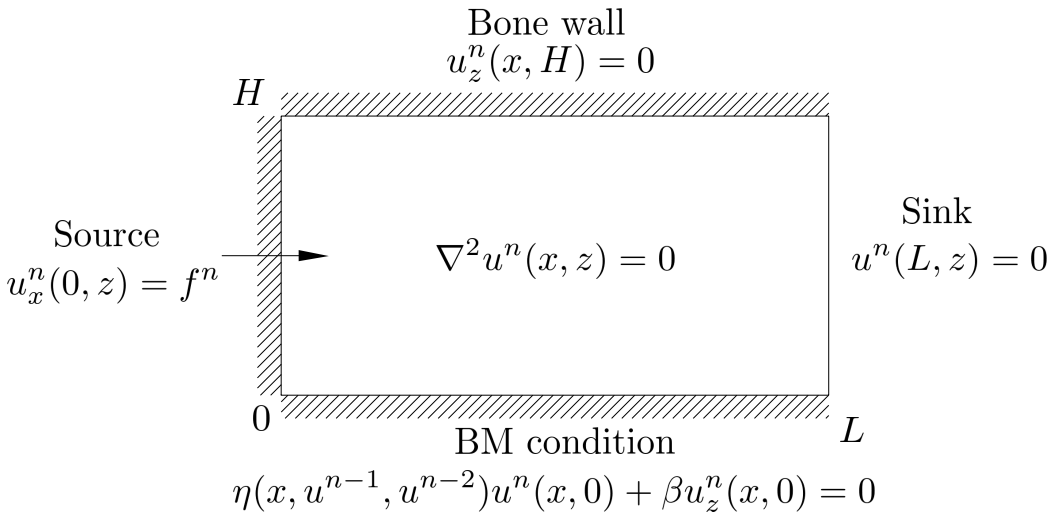

Figure 3.1: Boundary value problem of the cochlea model.
The cochlea model is defined on a rectangular domain $[0,L]\times[0,H]$ as a set of partial differential equations. After temporal discretization, the model is reduced to a well-posed, elliptic boundary problem with Dirichlet and Neumann boundary conditions. $n=2,3,\cdots$ represents time steps for temporal discretization.

To facilitate the discussion of our solution methodology, an abstraction of the cochlear model used in this thesis is shown in Figure 3.1. By denoting superscripts as the time step in temporal discretization, the cochlea model is reduced to a linear boundary value problem defined on a rectangular domain $[0,L]\times[0,H]$. In this thesis, we only consider the linear model of the homogeneous Laplace's equation in the interior domain Ω. The boundary of the domain, denoted as $\partial\Omega$, is governed by a combination of Dirichlet and Neumann boundary conditions. The input of the system is given as a Neumann boundary condition at the left boundary $x=0$ with sound pressure f^n at the nth time step. The fluid pressure is released at the sink at right boundary $x=L$, represented as a zero Dirichlet boundary condition. The upper boundary is an impenetrable bone wall, given as a zero Neumann boundary condition. The bottom boundary, i.e. the BM boundary, is a mixture of Dirichlet and

Neumann boundary condition. Coefficient $\eta(x, u^{n-1}, u^{n-2})$ incorporates BM stiffness and BM's temporal state, and is updated at each time step by the results of previous two time steps. The detailed derivation of the cochlear model will be given in Chapter 4.1.

The numerical solution of the aforementioned boundary value problem can be computed by using collocation method. Let $\mathcal{L}$ denote the differential operator for the interior of the domain (i.e. the Laplacian operator ∇^2), and let $\mathcal{B}$ denote the differential operator for the boundary of the domain. The set of partial differential equation can be simplified as

$$\begin{aligned} \mathcal{L}u^n &= 0, \quad \text{in } \Omega \\ \mathcal{B}u^n &= g, \quad \text{in } \partial\Omega \end{aligned}$$

where $g(0, z) = f^n$, $g(L, z) = 0$ for $0 \leq z \leq H$, and $g(x, 0) = g(x, H) = 0$ for $0 \leq x \leq L$.

First, the solution $u^n(x, z)$ is approximated by a linear combination of basis functions $\{\phi_j(x, z)\}$, namely

$$u^n(x, z) = \sum_{j=1}^{M} c_j \phi_j(x, z).$$

By selecting certain mutually exclusive collocation points $\{x_i, z_i\}_{i=1}^{N_i}$ in Ω, and $\{x_i, z_i\}_{i=N_i+1}^{N}$ on $\partial\Omega$, the values of the basis function coefficients c_j can be derived by enforcing

$$\sum_{j=1}^{M} c_j \mathcal{L}\phi_j(x_i, z_i) = 0, \quad \text{for } i = 1, \cdots, N_i, \tag{3.1}$$

and

$$\sum_{j=1}^{M} c_j \mathcal{B}\phi_j(x_i, z_i) = g(x_i, z_i), \quad \text{for } i = N_i + 1, \cdots, N. \tag{3.2}$$

Equation (3.1) and (3.2) can be written in the matrix format as

$$\begin{bmatrix} A \\ B \end{bmatrix} C = \begin{bmatrix} 0 \\ G \end{bmatrix},$$

where

$$A = \begin{bmatrix} \mathcal{L}\phi_1(x_1, z_1) & \mathcal{L}\phi_2(x_1, z_1) & \cdots & \mathcal{L}\phi_M(x_1, z_1) \\ \mathcal{L}\phi_1(x_2, z_2) & \mathcal{L}\phi_2(x_2, z_2) & \cdots & \mathcal{L}\phi_M(x_2, z_2) \\ \vdots & \vdots & \ddots & \vdots \\ \mathcal{L}\phi_1(x_{N_i}, z_{N_i}) & \mathcal{L}\phi_2(x_{N_i}, z_{N_i}) & \cdots & \mathcal{L}\phi_M(x_{N_i}, z_{N_i}) \end{bmatrix},$$

$$B = \begin{bmatrix} \mathcal{B}\phi_1(x_{N_i+1}, z_{N_i+1}) & \mathcal{B}\phi_2(x_{N_i+1}, z_{N_i+1}) & \cdots & \mathcal{B}\phi_M(x_{N_i+1}, z_{N_i+1}) \\ \mathcal{B}\phi_1(x_{N_i+2}, z_{N_i+2}) & \mathcal{B}\phi_2(x_{N_i+2}, z_{N_i+2}) & \cdots & \mathcal{B}\phi_M(x_{N_i+2}, z_{N_i+2}) \\ \vdots & \vdots & \ddots & \vdots \\ \mathcal{B}\phi_1(x_N, z_N) & \mathcal{B}\phi_2(x_N, z_N) & \cdots & \mathcal{B}\phi_M(x_N, z_N) \end{bmatrix},$$

$$C = [c_1, c_2, \cdots, c_J]^\top,$$

and

$$G = [g(x_{N_i+1}, z_{N_i+1}), g(x_{N_i+2}, z_{N_i+2}), \cdots, g(x_N, z_N)]^\top.$$

The accuracy of the collocation method is dependent on the selection of basis functions and collocation points. The following sections present two types of basis functions: global radial basis functions and B-spline bases. Their properties and the corresponding collocation schemes are discussed.

3.2.1 Global Radial Basis Functions

A radial basis function (RBF) is a real-valued function whose value is dependent on the distance between the sampled position $\boldsymbol{x}$ to the center of the function $\boldsymbol{x}_c$[1]. That is

$$\phi_c(\boldsymbol{x}; \epsilon) = \phi(||\boldsymbol{x} - \boldsymbol{x}_c||_2; \epsilon) = \phi(r; \epsilon)$$

where r denotes the L_2 distance between $\boldsymbol{x}$ and $\boldsymbol{x}_c$. ϵ is the shape parameter to control how localized the basis function is; usually speaking, the smaller $|\epsilon|$, the flatter (less localized) the basis function. A global RBF is an RBF with global support, which would result in a non-sparse system matrix in a collocation scheme. In return, using global basis functions allows us to have arbitrary distribution of basis function and collocation points. The collocation method using global RBF are also called meshfree methods because the absence of a discretization mesh during computation. The meshfree methods are generally advantageous in solving problems defined on an irregularly shaped domain because efforts to create and maintain a proper discretization

[1] In this thesis, the center of a basis function refer to the point about which the value of the function is symmetrical.

mesh is removed.

The partial derivatives of RBFs with respect to dimension x_i are given as follows. For any sufficiently differentiable RBFs, the chain rule yields

$$\frac{\partial \phi}{\partial x_i} = \frac{\mathrm{d}\phi}{\mathrm{d}r}\frac{\partial r}{\partial x_i}$$

and

$$\frac{\partial^2 \phi}{\partial x_i^2} = \frac{\mathrm{d}\phi}{\mathrm{d}r}\frac{\partial^2}{\partial x_i^2} + \frac{\mathrm{d}^2\phi}{\mathrm{d}r^2}(\frac{\partial r}{\partial x_i})^2$$

where

$$\frac{\partial r}{\partial x_i} = \frac{x_i}{r}$$

and

$$\frac{\partial^2 r}{\partial x_i^2} = \frac{1 - [\frac{\partial r}{\partial x_i}]^2}{r}.$$

In this thesis, the collocation scheme for global RBF is very straight-forward: the centers of the function basis coincide with the collocation points. For a specific class of global RBFs, the accuracy of collocation scheme can be controlled by three factors: the distribution of function basis, the distribution of collocation points, and the shape parameter ϵ. Generally speaking, high accuracy of approximation is usually obtained when the domain is densely "covered" with function basis and collocation points, and when less localized (small ϵ) function bases are used. However, the large number of function bases and collocation points drastically increases the computational cost of the system matrix. Worse still, small point distance with flat (non-localized) function bases result in a system matrix with large condition number, rendering the solution unstable and sometimes unobtainable. Finding the optimal collocation scheme for a function basis is currently an active research topic. More information can be found in [62].

In the following we introduce the multiquadric RBF and the Gaussian RBF.

Multiquadric RBF

The multiquadric RBF (MQRBF) was originally used as an interpolation method by Iowa State University Geodesist Roland Hardy in 1968. The work was published later on in 1971 [31]. In 1979, Richard Franke from the Naval Postgraduate School compared various methods to solve the scattered data interpolation problem [21]. He concluded that Hardy's MQ interpolation scheme was the best among all tested schemes. In 1990, the MQ method was modified by physicist Edward Kansa [35, 36]

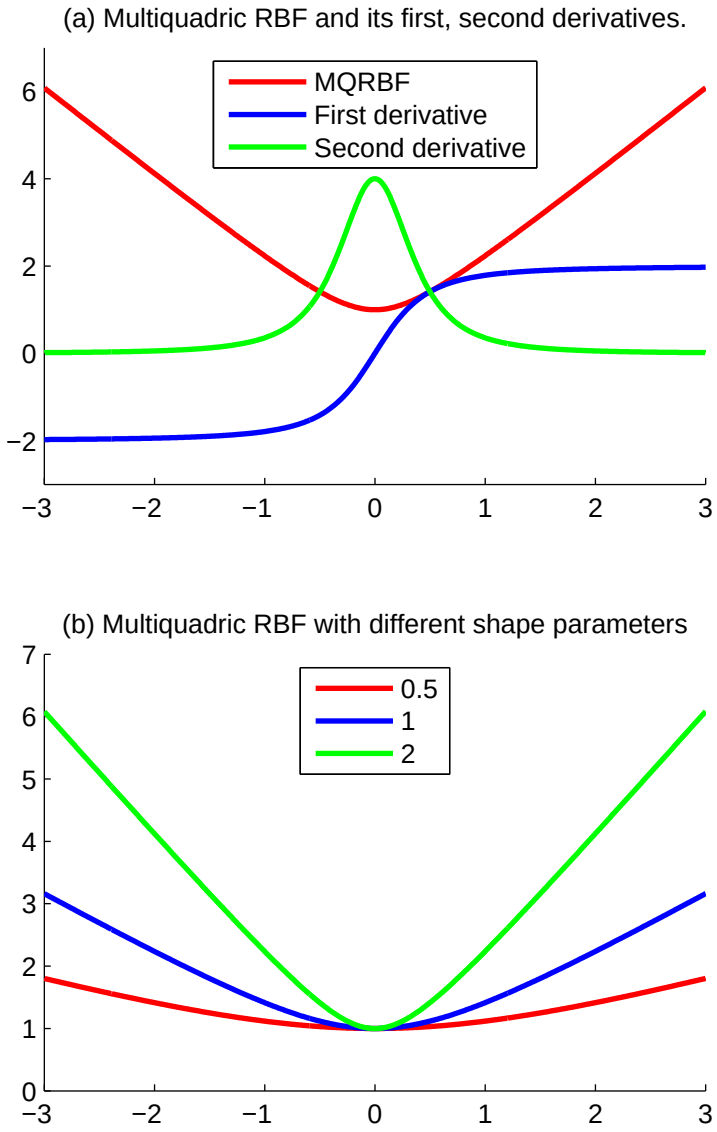

Figure 3.2: Shape of MQRBF.
Graph (a) plots the single variate MQRBF and its first, second order derivatives, with shape parameter $\epsilon = 2$. Graph (b) shows the effect of shape parameter. As we can see in the graph, the larger the shape parameter, the sharper (more localized) the basis function is.

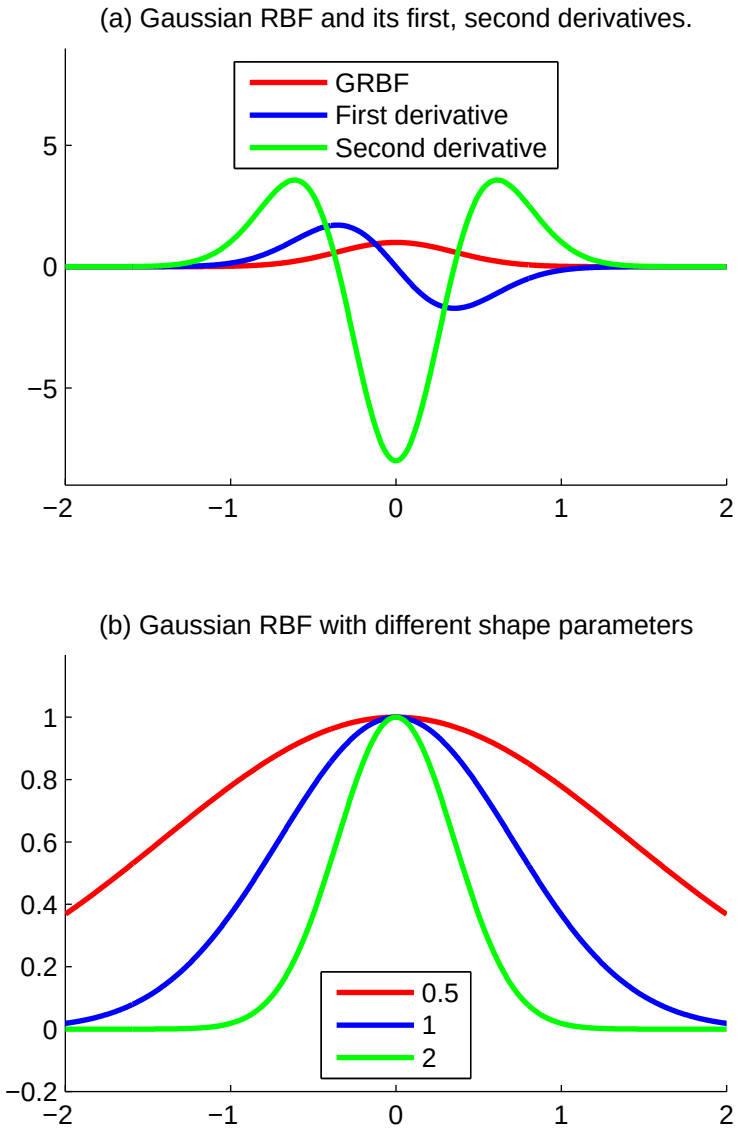

Figure 3.3: Shape of GRBF.
Graph (a) plots the single variate Gaussian RBF and its first, second order derivative, with shape parameter $\epsilon = 2$. Graph (b) shows the effect of shape parameter. As we can see in the graph, the larger the shape parameter, the sharper (more localized) the basis function is.

to solve differential equations, after which the popularity of the method grow rapidly.

The MQRBF $\phi_{\mathrm{MQ}}(r, \epsilon)$ is defined as

$$\phi_{\mathrm{MQ}}(r; \epsilon) = \sqrt{1 + \epsilon^2 r^2}$$

Figure 3.2 illustrates the properties of the MQRBF. As we can see in Figure 3.2 (a), the further away the sampling point is from the function center, the greater value the function obtains. That means the configuration of the system matrix is sensitive to the collocation points at the boundary of the domain.

Gaussian RBF

The Gaussian RBF (GRBF) is named after the German mathematician Carl Friedrich Gauss. It is defined as

$$\phi_{\mathrm{G}}(r; \epsilon) = e^{-(\epsilon r)^2}$$

where e is the base of the natural logarithm Introduced by L. Euler.

Figure 3.3 illustrates the properties of the GRBF. Similar to MQRBF, the function value is more localized with a greater shape parameter ϵ. But unlike MQRBF, the value of GRBF decreases quickly as the sampling point moves away from the function center. Therefore, the GRBF is more sensitive to local structure of collocation points instead of the boundary of the domain.

3.2.2 B-Spline Bases

In contrast to the aforementioned global basis functions, locally supported spline basis functions are used also used in the solution schemes. The following introduces the formulation of the quadratic and cubic spline defined in [6]. Their corresponding collocation schemes are also given.

Let $\pi_{n-1} = \pi^1_{n-1}$ denote the space of all polynomials in one variable of order n, or degree at most $n-1$, and let $a = t_0 < \cdots < t_{m+1} = b$. The space

$$\mathcal{S}_{\boldsymbol{t},n} = \{f \in C^{n-2}[a, b] : f|_{[t_i, t_{i+1}]} \in \pi_{n-1}, i = 0, \cdots, m, \}$$

is called the spline space of order n and with knot sequence $\boldsymbol{t} = \{t_i\}, i = 1, \cdots, m$.

Definition 1. *Divided differences. Let*

$$\boldsymbol{t} : \cdots \leq t_0 \leq t_1 \leq t_2 \leq \cdots$$

be a nondecreasing sequence of real numbers. Then the divided difference (dd) of a (sufficiently smooth) function $f(t)$ is defined as follows: the zeroth dd of $f(t)$ at $t = t_k$ is

$$[t_k]f := f(t_k);$$

the first dd of $f(t)$ at $\{t_k \le t_{k+1}\}$ is

$$[t_k, t_{k+1}] := \begin{cases} f'(t_k), & \text{if } t_k = t_{k+1}, \\ \frac{f(t_{k+1})-f(t_k)}{t_{k+1}-t_k}, & \text{if } t_k \neq t_{k+1}; \end{cases}$$

and, for any $m > 0$, the mth dd of $f(t)$ at $\{t_k \le \cdots \le t_{k+m}\}$ is

$$[t_k, \cdots, t_{k+m}]f := \begin{cases} \frac{f^{(m)}(t_k)}{m!}, & \text{if } t_k = \cdots = t_{k+m} \\ \frac{[t_{k+1},\cdots,t_{k+m}]f-[t_k,\cdots,t_{k+m-1}]f}{t_{k+m}-t_k}, & \text{if } t_k \neq t_{k+m}. \end{cases}$$

The normalized B-spline basis which spans spline space $\mathcal{S}_{\boldsymbol{t},n}$ is defined as

$$N_{\boldsymbol{t},n,i}(x) = (t_{i+n} - t_i)[t_i, \cdots, t_{i+n}]_t (t - x)_+^{n-1}$$

where the divided difference is taken at the variable t, and

$$(t - x)_+^{n-1} = \max((t - x)^{n-1}, 0)$$

is a truncated power function.

The explicit formulation for each polynomial piece of the B-spline $N_{\boldsymbol{t},n,i}(x)$ can be deduced by the following algorithm given in [6].

Let

$$\phi_k^n(x) = \binom{n}{r} x^k (1 - x)^{n-k}$$

and

$$\phi_{j,k}^n(x) = \phi_k^n\Big(\frac{x - t_j}{t_{j+1} - t_j}\Big)$$

We will denote the restriction of $N_{\boldsymbol{t},n,i}$ to $[t_j, t_{j+1}]$ by

$$P_{i,j}^n(x) = \sum_{k=0}^{n-1} a_k^{n-1}(i, j)\phi_{j,k}^{n-1}(x).$$

The set of coefficients $\{a_k^{n-1}(i, j)\}$ will be called the Bernstein net of the B-spline $N_{\boldsymbol{t},n,i}$. We have the following result

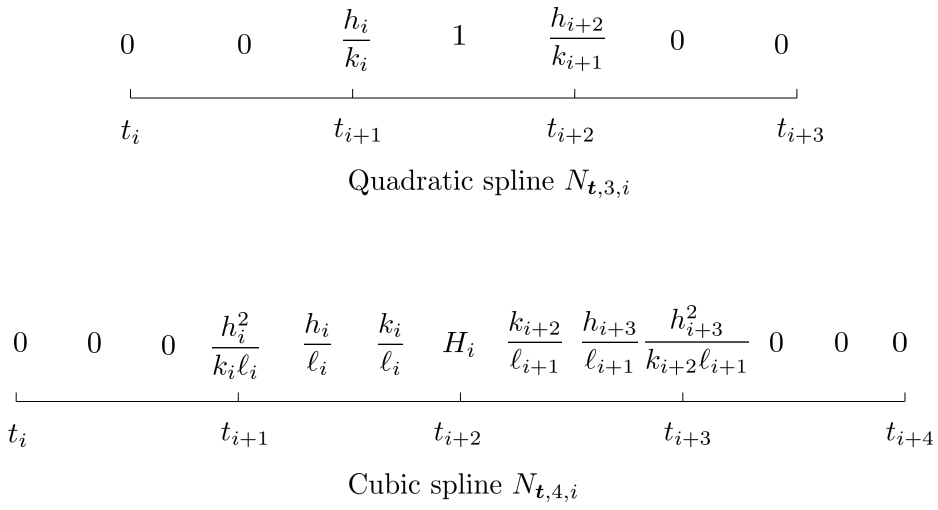

Figure 3.4: Bernstein net of the quadratic B-spline $N_{\boldsymbol{t},3,i}(x)$ and cubic B-spline $N_{\boldsymbol{t},4,i}(x)$.

Theorem 3.2.1. *Let* $a_k^{m-1}(i,i-1) = a_m^{m-1}(i,i+m) = 0$. *For each* $j = i, \cdots, i+m$ *and* $k = 0, \cdots, m-1$,

$$a_{k+1}^m(i,j) = a_k^m(i,j) + \frac{t_{i+j+1} - t_{i+j}}{t_{i+m} - t_i} a_k^{m-1}(i,j) - \frac{t_{i+j+1} - t_{i+j}}{t_{i+m+1} - t_{i+1}} a_k^{m-1}(i+1,j-1) \quad (3.3)$$

with initial condition $a_0^m(i,i) = 0$ *and* $a_0^m(i,j) = a_m^m(i,j-1), j = i+1, \cdots, i+m$.

In the special case of uniform mesh, say $t_k = k$, the formula 3.3 for computing the B-spline $N_n(x)$ is particularly simple, since by setting $i = 0$, it becomes:

$$a_{k+1}^m(0,j) = a_k^m(0,j) + \frac{1}{m}(a_k^{m-1}(0,j) - a_k^{m-1}(1,j-1))$$

with $a_0^m(0,0) = 0$, and $j, k = 0, \cdots, m-1$.

Hence, to compute $N_{m+1}(x)$ from $N_m(x)$, we first write down the Bernstein net for $\frac{1}{m}(N_m(x) - N_m(x-1))$, namely:

$$b_{jk}^{m-1} = \frac{1}{m}(a_k^{m-1}(0,j) - a_k^{m-1}(1,j-1)).$$

Then the Bernstein net $a_{jk}^m = a_k^m(0,j)$ of $N_{m+1}(x)$ can be obtained by the simple addition:

$$a_{j,k+1}^m = a_{jk}^m + b_{jk}^{m-1}, k = 0, \cdots, m-1,$$

with $a_{j0}^m = a_{j-1,m}^m$ and its initial condition $a_{00}^m = 0$, where the index $j, j = 0, \cdots, m-1$, indicates the $(j+1)$th polynomial pieces of $N_{m+1}(x)$. The computation of B-spline

on a nonuniform mesh is more complicated. By using Equation (3.3), we may find the Bernstein net of the quadratic and cubic splines as shown in Figure 3.4, where we have used the following notations.

$$\begin{cases} h_i = t_{i+1} - t_i \\ k_i = h_{i+1} + h_i = t_{i+2} - t_i \\ \ell_i = h_{i+2} + h_{i+1} + h_i = t_{i+3} - t_i \\ H_i = 1 - \frac{h_{i+2}^2}{k_{i+1}\ell_i} - \frac{h_{i+1}^2}{k_{i+1}\ell_{i+1}} \end{cases}$$

Figure 3.5 illustrates the shapes of quadratic and cubic B-splines basis derived by the aforementioned algorithm. Defined by equally spaced knots, quadratic B-spline spans three intervals, with the center located in the middle of the second interval; the cubic B-spline spans four intervals, with the center located on the knot between the second and the third interval. The quadratic spline is continuous up to first derivative; the cubic spline is continuous up to second derivative.

B-splines Collocation

In this part the collocation schemes for quadratic and cubic B-spline (QS and CS) are discussed. Define the domain of a univariate problem $[0, L]$, which is divided evenly into M segments with length h. Denote the endpoints of the segments as knot points $t_i, i = 0, \cdots, M$, it follows $t_i = i \times h$. The nth order spline space $\mathcal{S}_{\boldsymbol{t},n}$ on interval $[0, L]$ is spanned by a B-spline basis set $\mathcal{B}^n := \{B_j^n(x)\}_{j=-n+1}^{M-1}$. A function $f(x)$ defined on $[0, L]$ can be thus approximated as

$$f(x) \approx f_n(x) = \sum_{j=-n+1}^{M-1} c_j B_j^n(x) \tag{3.4}$$

We should note that a regular B-spline of n order spans n intervals. If only regular B-splines are used in approximation scheme defined in Equation (3.4), basis function $B_{-n+1}^n, \cdots, B_{-1}^n$ are defined partially outside the left boundary of domain $[0, L]$, and basis function $B_{M-n+1}^n, \cdots, B_{N-1}^n$ are defined partially outside the right boundary of domain $[0, L]$. Such bases are unsuitable for collocation methods. Because collocation points can only locate inside the problem domain (both interior and on boundaries), information about the external parts of the basis functions is unobtainable by collocation, which in turn render the system matrix less accurate or even singular. [5] shows collocation schemes using only regular B-splines. The proper rate of convergence cannot be retained unless perturbations are introduced to the system matrix.

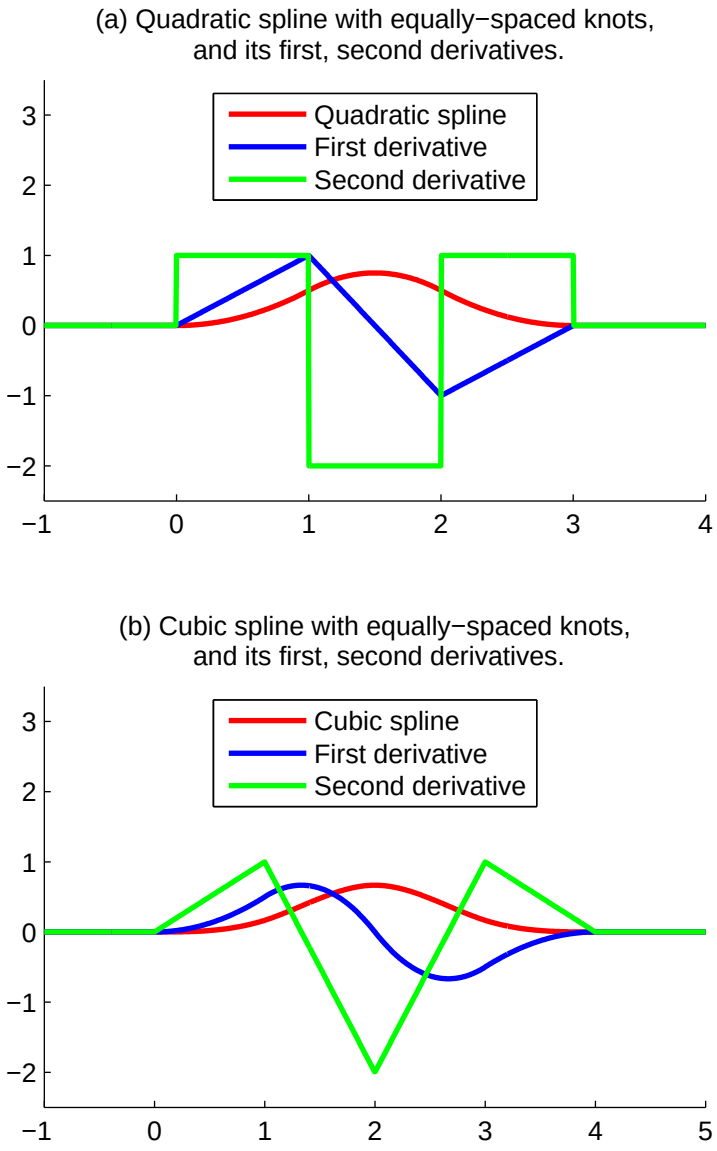

Figure 3.5: B-splines and their first, second derivatives

In this thesis, the B-spline basis functions are corrected as they are close to the boundary of the problem. The modified B-splines are defined only inside the problem domain, yet still serve as the bases for the corresponding spline space. The correction can be demonstrated with Figure 3.4. Take the cubic B-spline for example; if interval $[t_i, t_{i+4}]$ resides inside the problem domain, the corresponding B-spline is uncorrected; if a part of the interval $[t_i, t_{i+4}]$ is outside of the problem domain, the nodes that are outside of the domain are assigned to be the same as the boundary node, which updates the Bernstein net and consequently defines the corrected B-spline.

Figure 3.6 shows the corrected Bernstein net of quadratic and cubic B-spline defined to the left boundary of the domain $[0, L]$. The explicit formula of the corresponding left-boundary B-splines are defined as follows.

$$
\begin{aligned}
B^4_{-3}(x) &= \frac{(h-x)^3}{h^3}, \quad 0 \le x < h; \\
B^4_{-2}(x) &= \begin{cases} \frac{x(12h^2-18hx+7x^2)}{4h^3}, & 0 \le x < h, \\ \frac{(2h-x)^3}{4h^3}, & h \le x < 2h; \end{cases} \\
B^4_{-1}(x) &= \begin{cases} \frac{(18h-11x)x^2}{12h^3}, & 0 \le x < h, \\ -\frac{3}{2} + \frac{9x}{2h} - \frac{3x^2}{h^2} + \frac{7x^3}{12h^3}, & h \le x < 2h, \\ \frac{(3h-x)^3}{6h^3}, & 2h \le x < 3h; \end{cases} \\
B^4_{0}(x) &= \begin{cases} \frac{x^3}{6h^3}, & 0 \le x < h, \\ \frac{2}{3} - \frac{2x}{h} + \frac{2x^2}{h^2} - \frac{x^3}{2h^3}, & h \le x < 2h, \\ -\frac{22}{3} + \frac{10x}{h} - \frac{4x^2}{h^2} + \frac{x^3}{2h^3}, & 2h \le x < 3h \\ \frac{(4h-x)^3}{6h^3}, & 3h \le x < 4h; \end{cases} \\
B^3_{-2}(x) &= \frac{(1-x)^2}{h^2}, \quad 0 \le x < h, \\
B^3_{-1}(x) &= \begin{cases} \frac{(4-3x)x}{2h^2}, & 0 \le x < h, \\ \frac{(2-x)^2}{2h^2}, & h \le x < 2h, \end{cases} \\
B^3_{0} &= \begin{cases} \frac{x^2}{2h^2}, & 0 \le x < h, \\ -\frac{3}{2} + \frac{3x}{h} - \frac{x^2}{h^2}, & h \le x < 2h, \\ \frac{(3-x)^2}{2h^2}, & 2h \le x < 3h. \end{cases}
\end{aligned}
$$

The collocation set $\mathcal{S}_{\text{QS}}$ for quadratic B-spline is defined as the union of two

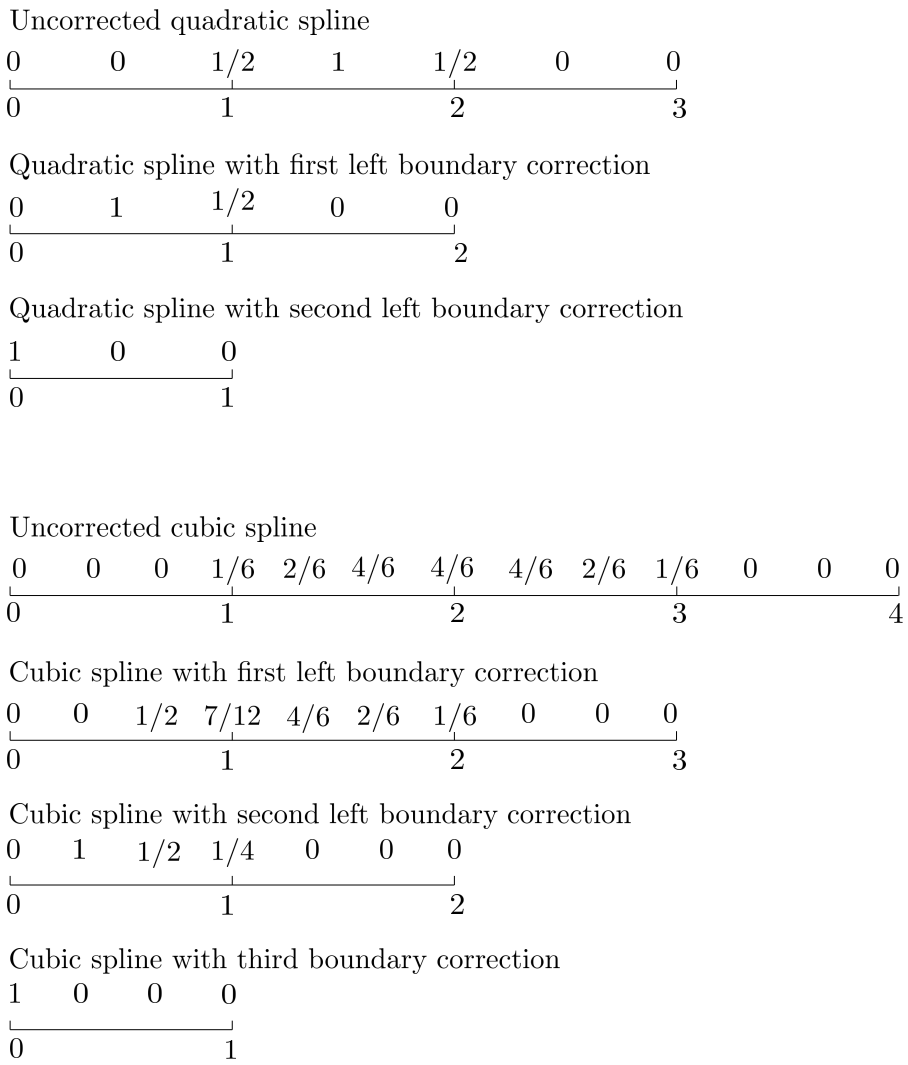

Figure 3.6: Bernstein net of the quadratic and cubic B-splines with boundary corrections. The splines are defined on an integer interval at the left boundary of the domain $[0, L]$. The Bernstein net of the right boundary is horizontal reflection of that on the left boundary.

boundary points and the mid-point of the intervals $[t_k, t_k + 1]$. That is

$$\mathcal{S}_{\text{QS}} := \{x_i\}_{i=1}^{M+2}, \quad \text{where } x_1 = 0, \quad x_{M+2} = L,$$
$$x_i = i \times h - \frac{3h}{2}, \quad i = 2, \cdots, M+1.$$

The collocation set $\mathcal{S}_{\text{CS}}$ for cubic B-spline is defined as the union of all the knot points of the domain and the mid-points of two boundary interval $[0, h]$ and $[L-h, L]$. That is

$$\mathcal{S}_{\text{CS}} := \{x_i\}_{i=1}^{M+3}, \quad \text{where } x_1 = 0, \quad x_2 = \frac{h}{2}, \quad x_{M+1} = L - \frac{h}{2}, \quad x_{M+2} = L,$$
$$x_i = (i-2) \times h, \quad i = 3, \cdots, M+1$$

Extending univariate B-spline collocation scheme to multivariate rectangular domain is straightforward. Take two dimensional domain $(x, y) \in \mathbb{R}^2$ for example. Denote $B_i^n(x)$ the basis function for dimension x with index set $\mathcal{I}$, and denote the corresponding collocation points x_p with index set $\mathcal{P}$. Denote $B_j^n(y)$ the basis function for dimension y with index set $\mathcal{J}$, and denote the corresponding collocation points y_q with index set $\mathcal{Q}$. The two dimensional basis function is given by the tensor product

$$\phi_{i,j}(x, y) = B_i^n(x) B_j^n(y), \quad i \in \mathcal{I} \text{ and } j \in \mathcal{J},$$

and the corresponding collocation points are given as

$$(x_p, y_q), \quad p \in \mathcal{P} \text{ and } q \in \mathcal{Q}.$$

Figure 3.7 and 3.8 illustrate the boundary splines and the corresponding two dimensional collocation schemes for quadratic and cubic splines.

B-spline basis functions are local basis functions. Compared to using global basis functions, collocation scheme with local basis functions results in a sparse system matrix, which is generally advantageous in data storage and computational time. However, the use of B-spline basis functions requires a more rigid collocation scheme; solutions are only obtainable with regular distribution of function centers and collocation points.

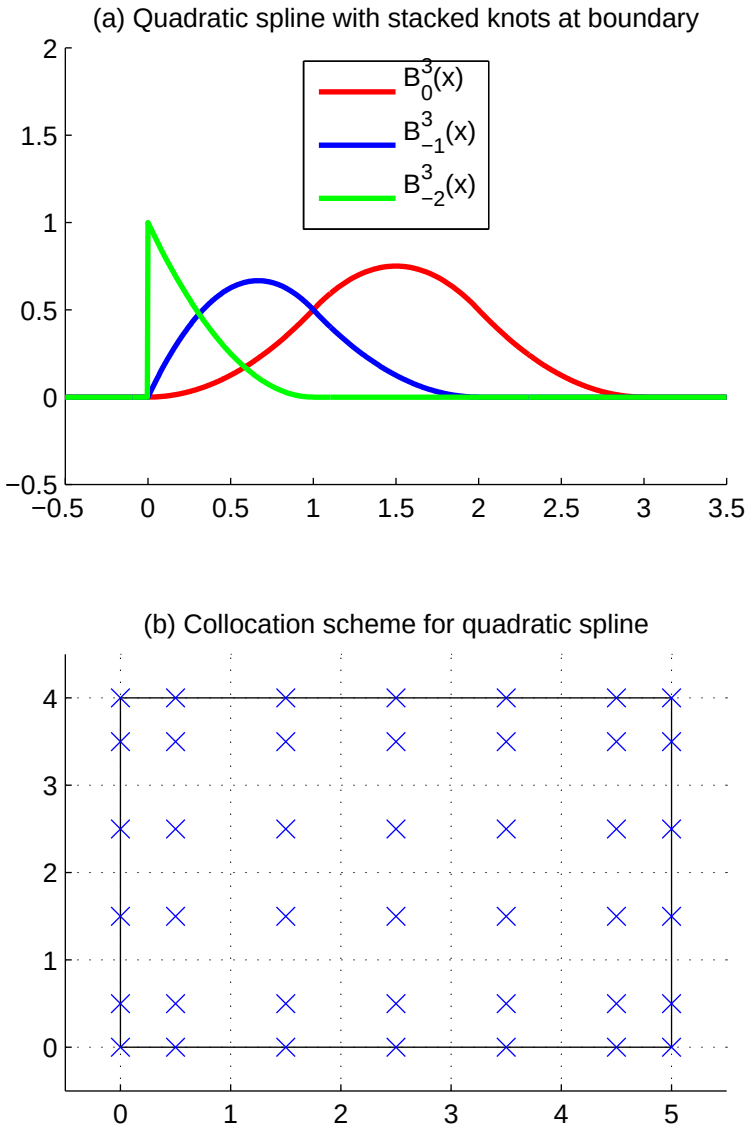

Figure 3.7: Boundary quadratic B-spline and the 2D collocation scheme.
(a) Boundary quadratic B-splines. The boundary splines on the right boundary is the horizontal reflection of the case in the left. (b) Two dimensional collocation scheme for domain $[0, 5] \times [0, 4]$, where collocation points are marked as "$\times$".

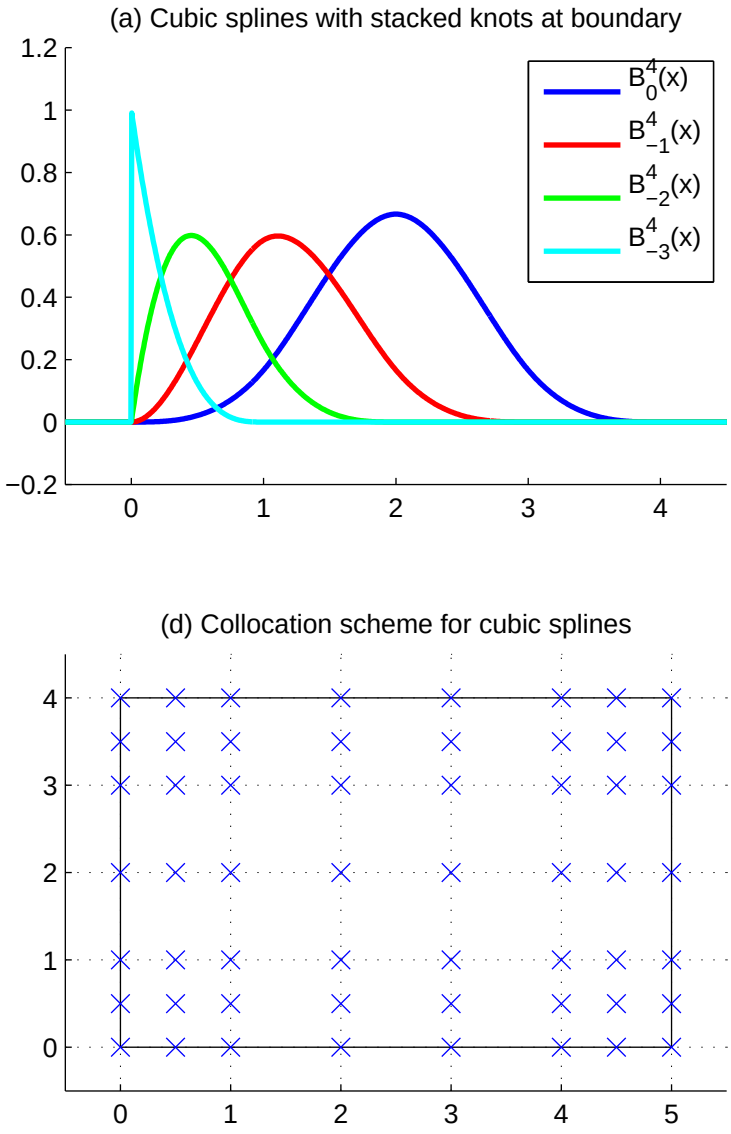

Figure 3.8: Boundary cubic B-spline and the 2D collocation scheme.
(a) Boundary cubic B-splines. The boundary splines on the right boundary is the horizontal reflection of the case in the left. (b) Two dimensional collocation scheme for domain $[0, 5] \times [0, 4]$, where collocation points are marked as "$\times$".

3.3 Multistep Method

Physical and engineering problems can often be modeled into so-called initial-value problems (IVPs) [3], that is, the solution to which is required to satisfy a given initial condition. One very typical category of the problem is the time domain simulation of physical phenomenon: estimating the temporal states of a systems given the the initial state of the system, the duration of time, and a set of differential equations to govern the evolution of the state of the system.

The following defines a prototype of a univariate initial-value problem: find the value of time-domain function $y(t)$ given

$$y'(t) = f(t, y), \quad a \leq t \leq b, \quad y(a) = \alpha.$$

The solution to an initial-value problem can be approximated by the solution of the weaker form of the problem on a discretized domain. To numerically solve a time domain problem $y(t)$ on $[a, b]$, one can discretized the time variable t into a series of successive time steps $t_0, t_1, \cdots, t_N$, where $t_0 = a$ and $t_N = b$. We know $y(t_0) = y(a) = \alpha$; function values at $t_1, t_2, \cdots, t_N$ can be computed by function values at previous time-steps and the evaluation of $f(t, y)$. For the sake of simplicity, the methods discussed in this dissertation use constant step size. That is, $t_n = t_0 + n \times h$, with constant step size h.

Popular methods for solving IVPs can be categorized into one-step methods and multi-step methods. One-step methods approximate the function value at t_{n+1} using information from only one of the previous time step t_i. To ensure the accuracy of numerical approximation, one-step methods, such as the popular "Runge-Kutta" methods, often evaluates $f(t, y)$ multiple times in the subinterval between t_n and t_{n+1}. These function evaluation could be costly. And because the information is obtained within the subinterval between t_n and t_{n+1}, it is not retained for direct use for the future approximations. To efficiently reuse previous computed results as a means to improve approximation accuracy, we can use function values $y(t)$ and $f(t, y)$ at multiple previous time steps t_i, t_{i-1} to compute the function values at the current time t_{n+1}. Such approximation methods are called multi-step methods.

The following equation defines the linear m-step method:

$$y_{n+1} = \sum_{j=0}^{m-1} a_j y_{n-1} + h \sum_{j=-1}^{m-1} b_j f(t_{n-j}, y_{n-j}) \tag{3.5}$$

for all integers n satisfying $0 \leq nh \leq b - a$. When $b_{-1} = 0$ the method is called explicit, or open, since Equation (3.5) gives y_{n+1} explicitly in terms of previously determined values. When $b_{-1} \neq 0$ the method is called implicit, or closed, since y_{n+1} occurs on both sides of the equation.

The following introduce the m-step backward difference formula methods, **BDFm** [54]. These methods can be derived by interpolating the function $y(t)$ at $t_{n+1}, t_n, \cdots, t_{n+1-m}$ with an m-degree polynomial $p_m(t)$, then replacing the derivative y' with $p'_m(t)$ for discretization.

For $m = 1$, since

$$p_1(t) = y(t_{n+1}) + (t - t_{n+1}) + (t - t_{n+1})\frac{y(t_{n+1} - y(t_n))}{h},$$

discretization gives

$$\frac{y_{n+1} - y_n}{h} = f(t_{n+1}, y_{n+1}).$$

The **BDF1** formula is therefore

$$y_{n+1} = y_n + hf(t_{n+1}, y_{n+1})$$

which is also called the Backward Euler Method.

For $m = 2$,

$$p_2(t) = y(t_{n+1}) + (t - t_{n+1})[\frac{y_{n+1} - y_n}{h} + (t - t_n)\frac{y_{n+1} - 2y_n + y_{n-1}}{2h^2}],$$

$$p'_2(t_{n+1}) = \frac{3yy_{n+1} - 4y_n + y_{n-1}}{2h}.$$

Through discretization we obtain the **BDF2** formula

$$y_{n+1} = \frac{4}{3}y_n - \frac{1}{3}y_{n-1} + \frac{2h}{3}f(t_{n+1}, y_{n+1})$$

One can refer to [3] for a more comprehensive IVP solution methods, their convergence condition, and example of applications.

Handling IVP with Higher Degree Derivatives

For initial-value problem specified with derivatives of degree greater than one, additional variables representing lower degree derivatives can be added to form multiple lines of linear equations. For example, to use **BDF2** to numerically approximate the

following problem

$$y''(t) = f(t, y), \quad a \leq t \leq b, \quad y(a) = \alpha,$$

one can define variable $v(t) = y'(t)$, and thus $v'(t) = y''(t)$. The following set of equations can be derived

$$\begin{aligned} y_{n+1} &= \frac{4}{3}y_n - \frac{1}{3}y_{n-1} + \frac{2h}{3}v_{n+1}, \\ v_{n+1} &= \frac{4}{3}v_n - \frac{1}{3}v_{n-1} + \frac{2h}{3}f(t, y_{n+1}). \end{aligned}$$

The aforementioned technique is applied in solving the temporal-spatial cochlear model because the state of the basilar membrane is defined with a second order time differential equation.

Chapter 4

Cochlear Models and Simulations

4.1 Mathematical Models

4.1.1 Passive Model

The cochlea is filled with water-like incompressible Stokes fluids. If we assume that the Reissner's membrane deforms passively with fluid movements, as it is commonly handled in cochlear models, the cochlea can be viewed as two fluid chamber divided by the BM in the middle. The movements of BM is subjected to the pressure difference between the two fluid chambers. In this thesis, the cochlea is modeled in two dimensions. To further simplify the model, we model only the upper cochlea chamber as an rectangle $\Omega \cup \partial\Omega = [0, L] \times [0, H]$, with the BM at $z = 0$ (Figure 4.1). The lower cochlear chamber is removed because it is symmetric to the upper chamber with respect to the BM, and thus its pressure is complementary to that of the upper chamber. Such simplification is also used in [43, 49].

Sound pressure is applied at the stapes, represented as the left boundary $x = 0$ of the domain. The change of pressure induces fluid motions to propagate along the the upper chamber (SV), reaching a small hole (helicotrema) at the other end of the domain $x = L$. In an actual cochlea, fluid motions continue to travel into the "lower" chamber (ST), causing a pressure difference against the fluids in SV. In our simplified model, the pressure difference is modeled as simply the pressure in the upper chamber. Let p represents the fluid pressure in our simplified model, and p_{SV}, p_{ST} represents the fluid pressure in SV and ST in an actual cochlea, it follows

$$p = p_{\mathrm{SV}} - p_{\mathrm{ST}} \tag{4.1}$$

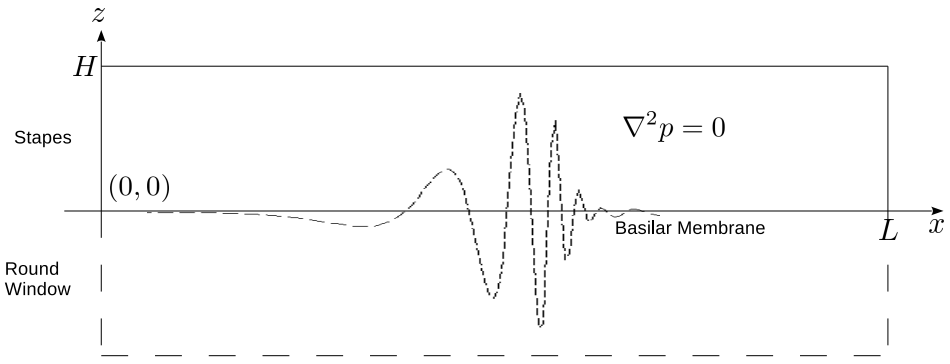

Figure 4.1: Diagram of the two-dimensional cochlear model and magnified BM vibration

Figure 4.1 shows the the diagram of our two-dimension cochlear model with BM movements. Note that the BM movements are amplified several orders of magnitude for ease of viewing. In an actual cochlea, the BM movement is on the order of nanometers (nm) [52, 56, 26], while our domain size is on the order of centimeters (cm). Because of this huge difference in length scales, the BM displacements is in effect negligible in fluid simulations. Thus we model the cochlear chamber with a fixed domain boundary $\partial\Omega$.

From the incompressibility of the cochlear fluid, the pressure p satisfies

$$\nabla^2 p(x, z, t) = \frac{\partial^2 p}{\partial x^2} + \frac{\partial^2 p}{\partial z^2} = 0, \quad (x, z) \in [0, L] \times [0, H], \tag{4.2}$$

where ∇^2 is the Laplacian operator.

The upper boundary at $z = H$ represents the bony wall of cochlear chamber, rigid and impenetrable to cochlear fluids. It follows

$$\frac{\partial p}{\partial z}(x, H, t) = 0, \quad 0 \le x \le L \tag{4.3}$$

The right boundary at $x = L$ represents the helicotrema, which equalizes the fluid pressure between SV and ST. Therefore the fluid pressure satisfies a zero Dirichlet boundary condition:

$$p(L, z, t) = 0, \quad 0 \le z \le H. \tag{4.4}$$

Some other cochlear models instead use a zero Neumann boundary condition at $x = L$. It is shown in [49, 75] that the alternative configuration has minimal effect on the interior BM response. However, using Neumann boundary condition might offer some insights into the dispersive nature of BM dynamics.

The left boundary at $x = 0$ represents the footplate of the stapes, which applies

sound pressure to cochlear fluids:

$$\frac{\partial p}{\partial x}(0, z, t) = 2\rho T_m p_e(t), \quad 0 \le z \le H, \tag{4.5}$$

where ρ is the density of fluid, T_m is the middle ear filtering operator, and $p_e(t)$ is the input sound pressure at the eardrum. The middle ear filtering is frequency dependent. If the input is defined as an multi-tone signal $p_e = 2\sum_{j=1}^{J_m} A_j \cos(\omega_j t)$, we have

$$T_m p_e(t) = 2\sum_{j=1}^{J_m} a_m(\omega_j) A_j \cos(\omega_j t), \tag{4.6}$$

where $a_m(\cdot)$ is the following.

$$a_m(\omega) = 30(1/30 + 0.0605\omega^2((1 - \omega^2\omega_m^{-2})^2 + (2\phi_m\omega/\omega_m)^2)^{-0.5}). \tag{4.7}$$

Here, ω_m is the middle ear characteristic frequency 4 kHz. $\phi_m = 0.7$ represents the middle ear damping ratio. Equation (4.7) is obtained by fitting experimental data in [29].

Let the BM displacement along the z direction be represented by $u(x, t)$, with the first and second order derivatives denoted by $u_t(x, t)$ and $u_{tt}(x, t)$, respectively. Then the bottom boundary (BM) condition at $z = 0$ is given by

$$\frac{\partial p}{\partial z}(x, 0, t) = 2\rho u_{tt}(x, t), \quad 0 \le x \le L. \tag{4.8}$$

The BM is modeled as a spring-mass system subjected to the external force p. Following the classical spring-mass mechanics, we obtain

$$p(x, 0, t) = m u_{tt}(x, t) + r u_t(x, t) + s(x)u(x, t), \quad 0 \le x \le L, \tag{4.9}$$

where m represents the mass density, r represents the damping term, and $s(x)$ represents the varying stiffness of the BM along its length. $s(x)$ is defined as

$$s(x) = 4\pi^2 m(0.456 \exp(4.83(1 - x/L)) - 0.45)^2. \tag{4.10}$$

The formula is based on data in [28, 44]; see also [16, 76].

The model presented above is a complete initial boundary value problem, with initial value given by $u(x, 0)$ and $u_t(x, 0)$, the initial displacement and velocity of BM segments. Pressure $p(x, z, t)$ can be uniquely determined by the spatial conditions

once the $u(x,t)$ and $u_t(x,t)$ is resolved.

The cochlear mode listed above does not incorporate the effect of the cochlear amplifier. As demonstrated in past cochlear researches, the passive cochlear model could not achieve characteristics such as the high frequency selectivity the actual cochlea possess. The OHC feed-forward model is introduced in addition to the passive model with the intension to bridge the gap between model performance and physiological data.

4.1.2 Feed-forward active model

A feed-forward (FF) OHC model is combined with the classical passive cochlea model to reproduce the high sensitivity and frequency selectivity of a normal ear. The model presented in this thesis appeared in [45]. Figure 4.2 shows a schematic drawing of the organ of Corti, view transversally and longitudinally. The OHCs are microstructures that live on the BM. Organized in rows, the OHCs responds to mechanical stimuli like piezo-electric actuators, pushing and pulling the BM. The force applied by the OHCs are assumed to be proportional to the force received by the BM. The total force applied on the BM is transmitted to the cilia of the OHCs, which in turn acts on the OHCs and back on the BM. We obtain the relation

$$F_{\text{cilia}}(x,t) = C_1(x,t)\frac{F_{\text{BM}}(x,t)}{2}, \tag{4.11}$$

where F_{cilia} is the force acting on the cilia, F_{BM} is the total force acting on the BM, and C_1 is a coefficient. F_{BM} is a compound of fluid force from both cochlear chambers F_f and OHCs feedback force F_{cell}

$$F_{\text{BM}}(x,t) = 2F_f(x,t) + F_{\text{cell}}(x,t). \tag{4.12}$$

As shown in the longitudinal view of Figure 4.2b, the array of OHCs leans towards the basal end of the cochlea. Thus the force acting on cilia at location x cause the OHCs to push (or pull) at a point $x + \Delta$ downstream on the BM:

$$F_{\text{cell}}(x+\Delta,t) = C_2(x,t)F_{\text{cilia}}(x,t), \tag{4.13}$$

where C_2 is a transfer function coefficient, and Δ is the OHCs tilt offset. Combining

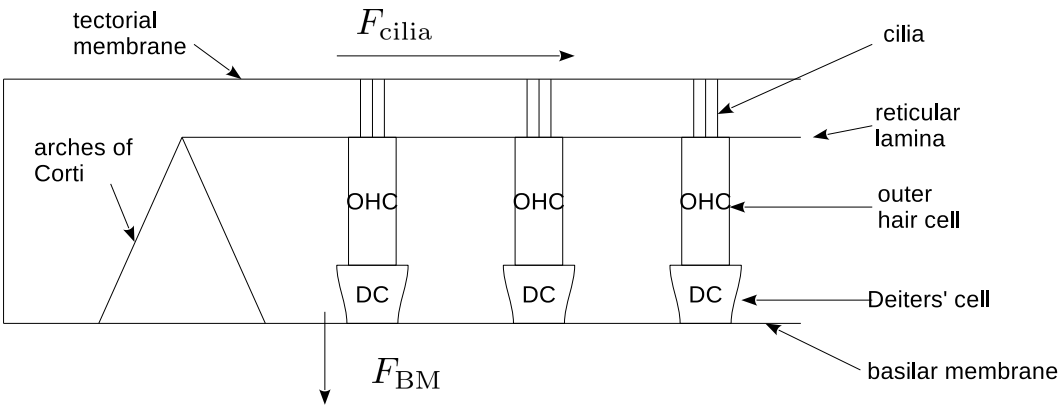

(a) Transverse view

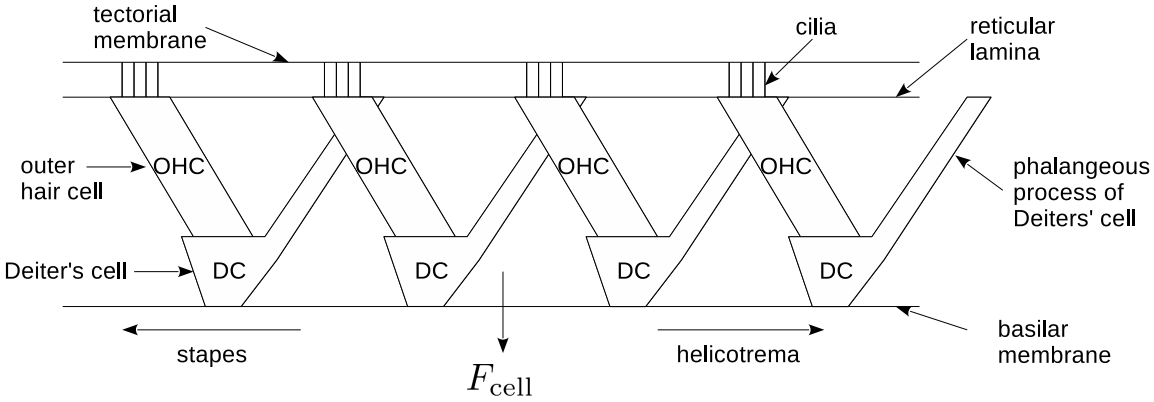

(b) Longitudinal view

Figure 4.2: Schematic drawing feed-forward OHC mechanism.
Both transversal and longitudinal view of the organ of Corti are shown. The force applied to BM causes a rotational movement around the pivot point of the arch of Corti, bringing a shear movement of the cilia against the tectorial membrane. Such shear movement results in the piezo-electric movement of the OHCs, consequently pushing or pulling the BM section downstream due to the longitudinal tilt of the OHCs. Image adapted with modification from [46].

Equation (4.11), (4.12) and (4.13), it follows

$$\begin{aligned} F_{\text{cell}}(x+\Delta,t) &= \frac{C_1(x,t)C_2(x,t)}{2}(2F_f(x,t)+F_{\text{cell}}(x,t)) \\ &= \alpha(x,t)(2F_f(x,t)+F_{\text{cell}}(x,t)), \end{aligned} \tag{4.14}$$

where $\alpha(x,t) = C_1C_2/2$ denotes the FF gain factor. It is known that the OHC force exhibits a compressive growth with respect to BM displacements u. More specifically, $alpha(x,t)$ remains fairly constant for small value u, and plummet to close to 0 as u increases.

4.1.3 Nonlinear nonlocal FF model

Kim and Xin's work in [39] discovered that the aforementioned FF model is problematic for its pointwise definition of BM feedback force. In temporal simulations, the evolving BM profile generates a sawtooth-shaped gain factor, which consequently renders the BM profile to be more irregular and unstable. Such a problem can be remedied by broadening the support of the BM gain factor, making the computation of α nonlocal:

$$\alpha(x,u,t) = \frac{\gamma}{\sqrt{\lambda\pi}}\int_0^L \exp(-(x-x')^2/\lambda)g(u(x',t))dx', \tag{4.15}$$

where γ and λ are constants. $g(\cdot)$ is defined as

$$g(x) = \frac{1}{2}(1+\tanh(6-\frac{|x|}{0.03})) \tag{4.16}$$

Figure 4.3 shows the shape of $g(\cdot)$.

According to Equation (4.1), we have $p(x,0,t) = 2F_f(x,t)$. Denote the OHC feedback force by $q(x,t) = F_{cell}(x,t)$. Then Equation (4.9) is modified as

$$q(x,t)+p(x,0,t) = mu_{tt}+ru_t+s(x)u, \quad 0 \le x \le L. \tag{4.17}$$

Equation (4.14) gives

$$q(x+\Delta,t) = \alpha(x,u,t)(p(x,0,t)+q(x,t)), \quad 0 \le x \le L-\Delta \tag{4.18}$$

At interval $x = [0,\Delta]$ we define $q(x,t) = 0$ because the lack of feedback force from the OHCs due to the longitudinal tilt.

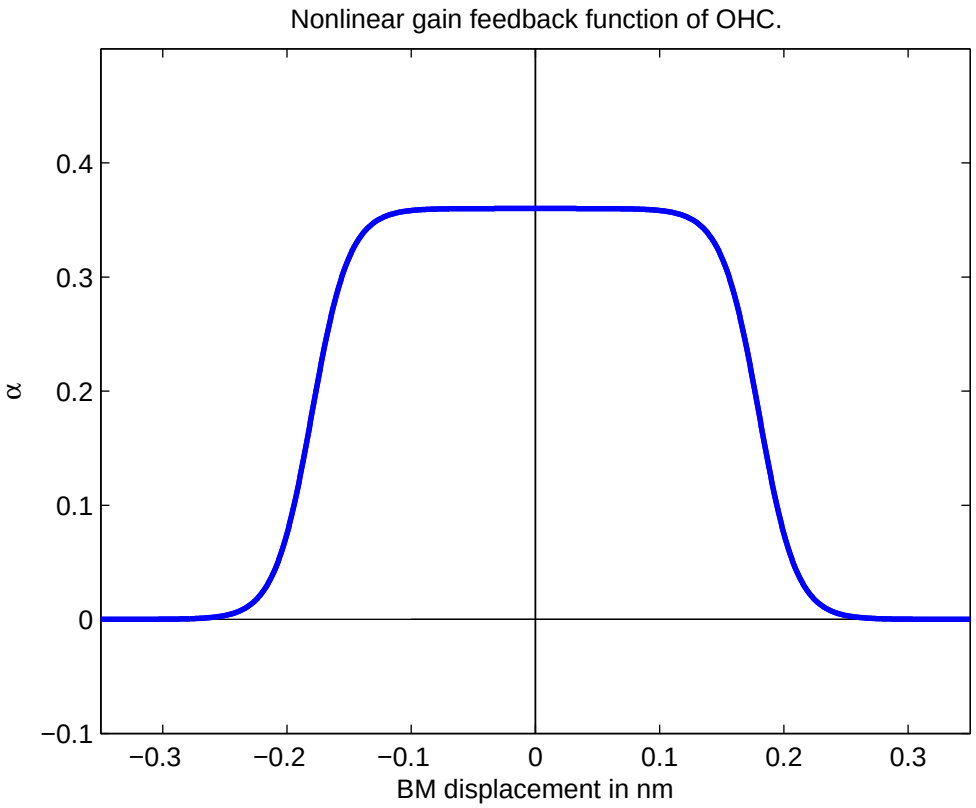

Figure 4.3: Nonlinear feedback gain on BM displacement values.

4.1.4 Overall Models

Summarizing the formulas in the mathematical modeling, the following two overall models can be derived.

Temporal-Spatial Model

The physical conditions listed above are gathered to form temporal-spatial partial differential equation system. To allow for more efficient numerical simulation, a change of variable is performed to homogenize the equations. Let $p' = p + 2\rho T_m p_e(t)(L - x)$. p' satisfies a Laplace equation with homogeneous boundary data except on $z = 0$. Replace p' by p as a notation, the temporal-spatial cochlear model is given by the

following set of differential equations:

$$\nabla^2 p(x,z,t) = 0, \quad (x,z) \in [0,L] \times [0,H], \tag{4.19}$$

$$p(L,z,t) = 0, \quad \frac{\partial p}{\partial x}(0,z,t) = 0, \quad \frac{\partial p}{\partial z}(x,H,t) = 0, \tag{4.20}$$

$$\frac{\partial p}{\partial z}(x,0,t) = 2\rho u_{tt}(x,t), \tag{4.21}$$

$$q(x,t) + p(x,0,t) = m u_{tt} + r u_t + s(x)u + 2\rho T_m p_e(t)(L-x), \tag{4.22}$$

$$q(x+\Delta,t) = \alpha(x,u,t)(p(x,0,t) + q(x,t) - 2\rho T_m p_e(t)(L-x)). \tag{4.23}$$

Spatial Model

Let us first assume that the sound input is a pure tone signal $p_e = Ae^{i\omega t}$, and impose the system response to take the form

$$u(x,t) = U(x)e^{i\omega t}, q(x,t) = Q(x)e^{i\omega t}, p(x,z,t) = P(x,z)e^{i\omega t}. \tag{4.24}$$

The aforementioned temporal-spatial model can be simplified into the following spatial model

$$\nabla^2 P(x,z) = 0, \quad (x,z) \in [0,L] \times [0,H], \tag{4.25}$$

$$P(L,z) = 0, \quad \frac{\partial P}{\partial x}(0,z) = 2\rho a_m(\omega)A, \quad \frac{\partial P}{\partial z}(x,H) = 0, \tag{4.26}$$

$$\frac{\partial P}{\partial z}(x,0) = -2\rho\omega^2 U(x), \tag{4.27}$$

$$Q(x) + P(x,0) = (-m\omega^2 + ir\omega + s(x))U(x), \tag{4.28}$$

$$Q(x+\Delta) = \alpha(P(x,0) + Q(x)). \tag{4.29}$$

Finding a numerical solution to the PDEs requires proper discretization of the solution domain. Because the spatial model is a simplified version of the temporal-spatial model, the spatial discretization techniques apply directly to the temporal-spatial model. In the following sections the solution to the spatial model is first presented. The effectiveness of various spatial discretization scheme are compared. Then the best scheme will be adapted in order to find the solution to the temporal-spatial model.

4.2 Spatial Model Solution

In this thesis, the basis function collocation methods are used to find the solution to the spatial cochlear model. Let the pressure value $P(x, z)$ function be a linear combination of basis functions

$$P(x, z) = \sum_{j=1}^{J} k_j \phi_j(x, z). \tag{4.30}$$

If global radial basis functions are used, we have

$$\phi_j(x, z) = \phi(x - x_j, z - z_j)$$

where (x_j, z_j) represents the center of the basis function $\phi_j(x, z)$. If the basis functions are constructed with tensor products of basis function of different variables, we have

$$\phi_j(x, z) = \chi_\ell(x)\zeta_m(z)$$

where j denotes the index pair (ℓ, m), and $\chi(x)$ and $\zeta(z)$ are basis functions for dimension x, z respectively.

By selecting a set of collocation points $\mathcal{S} := \{(x_i, z_i)\}_{i=1}^{I}$, we apply the collocation method defined in Equation (3.1) and (3.2) to the system of equations (4.25), (4.26) and (4.27), to obtain the following linear system

$$DK = F,$$

such that D is the $I \times J$ system matrix, K is the $J \times 1$ coefficient vector, and and F is the $I \times 1$ right-hand side vector.

The domain of the problem is $[0, L] \times [0, H]$. The collocation points are selected on a regular grid with grid size $\Delta x = \Delta z$. [1] Let $N = L/\Delta x$ and $M = H/\Delta x$, and denote $x_n = n \times \Delta x$ for $n = 0, 1, \cdots, N$. For simplicity, assuming the OHC feedback distance $\Delta = \tau \Delta x$ for some integer $\tau < N$, Equation (4.29) gives

$$Q(x_n + \tau \times \Delta x) - \alpha Q(x_n) = \alpha P(x_n), \quad \text{for } n = 0, 1, \cdots, N - \tau. \tag{4.31}$$

Let $\mathscr{P}, \mathscr{Q}$ denote the column vector of $P(x, z)$ and $Q(x)$ evaluated on the collocation

[1] with special boundary treatment for spline basis functions. Same in the following passages.

points on the BM boundary, it follows

$$B\mathscr{Q} = C\mathscr{P}. \tag{4.32}$$

The matrix B has 1's on its diagonal, $B(n+\tau, n) = -\alpha$ for $n = 0, 1, \cdots, N-\tau$, and zeros everywhere else. The matrix C is a lower triangular matrix with $C(n+\tau, n) = \alpha$ for $n = 0, 1, \cdots, N-\tau$ and zero everywhere else. It is obvious that $B + C$ produces the identity matrix Id of size $(N+1) \times (N+1)$. For the sake of simplicity, the discretization procedure in Equation (4.31) is applied directly to the spline collocation schemes despite the irregularities at the boundaries. As we can see in the experiments, the straight-forward adaptation still produces reasonable results.

Because matrix B is invertible, Equation (4.32) gives

$$\mathscr{Q} = B^{-1}C\mathscr{P}. \tag{4.33}$$

Let $\mathscr{U}$ denote the vector of BM displacement function $U(x)$ evaluated at BM collocation points. Equation (4.33) and (4.28) gives

$$(B^{-1}C + Id)\mathscr{P} = (-\omega^2 M + i\omega R + S)\mathscr{U}$$

where the matrices M, R and S are diagonal matrices with m, s, and $S(n, n) = s(n \times \Delta x)$. It follows

$$\mathscr{U} = E\mathscr{P} \tag{4.34}$$

where $E = (-\omega^2 M + i\omega R + S)^{-1}(B^{-1}C + Id)$. Let $\tilde{D}$ represent the part of the system matrix D created with collocation points on the BM boundary, and let $\check{D}$ represent the rest of the system matrix. Equation (4.27) and (4.34) gives

$$\tilde{D}K + 2\rho\omega^2 E\mathscr{P} = 0$$

Let $\tilde{\Gamma}$ denote the reconstruction matrix for BM boundary collocation points. It follows

$$(\tilde{D} + 2\rho\omega^2 E\tilde{\Gamma})K = 0$$

Let $\check{F}$ represent the right-hand size vector of collocation points which are not on the BM boundary. We derive the following linear system that incorporate OHC feedback

force and the BM spring system

$$\begin{bmatrix} \check{D} \\ \tilde{D} + 2\rho\omega^2 E\tilde{\Gamma} \end{bmatrix} K = \begin{bmatrix} \check{F} \\ 0 \end{bmatrix} \tag{4.35}$$

In this thesis, we restraint the number of basis functions to be the same as the number of collocation points. The coefficient vector K is thus computed as the inverse of the system matrix times the right-hand size vector. Least square solutions were also attempted, but the discussion is excluded from this thesis because only poor results were obtained.

Simulation Parameters

Parameters	Symbol	Magnitude	Unit
Membrane density	m	0.07	g/cm^2
Fluid density	ρ	1	g/cm^3
Length of cochlear	L	3.5	cm
Height of cochlear	H	0.1	cm
Resistance	r	0.07	$g/(cm^2 \cdot ms)$

Table 4.1: Simulation parameters for spatial cochlear model.

Table 4.1 lists the general parameters used throughout the spatial simulation. The OHC tilt Δ is chosen to be the same as the grid width Δx throughout spatial experiments. The parameters has the same value as in [39], so that the results are directly comparable.

4.2.1 Results and Discussions

Comparison Between Basis Functions

This experiment focus on comparing the effect of using different basis functions with their corresponding collocation schemes. The input frequency is fixed to be 4.5 kHz, and the input magnitude is fixed to be 40 dB SPL. Four types of basis functions are used

1. Multiquadric radial basis function (MQRBF). The shape parameter ϵ in this

experiment is chosen to be

$$\epsilon = \frac{1}{0.815d}, \quad \text{where } d = \frac{1}{J} = \sum_{j=1}^{J} d_j$$

and d_j is the distance from the jth center from its nearest neighbor. The selection of shape parameter is recommended by Hardy in [31]. Other parameter selection strategies, such as the leave-one-out-cross-validation (LOOCV) may lead to better performance, yet we do not pursue that in this thesis. The collocation points are selected on a regular grid with grid size $\Delta x = 0.05, 0.025$ and 0.01, and the function centers coincide with the collocation points. Because regular grids are used for collocation points and function centers, d is obviously the grid width Δx.

2. Gaussian radial basis function (GRBF). The shape parameter is chosen to be

$$\epsilon = \frac{1}{\sqrt{2}\Delta x}$$

so that the GRBF corresponds to normal distribution with Δx as the standard deviation. As a result, three collocation points are sampled within one standard deviation. The effect can be compared with the spline basis function collocation schemes where three collocation points are also sampled inside one basis function. The collocation points and the function centers are identical to the MQRBF case.

3. Quadratic spline basis function (QS). The collocation scheme is described in the previous chapter. Because the spline basis function has finite support, the system matrix is sparse, allowing finer grid size to be used. The grid width is chosen as $\Delta x = 0.025, 0.01$ and 0.005.

4. Cubic spline basis function (CS). The collocation scheme is described in the previous chapter. The grid width is chosen as the same as in the QS case.

Because the spatial cochlear model does not have a known analytical solution, the following criteria are used to evaluate the accuracies of spatial solutions.

1. κ, the condition number of the system matrix. The condition number reflects the stability of the solution with respect to changes in the input. Because the machine epsilon of a double variable, the accuracy of the direct solution of a

linear system with condition number close to or larger than 1e+16 is questionable. We consider that a matrix with large condition number, say 1e+10, may yield unreliable solutions.

2. x_{cp}, the location of the characteristic place (CP). x_{cp} is defined as

$$x_{\text{cp}} = \arg\max_x |U(x)|$$

where $|U(x)|$ is the complex modulus of the BM displacement given a pure-tone input of frequency f. As we found out in experiments, x_{cp} often deviates from the reference CP location deduced by the BM stiffness function, which is

$$x_{\text{ref}} = cp(f) = 3.5 \cdot (1 - (4.83)^{-1} \cdot \log((f + 0.45)/0.456)).$$

Because the cochlear model we study is a drastic simplification of the actual cochlea, plus that numerical errors are unavoidable in discretization, we believe small differences between x_{cp} and x_{ref} are normal and acceptable. A more important property is the exponential mapping between x_{cp} and the input frequency, which demonstrates the main function of the cochlea as a frequency analyzer.

3. $|U(x_{\text{cp}})|$, the magnitude of BM displacement at CP. According to [39, 46, 26], the BM displacement is at the range of fractions of a nanometer (nm) in a passive cochlea, and is magnified for about 100 times when active element is present.

4. $\Xi(x_{\text{cp}})$, energy concentration around CP. The energy concentration is defined as the percentage of energy distributed in the interval $[x_{\text{cp}} - \delta x, x_{\text{cp}} + \delta x]$:

$$\Xi(x_{\text{cp}}) = \frac{\int_{x_{\text{cp}}-\delta x}^{x_{\text{cp}}+\delta x} |U(x)|^2 \mathrm{d}x}{\int_0^L |U(x)|^2 \mathrm{d}x}. \tag{4.36}$$

Throughout this thesis, δx is fixed as 0.05 cm, and is thus omitted from the notation. Energy concentration represents the frequency selectivity of the cochlear model. Cochlea maps the frequency of a pure-tone input to the vibration of a certain part of the BM, and therefore a large portion of the BM energy should distribute around the CP. The addition of OHC active feedback system should increase frequency selectivity of the cochlea, which boosts the energy concentration further.

5. Shape of BM displacement profile and cochlear fluid pressure. A pure-tone signal produces a traveling wave within the cochlea, which consists of a long wavelength section close to the basal end, a short wavelength section close to the CP, and a sharp cut-off after the CP (The "long-short-cut-off" shape. See Figure 2.2). Because it is difficult to quantify the shape characteristics, qualitative observation were made based on the BM displacement profile and cochlea pressure distribution.

Figure 4.4 and 4.5 show the pressure distribution and the BM profiles of the solutions obtained with different basis functions. The details of the experiments are listed in Table 4.2 and 4.3. Below are the discussions of the results by basis functions.

1. MQRBF. Judging from the shape of the pressure map and BM profile of the passive model, the solution is partially correct. The long wavelength region, short wavelength region and the sharp cut-off are observed in the graph. However, the CP location is drastically away from the reference point. In the active model, a boost of BM displacement and energy concentration is observed, but the amplification is beyond reasonable range. For the active model with grid width $\Delta x = 0.01$ cm, The magnitude of BM displacement is 2 mm, a number greater than the height of the cochlear duct. The erroneous result is probably due to the large condition number of the system matrix. As it is indicated in the Table 4.2 and 4.3, the MQRBF basis seems very sensitive to the addition of OHC feedback factor. The change of grid size also tend to greatly alter the simulation result.

2. GRBF. The pressure distribution of the passive model does not show any significant concentration of fluid pressure. Although the BM displacement has it peak close to the reference CP location, the waveform does not comply with the "long-short-cut-off" shape. In the solution of the active model, concentration of pressure and BM displacement is clearly observed near the reference CP location. However, for the active model with grid width $\Delta x = 0.01$ cm, the magnitude of BM displacement is a lot larger than the expected range. Worse still, a decrease in energy concentration is observed in the active model solution for $\Delta x = 0.05$ and 0.025. As we can see in the tables, although the solutions using GRBF produce x_{cp} closer to the reference CP, and have a smaller condition number, the simulation result is still far from ideal.

3. QS. In the passive solution, the BM displacement profile clearly demonstrates a "long-short-cut-off" pattern, with the maximum BM displacement close to

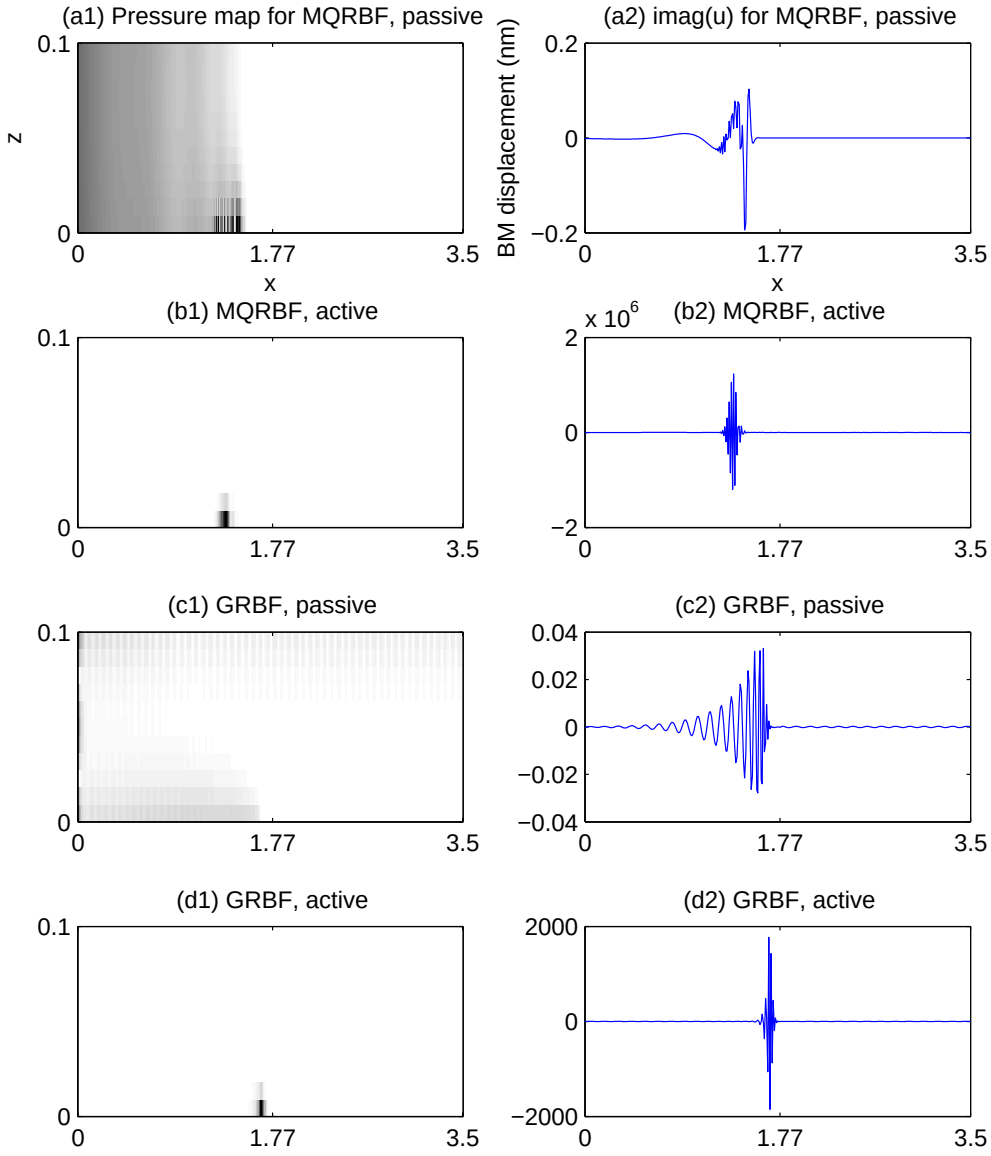

Figure 4.4: Pressure map and BM displacement for global RBFs.
The input signal is a 4.5 kHz, 40 dB SPL pure-tone. Grid width $\Delta x = 0.01$. The left column shows the pressure map within the simulated cochlear model, where darker area represents larger magnitude. The right column shows the imaginary part of the corresponding BM profile. Axis labels are shown for graphs on the first row only. The reference CP (1.77 cm) is marked in the graphs.

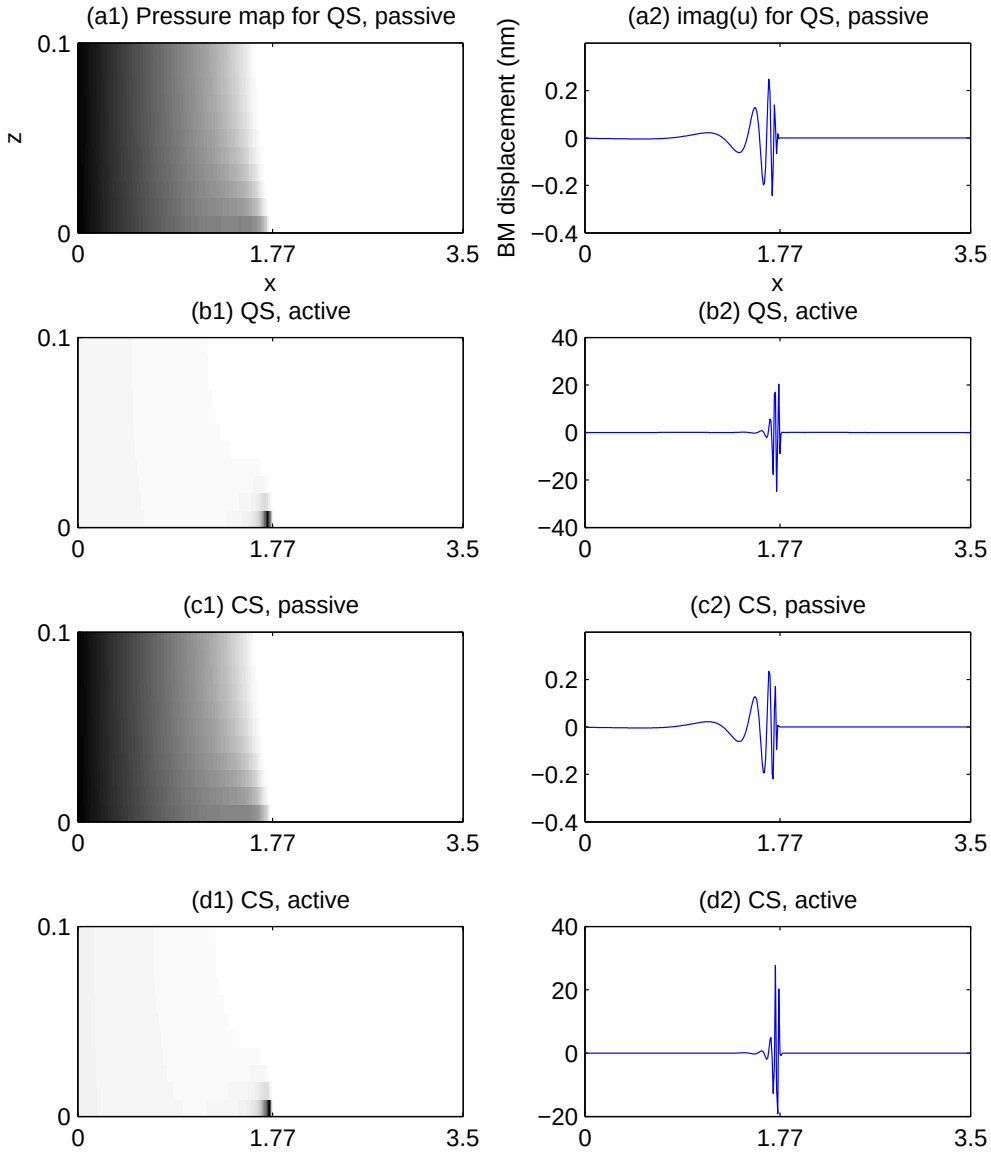

Figure 4.5: Pressure map and BM displacement for spline basis functions. The input signal is a 4.5 kHz, 40 dB SPL pure-tone. Grid width $\Delta x = 0.01$. The left column shows the pressure map within the simulated cochlear model, where darker area represents larger magnitude. The right column shows the imaginary part of the corresponding BM profile. Axis labels are shown for graphs on the first row only. The reference CP (1.77 cm) is marked in the graphs.

Basis	Δx	κ	x_{cp}	$\lvert U(x_{\text{cp}})\rvert$	$\Xi(x_{\text{cp}})(\%)$
MQRBF $\epsilon = 24.54$	0.05	1.63e+7	0.87	0.0164	50.86%
MQRBF $\epsilon = 49.08$	0.025	9.95e+7	1.23	0.0797	53.15%
MQRBF $\epsilon = 122.7$	0.01	5.52e+8	1.48	0.2665	63.27%
GRBF $\epsilon = 14.14$	0.05	6.50e+4	1.25	0.0485	42.27%
GRBF $\epsilon = 28.28$	0.025	2.93e+5	1.48	0.0622	57.71%
GRBF $\epsilon = 70.71$	0.01	1.99e+6	1.64	0.0488	39.31%
QS	0.025	4.09e+5	1.68	0.3499	52.28%
QS	0.01	4.33e+6	1.7	0.269	51.43%
QS	0.005	3.16e+7	1.7	0.2621	53.08%
CS	0.025	5.37e+5	1.69	0.3541	51.55%
CS	0.01	5.01e+6	1.7	0.2629	53.99%
CS	0.005	3.52e+7	1.7	0.2597	53.11%

Table 4.2: Comparison between basis functions, passive model. Δx and x_{cp} is given in cm, while $\lvert U(x_{\text{cp}})\rvert$ is given in nm.

Basis	Δx	κ	x_{cp}	$\lvert U(x_{\text{cp}})\rvert$	$\Xi(x_{\text{cp}})(\%)$
MQRBF $\epsilon = 24.54$	0.05	1.98e+9	0.91	1.62e+0 (9.81e+1)	48.82% (-4.01%)
MQRBF $\epsilon = 49.08$	0.025	7.73e+11	1.11	2.89e+2 (3.62e+2)	70.18% (32.04%)
MQRBF $\epsilon = 122.7$	0.01	6.69e+15	1.36	1.39e+6 (5.20e+6)	95.21% (50.48%)
GRBF $\epsilon = 14.14$	0.05	1.59e+6	1.78	1.91e+0 (3.83e+1)	25.73% (-39.13%)
GRBF $\epsilon = 28.28$	0.025	1.34e+8	1.56	4.29e+1 (6.89e+2)	55.58% (-3.69%)
GRBF $\epsilon = 70.71$	0.01	6.09e+10	1.68	2.35e+3 (4.81e+4)	99.39% (152.84%)
QS	0.025	5.39e+5	1.7	1.96e+1 (5.51e+1)	79.9% (52.83%)
QS	0.01	4.92e+6	1.76	3.20e+1 (1.18e+2)	95.62% (85.92%)
QS	0.005	2.85e+7	1.76	2.46e+1 (9.28e+1)	98.47% (85.51%)
CS	0.025	7.63e+5	1.77	1.94e+1 (5.37e+1)	64.79% (25.68%)
CS	0.01	5.59e+6	1.75	4.02e+1 (1.52e+2)	98.58% (82.59%)
CS	0.005	3.17e+7	1.76	2.26e+1 (8.61e+1)	98.35% (85.18%)

Table 4.3: Comparison between basis functions, active model ($\alpha = 0.36$).
Δx and x_{cp} is given in cm, while $\lvert U(x_{\text{cp}})\rvert$ is given in nm. Number in parentheses denote the boost amount from the passive case.

the reference CP location. In the pressure map, a clear cut-off is found after the reference CP, showing that most of the pressure energy is absorbed by the BM segment before the CP. In the active solution, the BM displacement and the pressure distribution is condensed into a small region about the reference CP, showing high frequency selectivity. The BM displacement is magnified for about 100 times after the active element is added, which matches the observed difference between impaired and normal ears [26, 46]. The model solutions using QS ideally matches the physiological characteristics of the cochlea. Additionally, solutions using QS seems to be stable with the variation of grid size.

4. CS. The performance of the CS basis functions is nearly identical to the QS basis functions. Except for some small numerical difference, the results are essentially the same.

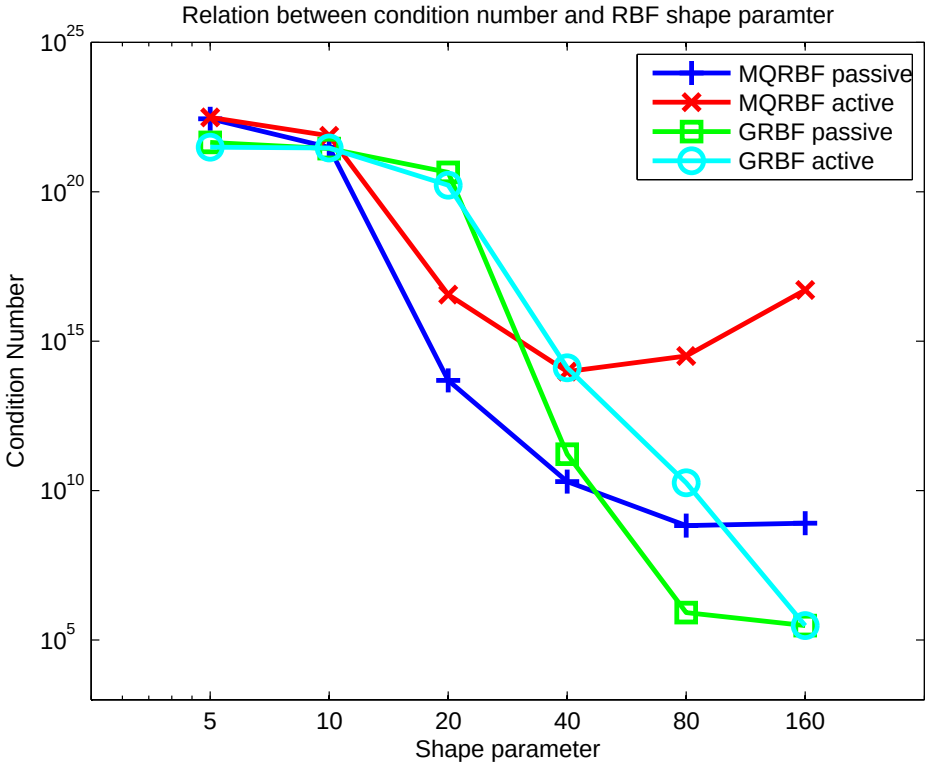

Figure 4.6: Relationship between shape parameter of RBFs and the condition number of the system matrix. $\Delta x = 0.01$

The relationship between the RBF shape parameter ϵ and the system matrix condition number κ is further investigated; the results are shown in Figure 4.6. MQRBF

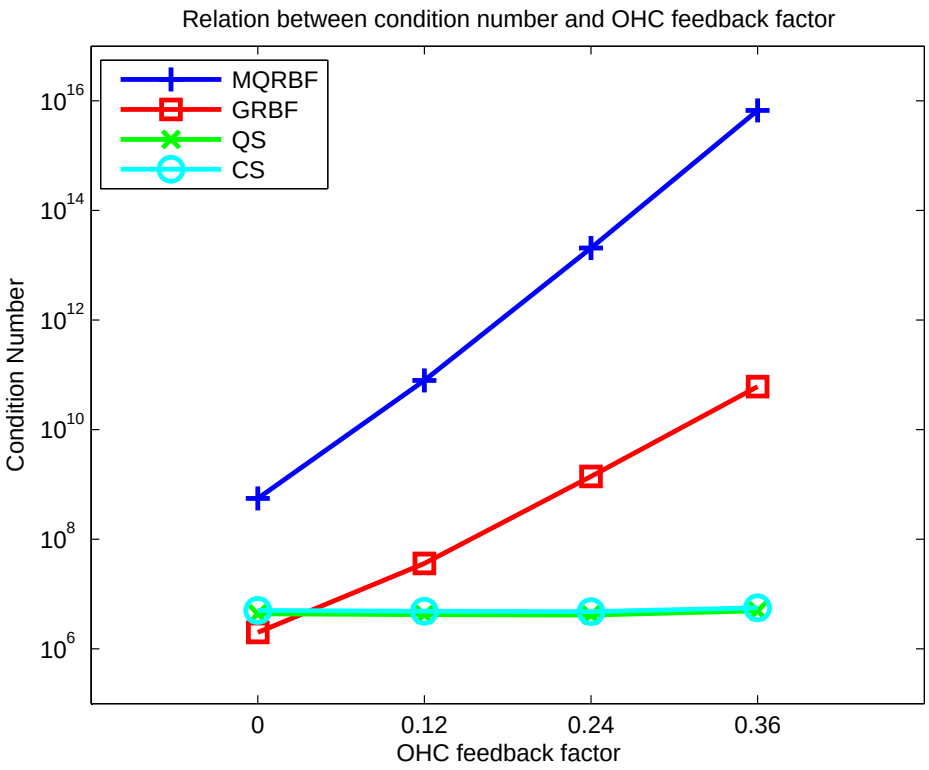

Figure 4.7: Relationship between OHC feedback factor and the condition number of the system matrix. $\Delta x = 0.01$

and GRBF is compared side-by-side on the same grid with $\Delta x = 0.01$. As we see in the graph, a larger shape parameter generally result in a smaller condition number, except for using MQRBF on the active model, where the condition number rise again after $\epsilon = 40$. Generally speaking, a larger shape parameter results in a more localized basis function. The condition number is decreased because the columns of the system matrix are less linearly dependent, while the target function is worse represented because the basis functions have less coverage. However, such a trend is not preserved for using MQRBF on the active model. The added OHC active feedback factor introduces a Dirichlet boundary condition on the BM boundary (overall it is a Robin boundary condition), and because the value of the MQRBF increases as the collocation point moves away from the function center, the the columns of the system matrix is dominated by the homogeneous OHC active feedback factor when the shape parameter is large, rendering the matrix linearly dependent. Additionally, we discovered that reasonable results are rarely obtained for global RBF with a large shape parameters after repeated experiments. It suggests that global RBF may not

be an ideal type of basis functions for this spatial cochlear model.

Figure 4.7 shows the relationship between the OHC active feedback factor α and the system matrix condition number κ. The grid size is 0.01 cm, and the shape parameter for MQRBF and GRBF is 122.7 and 70.71 respectively. It can be observed that MQRBF is indeed very sensitive to the introduction of OHC feedback factor. For a fixed grid and a fixed shape parameter, a larger α results in a larger κ, quickly rendering the linear system unstable. GRBF is less affected by the change of α, yet κ does increase with α in general. The condition number for QS and CS is largely unaffected by the change of α due to their finite support.

In conclusion, we discussed the effects of solving the spatial cochlear model using four types of basis functions. It is discovered that the global RBF functions are generally disadvantageous, because inaccurate solution are obtained for large grid width and large shape parameter, while small grid width and small shape parameter renders the solution unstable. We believe the cause is two-fold: 1. To find a highly localized solution (high frequency selectivity) in a highly elongated model (35:1), it requires a fine grid and a small shape parameter to produce a localized result, which consequently renders the system matrix linearly dependent as the collocation points are arranged in tightly placed arrays. 2. The introduction of homogeneous OHC feedback factor linearizes the boundary condition, deteriorating the system matrix further because global RBFs are sensitive to boundary conditions. On the other hand, the spline basis functions give stable results which agree with physiological data and past works. They serve as ideal basis functions for future experiments.

Response to Pure-Tone Inputs

Figure 4.8 shows the so-called iso-intensity graph for the spatial cochlear model, computed using the CS basis function with grid width $\Delta x = 0.01$. Pure-tone signals of same sound pressure level but different frequencies are used as input, and modulus of the BM displacement are taken as output. The graph shows the system response for 40 dB SPL signals of frequencies 18, 12.73, 9, 6.36, 4.5, 3.18 and 2.25 kHz, peaking at BM location 2.19, 1.98, 1.76, 1.52, 1.28, 1.04 and 0.8 cm, respectively. The vertical axis is the BM displacements in logarithmic scale, and the horizontal axis is the distance to the oval window. Dashed lines represent the BM displacement of the passive model with same input signals.

The graph demonstrates traits of the spatial cochlear model that comply with physiological observations. First of all, the cochlea as a frequency analyzer maps the frequency of a input signal to a certain location (CP) of the BM. As the input

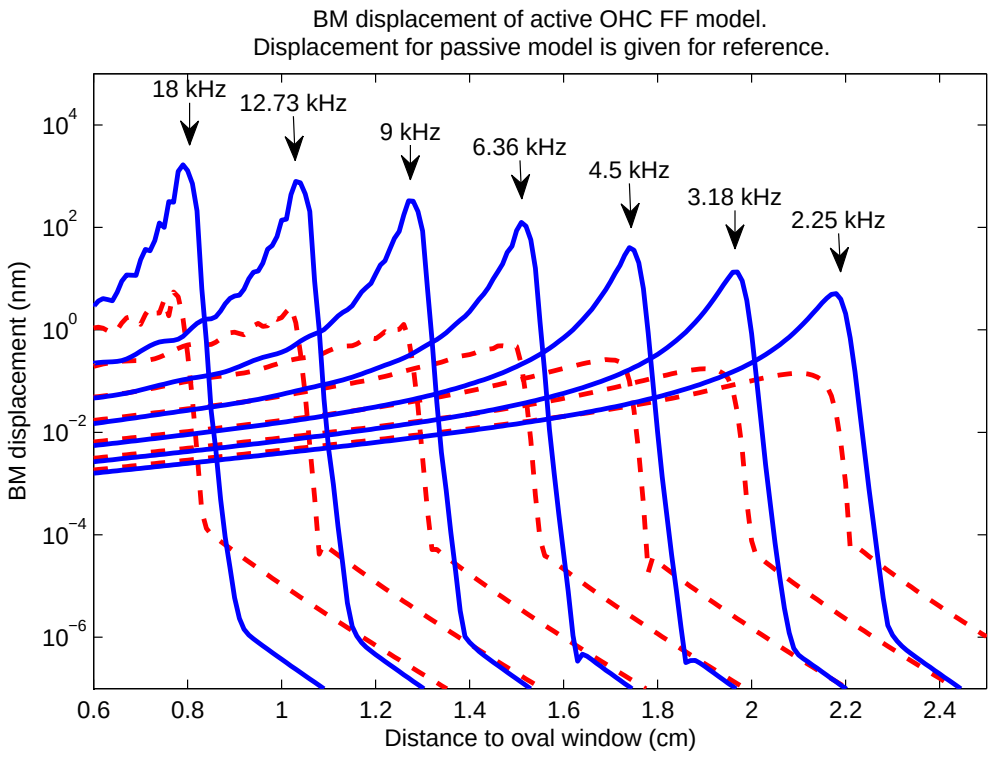

Figure 4.8: BM displacement magnitude for input signal of different frequencies.

increase exponentially in frequency, the CP moves linearly towards the basal end (oval window). That can be observed from the graph where the BM displacement peaks are placed linearly for exponential growth of frequencies. Second, the addition of OHC active feedback factor drastically improves the frequency selectivity and peak magnitude, conforming to the observations made in live cochlea [26, 46] and the experiment results in [45, 46]. Third, the sensitivity grows as the input frequency gets higher. Such a characteristic coincide with our sense of hearing, as we are generally more sensitive to high frequency sounds (sirens, blackboard scratches) than low frequency sounds (footsteps, bass guitar).

Figure 4.9 shows the frequency–location map of the solutions presented in Figure 4.8. The vertical axis is the input frequency in logarithmic scale, and the horizontal axis represent the distance of the CP location to the oval window. As we can observe, the frequency–location map obtained from both the passive and the active spatial model conform well with physiological data in [28, 44].

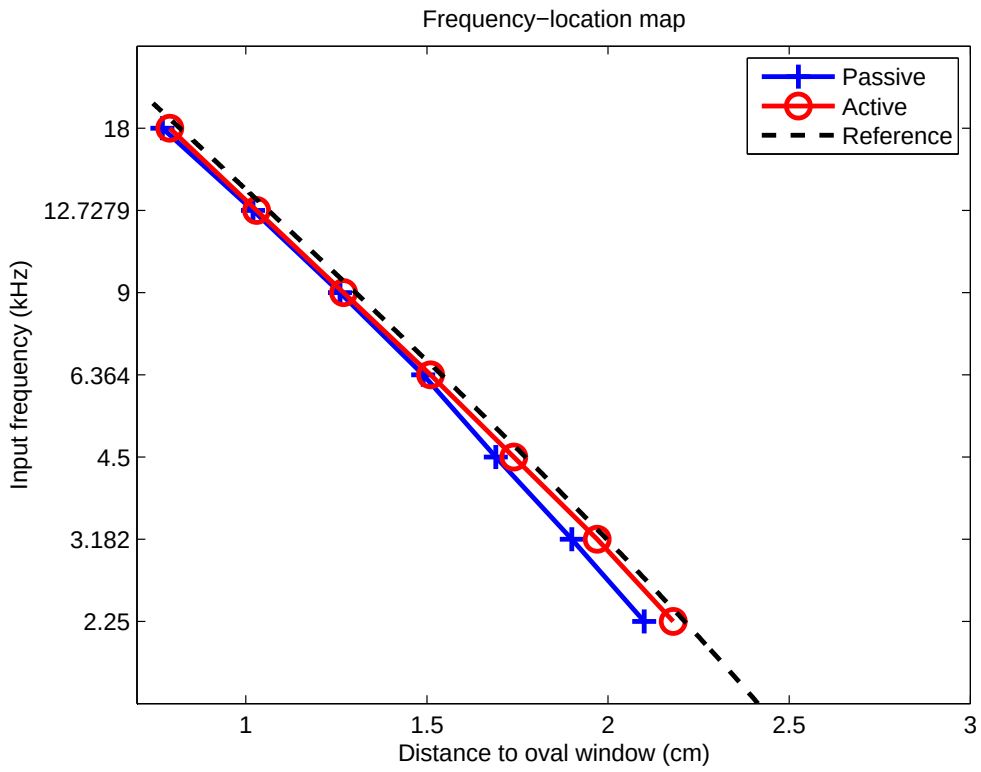

Figure 4.9: Frequency-location map of the spatial cochlear model.

4.3 Temporal-Spatial Model Solution

Solving the temporal-spatial model requires proper discretization in both space and time domain. By the method of separation of variables, $p(x, z, t)$ is given as

$$p(x, z, t) = \sum_{j=1}^{J} k_j(t)\phi_j(x, z)$$

The spatial discretization is given in the previous section. The following discusses the temporal discretization for Equation (4.22) and (4.23).

Assuming that collocation points are selected on a regular grid, and $\Delta = \tau\Delta x$. Denoting $x_n = n \times \Delta x$ for $n = 0, 1, \cdots, N$, Equation (4.23) gives

$$q(x_n + \tau\Delta x, t) - \alpha(x_n, u, t)q(x_n, t) = \alpha(x_n, u, t)(p(x_n, 0, t) - F_{\text{in}}(x_n, t))$$

where $F_{\text{in}}(x, t) = 2\rho T_m p_e(t)(L - x)$. Let $\mathscr{Q}(t), \mathscr{P}(t)$ and $\mathscr{F}_{\text{in}}(t)$ denotes the column

vector for $q(x_n,t), p(x_n,0,t)$ and $F_{\text{in}}(x_n,t)$ respectively. It follows

$$B\mathscr{Q}(t) = C(\mathscr{P}(t) - \mathscr{F}(t))$$

where matrices B and C are very similar to the spatial case except for variable α values. Because matrix B is invertible, it can be further deduced

$$\mathscr{Q}(t) = B^{-1}C(\mathscr{P}(t) - \mathscr{F}(t)). \tag{4.37}$$

Define $\mathscr{U}(t)$ as the vector of $u(x,t)$ evaluated at BM boundary collocation points. Define $G = B^{-1}C + Id$, where Id is the $(N+1)\times(N+1)$ identity matrix. Putting Equation (4.37) into Equation(4.22) gives

$$B^{-1}C(\mathscr{P}(t) - \mathscr{F}_{\text{in}}(t)) + \mathscr{P}(t) = M\mathscr{U}_{tt}(t) + R\mathscr{U}_t(t) + S\mathscr{U}(t) + \mathscr{F}_{\text{in}}(t)$$

By simplification,

$$G(\mathscr{U})\mathscr{P}(t) - M\mathscr{U}_{tt}(t) = R\mathscr{U}_t(t) + S\mathscr{U}(t) + G(\mathscr{U})\mathscr{F}_{\text{in}}(t). \tag{4.38}$$

Similar to the spatial case, let $\tilde{D}$ and $\tilde{\Gamma}$ denote the BM boundary differentiation and reconstruction matrices. Equation (4.21) and (4.38) gives

$$(G(\mathscr{U})\tilde{\Gamma} - \frac{1}{2\rho}M\tilde{D})K(t) = R\mathscr{U}_t(t) + S\mathscr{U}(t) + B^{-1}C + G(\mathscr{U})\mathscr{F}_{\text{in}}(t). \tag{4.39}$$

The relationship among vector $K(t)$, $\mathscr{U}_t(t)$ and $\mathscr{U}(t)$ is specified by a second order differential equation in time domain. To make the problem applicable to common numerical integration schemes which are typically written for first order differential equations, we need to introduce an intermediate variable $\mathscr{V}(t)$. Define $\mathscr{V}(t) = \mathscr{U}_t(t)$, and thus $\mathscr{V}_t(t) = \mathscr{U}_{tt}(t)$. Let the superscript denote the time step of a variable. For example, $\mathscr{U}^n$ denotes vector $\mathscr{U}(t)$ at the nth time step. By the second order backward differencing formula **BFD2**, we obtain the following two equations

$$\mathscr{U}^{n+2} = \frac{4}{3}\mathscr{U}^{n+1} - \frac{1}{3}\mathscr{U}^n + \frac{2\Delta t}{3}\mathscr{V}^{n+2} \tag{4.40}$$

$$\mathscr{V}^{n+2} = \frac{4}{3}\mathscr{V}^{n+1} - \frac{1}{3}\mathscr{V}^n + \frac{2\Delta t}{3}\mathscr{U}_{tt}^{n+2} \tag{4.41}$$

where Δt is the time step size. Note that we have $\mathscr{U}_{tt}^{n+2} = \tilde{\Gamma}K^{n+2}$. Combining

the equations (4.39), (4.40), and (4.41), we derive

$$\begin{aligned}(G(\mathscr{U}^{n+2})\tilde{\Gamma}-\frac{1}{2\rho}M\tilde{D})K^{n+2} = R(&\frac{4}{3}\mathscr{V}^{n+1}-\frac{1}{3}\mathscr{V}^{n}+\frac{2\Delta t}{3}\frac{1}{2\rho}\tilde{D}K^{n+2})\\ &+S(\frac{4}{3}\mathscr{U}^{n+1}-\frac{1}{3}\mathscr{U}^{n}+\frac{2\Delta t}{3}(\frac{4}{3}\mathscr{V}^{n+1}-\frac{1}{3}\mathscr{V}^{n}+\frac{2\Delta t}{3}\frac{1}{2\rho}\tilde{D}K^{n+2}))\\ &+G(\mathscr{U}^{n+2})F_{\text{in}}^{n+2}.\end{aligned}$$

Grouping terms with K^{n+2} on the left-hand side of the equation, and simplifying the coefficients, it follows,

$$\begin{aligned}&(G(\mathscr{U}^{n+2})\tilde{\Gamma}-\frac{1}{2\rho}M\tilde{D}-\frac{\Delta t}{3\rho}R\tilde{D}-\frac{2\Delta t^2}{9\rho}S\tilde{D})K^{n+2} =\\ &R(\frac{4}{3}\mathscr{V}^{n+1}-\frac{1}{3}\mathscr{V}^{n})+S(\frac{4}{3}\mathscr{U}^{n+1}-\frac{1}{3}\mathscr{U}^{n}+\frac{2\Delta t}{3}(\frac{4}{3}\mathscr{V}^{n+1}-\frac{1}{3}\mathscr{V}^{n}))+G(\mathscr{U}^{n+2})\mathscr{F}_{\text{in}}^{n+2}\end{aligned} \tag{4.42}$$

Let $\tilde{\tilde{D}}$ denote the left-hand side of equation 4.42, and let $\tilde{\tilde{F}}$ denote the right-hand side. Let $\check{D}$ and $\check{F}$ denote the differentiation matrix and the right-hand side vector for collocation points not on the BM boundary. Combining the spatial and temporal discretization we obtain the following linear system

$$\begin{bmatrix}\check{D}\\ \tilde{\tilde{D}}^{n+2}\end{bmatrix}K^{n+2}=\begin{bmatrix}\check{F}\\ \tilde{\tilde{F}}^{n+2}\end{bmatrix}. \tag{4.43}$$

The value of $\tilde{\tilde{D}}^{n+2}$ is dependent on $G(\mathscr{U}^{n+2})$, where $\mathscr{U}^{n+2}$ is approximated explicitly by the second order Taylor expansion,

$$\mathscr{U}^{n+2}=\mathscr{U}^{n+1}+\Delta t\mathscr{V}^{n+1}+\frac{\Delta t}{2}(\mathscr{V}^{n+1}-\mathscr{V}^{n}).$$

$\tilde{\tilde{F}}^{n+2}$ is determined by the sound pressure input of the system. Once the coefficient vector K^{n+2} is solved, $\mathscr{V}_t^{n+2}$ is calculated by Equation (4.21), which in term updates $\mathscr{V}^{n+2}$ and $\mathscr{U}^{n+2}$ to prepare for the simulation of next time step. The homogenization of the temporal-spatial model allows most of the system matrix and the right-hand side vector to stay constant for the entire simulation. Such a configuration may be exploited for fast matrix inverse to shorten the simulation time [39].

4.3.1 Experiment Setup

Simulation Parameters

Parameters	Symbol	Magnitude	Unit
Membrane density	m	0.07	$\mathrm{g/cm^2}$
Fluid density	ρ	1	$\mathrm{g/cm^3}$
Length of cochlear	L	3.5	cm
Height of cochlear	H	0.1	cm
Resistance	r	0.07	$\mathrm{g/(cm^2 \cdot\ ms)}$
Grid width	Δx	0.025	cm
Time step	Δt	0.0025	ms

Table 4.4: Simulation parameters for spatial cochlear model.

Table 4.4 lists the parameters for the temporal-spatial experiments. The nonlinear gain factor $\alpha(x, u, t)$ is defined in Equation (4.15) with $\gamma = 0.36$ and $\lambda = 0.12$ cm^2. The grid width is fixed to be 0.025 as a compromise between simulation time and numerical accuracy. Cubic spline basis functions are used for their numerical stability shown in the spatial experiments. Δt is chosen as the same as in [39] where proof of convergence for FDM discretization is given. However, we do not prove the convergence of our temporal-spatial solution for cubic spline basis functions.

The input is given as

$$T_m p_e(t) = (1 - e^{-t/t_0}) \sum_{j=1}^{J_m} a_m(\omega_j) A_j \sin(\omega_j t),$$

where $t_0 = 2.0$. This configuration gradually increase the input magnitude as a measure to suppress the undesirable dispersive tail which often appears in the BM displacement. The convergence to a quasi-static state is sped up as a result [39, 75].

Figure 4.10 shows an example of the temporal-spatial simulation result, were a 4.5 kHz, 40 dB SPL pure-tone is used as input. The top graph illustrates the BM velocity profile at $t = 28$ ms, where a "long-short-cut-off" waveform is observed. The middle graph shows the evolution of the BM velocity. The BM location which obtained maximum BM velocity is marked at the vertical axis, while time is given in the horizontal axis. As we can observe that the BM location with maximum velocity changes drastically for the first three milliseconds, after which the profile converges to a quasi-static state where the maximum location only varies within a small range. It can be explained that the dynamic state is the transient period for the pressure

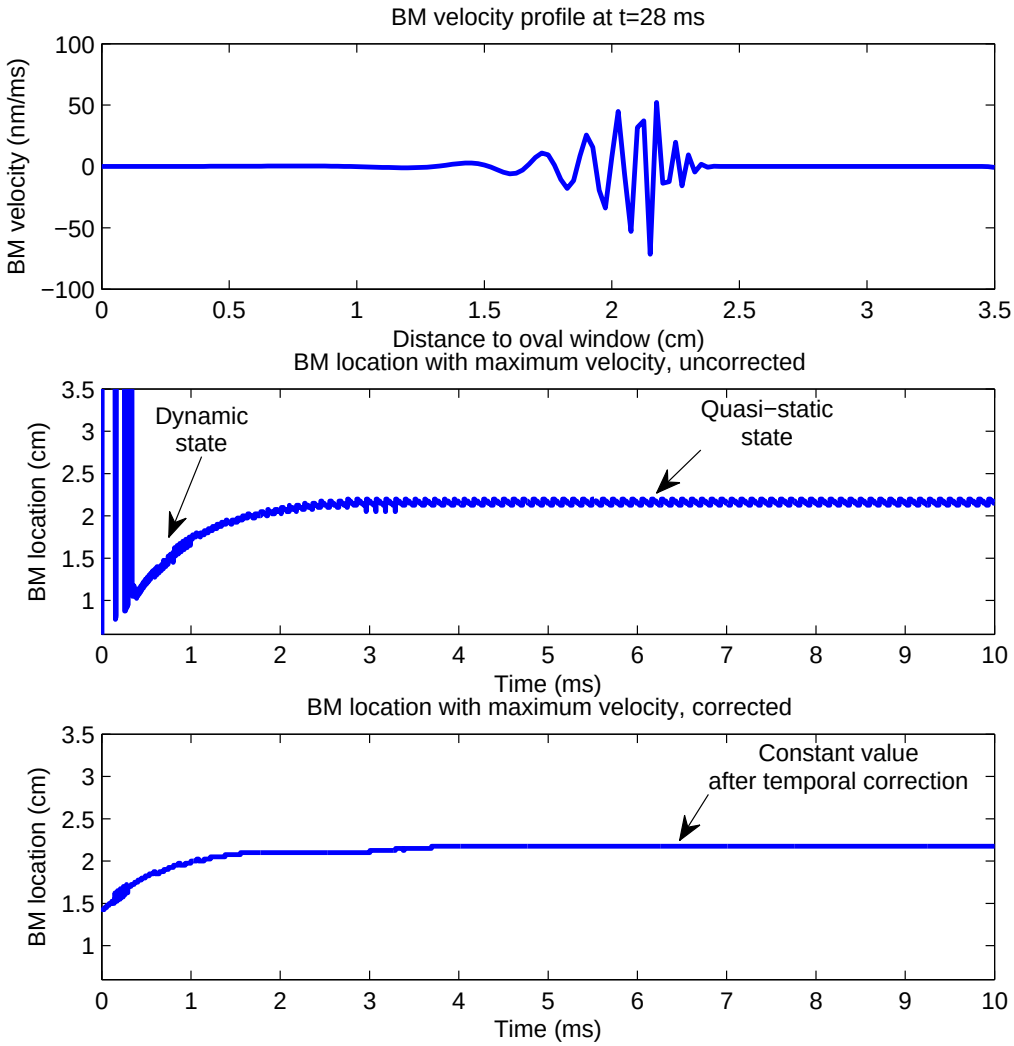

Figure 4.10: Example of temporal-spatial simulation results. Input is a 4.5 kHz, 40 dB SPL pure-tone.

energy to concentrate around the CP, and after the BM attains most of its energy around the CP, the small variation is caused by the vertical movements of the BM spring systems around the CP. To allow quantitative analysis, the BM velocity $v(x,t)$ is corrected by choosing the maximum velocity in a small time window:

$$v_{\mathrm{c}}(x,t) = \max_{t' \in [t-\delta t, t+\delta t]} |v(x,t')|,$$

where $V_{\mathrm{c}}(x,t)$ denotes the corrected BM velocity, and δt is fixed as three cycles of the input frequency. The BM evolution computed with corrected BM velocity is shown in the bottom graph of Figure 4.10, where the corrected BM velocity profile reaches a static state after four milliseconds.

Similar to the spatial model, we define the following values to facilitate the discussion.

1. x_{cp}, the location of the characteristic place (CP). x_{cp} for the temporal-spatial model is defined as

$$x_{\mathrm{cp}} = x_{\mathrm{cp},[t_a,t_b]} = \arg\max_x \frac{1}{t_b - t_a} \int_{t_a}^{t_b} v_{\mathrm{c}}(x,t)\mathrm{d}t$$

   where interval $[t_a, t_b]$ is selected so that the corrected BM velocity profile is in a static state. Through repeated experiments, we discovered that the static state is reach after 20 ms regardless of the input. The interval is therefore chosen to be $[20, 40]$ throughout the discussion.

2. $u_{\mathrm{mean}}(x_{\mathrm{cp}})$, the average of BM displacement at CP, defined as

$$u_{\mathrm{mean}}(x_{\mathrm{cp}}) = \frac{1}{t_b - t_a} \int_{t_a}^{t_b} |u(x_{\mathrm{cp}}, t)|\mathrm{d}t$$

3. $\Xi(x_{\mathrm{cp}})$, energy concentration. The energy concentration around x_{cp} is defined as

$$\Xi(x_{\mathrm{cp}}) = \frac{\int_{x_{\mathrm{cp}}-\delta x}^{x_{\mathrm{cp}}+\delta x} \int_{t_a}^{t_b} E(x,t)\mathrm{d}t\mathrm{d}x}{\int_0^L \int_{t_a}^{t_b} E(x,t)\mathrm{d}t\mathrm{d}x}$$

   where the energy function $E(x,t)$ is given as the energy of individual BM spring systems

$$E(x,t) = \frac{1}{2}mv^2(x,t) + \frac{1}{2}S(x)u^2(x,t).$$

   Similar to the spatial model, the energy concentration around CP reveals the

degree of frequency selectivity for the temporal-spatial mode.

4.3.2 Results and Discussions

Response to Pure-Tone Input

Frequency	γ	x_{cp}	$\lvert u_{\text{mean}}(x_{\text{cp}})\rvert$	$\Xi(x_{\text{cp}})(\%)$
2.25	0	2.28	6.16e-2	17.94%
3.182	0	2.03	6.43e-2	17.95%
4.5	0	1.96	9.95e-2	17.94%
6.364	0	1.88	1.48e-1	18.04%
9	0	1.5	2.78e-1	17.66%
12.7279	0	1.45	8.36e-1	24.57%
18	0	1.05	8.24e-1	24.70%
2.25	0.36	2.45	6.68e-1 (9.85)	34.16% (90.46%)
3.182	0.36	2.3	1.05 (1.53e+1)	37.02% (106.24%)
4.5	0.36	2.18	1.74 (1.65e+1)	41.41% (130.73%)
6.364	0.36	1.93	2.10 (1.32e+1)	46.68% (158.71%)
9	0.36	1.73	4.13 (1.39e+1)	53.86% (205.03%)
12.7279	0.36	1.55	3.73 (3.46)	58.67% (138.80%)
18	0.36	1.28	5.70 (5.92)	58.77% (137.96%)

Table 4.5: Temporal-spatial simulation results of 40 dB SPL pure-tone signals. x_{cp} is given in cm. $\lvert u_{\text{mean}}(x_{\text{cp}})\rvert$ is given in nm. Numbers in parenthesis represents the boost compared to the passive model ($\gamma = 0$).

Table 4.5 lists the experiment results for 40 dB SPL pure-tone signals. The experiments were carried out for input frequencies 2.25, 3.182, 4.5, 6.364, 9, 12.7279, and 18 kHz, on both the passive model ($\gamma = 0$) and the nonlinear active model ($\gamma = 0.36$). The location of the characteristic place, energy concentration, and the average BM displacement are shown. The value gain for adding the nonlinear OHC active feedback factor are listed in parentheses.

It can be observed from Table 4.5 that the inclusion of nonlinear OHC feedback factor enhance the BM vibration and frequency selectivity, as shown by increased

BM displacement value and the energy concentration. However, the addition of active element creates a less significant effect compared to the results from the spatial model,. That is probably due to the saturation property of the nonlinear feedback factor in time simulation. Moreover, adding the the nonlinear element seems to alter the CP location, some phenomenon not observed from the spatial model.

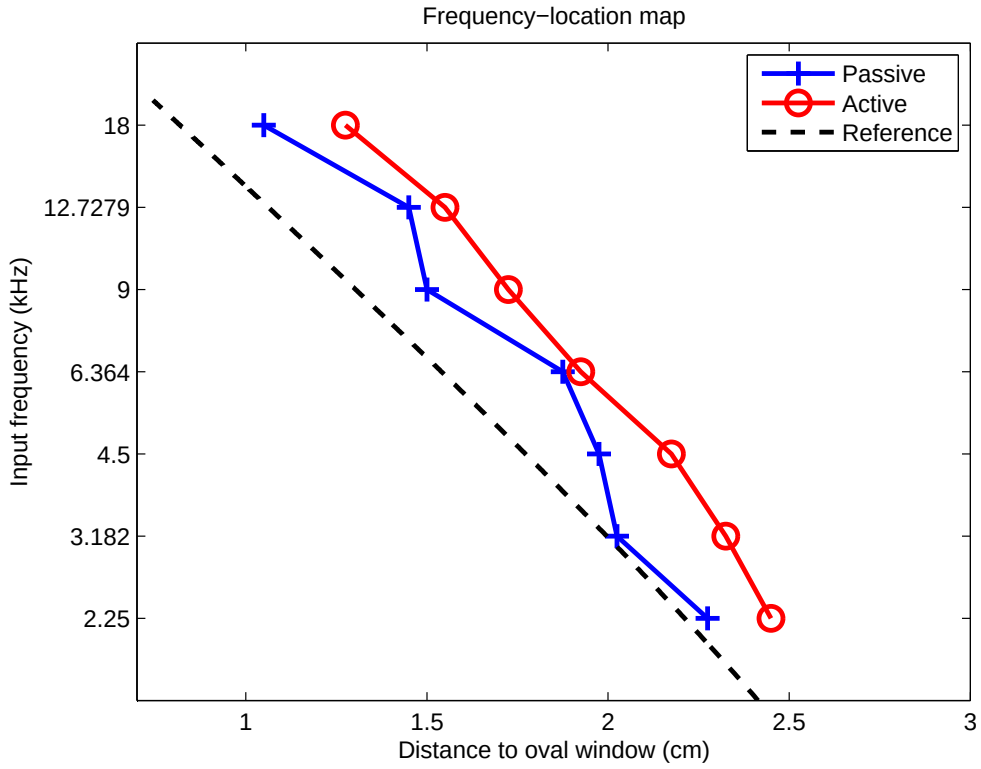

Figure 4.11: Frequency–location map for temporal-spatial simulation.

Figure 4.11 shows the frequency–location map of the temporal-spatial simulations. It can be observed that the temporal-spatial model is capable of mapping pure-tone input frequency to a specific location of the BM boundary. However, the frequency response for the passive model deviates substantially from the reference CP location, and the addition of OHC active feedback factor moves the line further from the reference. The result is significantly different from Figure 4.9 and from the results in [39].

We believe the cause for the discrepancy lies in our method of solution. The pressure-wave created by the pure-tone input propagates much slower than the sound wave in the cochlear fluid. Through the nonlinear OHC feedback system, and through the complex fluid interaction in the two dimensional domain, the frequency content

of the input signal is potentially changed to include low-frequency contents. Such a phenomenon is not captured by the spatial model or the temporal-spatial solution in [39] because the spatial model constraints the fluid pressure $P(x, z)$ and the BM displacement $U(x)$ to be a multiple of the carrying pure-tone signal $e^{i\omega t}$, while the temporal-spatial solution in [39] is algebraically reduced to the solution on the BM boundary for efficiency. However, further study is required to fully determine the effect of the nonlinear OHC feedback factor on the CP location.

Response to Multi-Tone Input

Figure 4.12 shows the simulation results of a multi-tone signal comprised of four pure-tone signals of 2.25, 4.5, 9 and 18 kHz. The top graph shows the BM uncorrected velocity profile at $t = 28$ ms, enveloped by the correct velocity profile. Two clear peaks are observed for input signal of 9 and 18 kHz, while the peaks for lower frequency are not obvious. The bottom graph shows the velocity profile in logarithmic scale, where the four peaks of the input pure-tone signals. An dispersive tail is also observed at the apex end as a result of the termination of the cochlear duct.

The result of multi-tone signal simulation conforms to the results of the spatial model; the cochlear model is more sensitive to high frequency signals than low frequency signals. The observation also complies with our sense of hearing that high frequency signals are more easily distinguished from a complex sound background. Additionally, the presence of high frequency signals saturates the OHC feedback factor, diminishing the sensitivity for low frequency signals.

Response to Transient Input

Figure 4.13 shows the transient response of the temporal-spatial model to a "click" input. The top graph shows the shape of the "click" signal, while the rest of the graphs shows the system response sampled as the BM velocity at $x = 1.5$ cm. It can be observed that, the passive system gives a weak response to the input click, which quickly dies down to zero. Equipped with the OHC active feedback mechanism, the click signal is greatly magnified at about 1 ms. The magnification of the click signal grows compressively with respect to the strength of the input as a result of the saturation of OHC feedback factor. Interestingly, a small, delayed wave lobe resurges at $t = 2.7$ ms, reflecting the complex dynamics of a nonlinear active cochlear model.

The resurgence of the BM response is correlated to the long known phenomenon of otoacoustic emission. Predicted by Thomas Gold in 1948, and experimentally

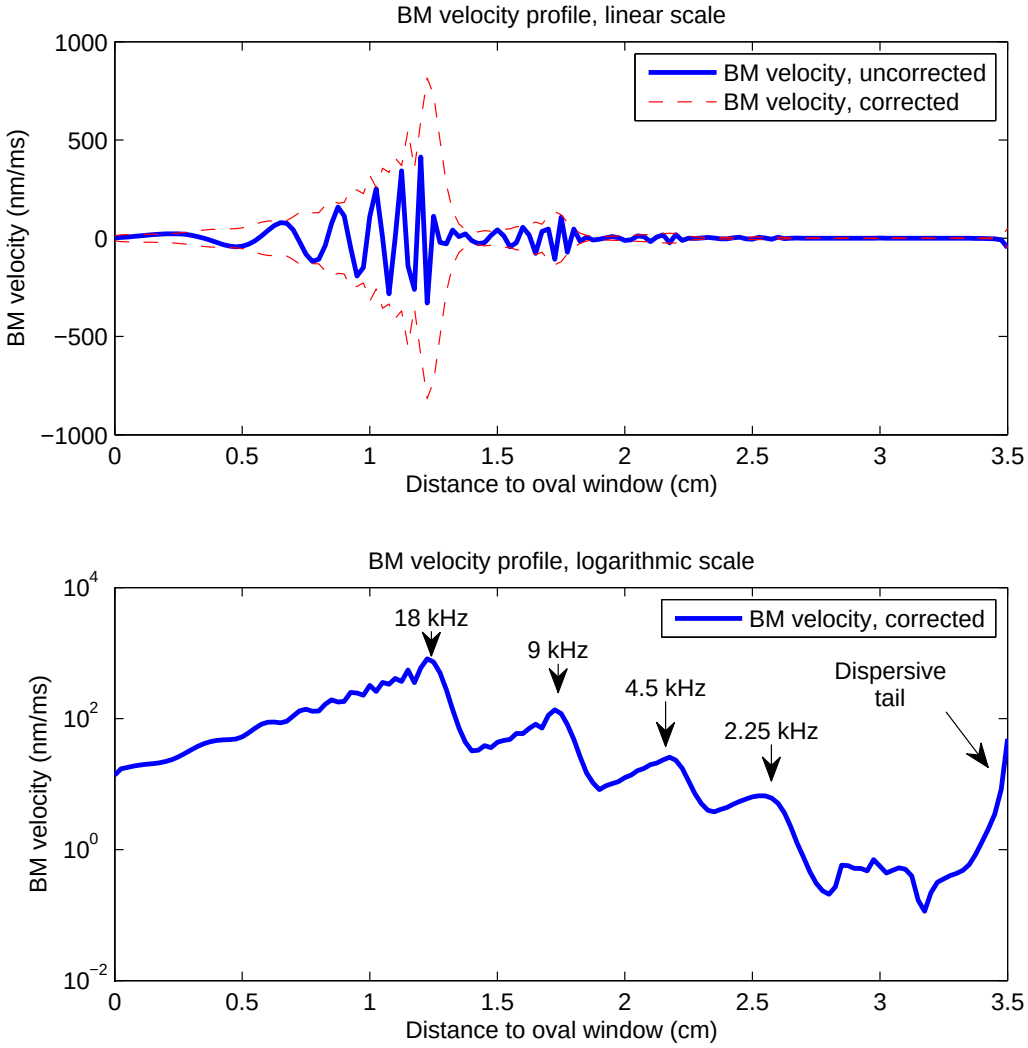

Figure 4.12: Temporal-spatial simulation result at $t = 28$ ms of a multi-tone signal, consisting of 2.25, 4.5, 9, and 18 kHz pure-tone signals at 40 dB SPL.

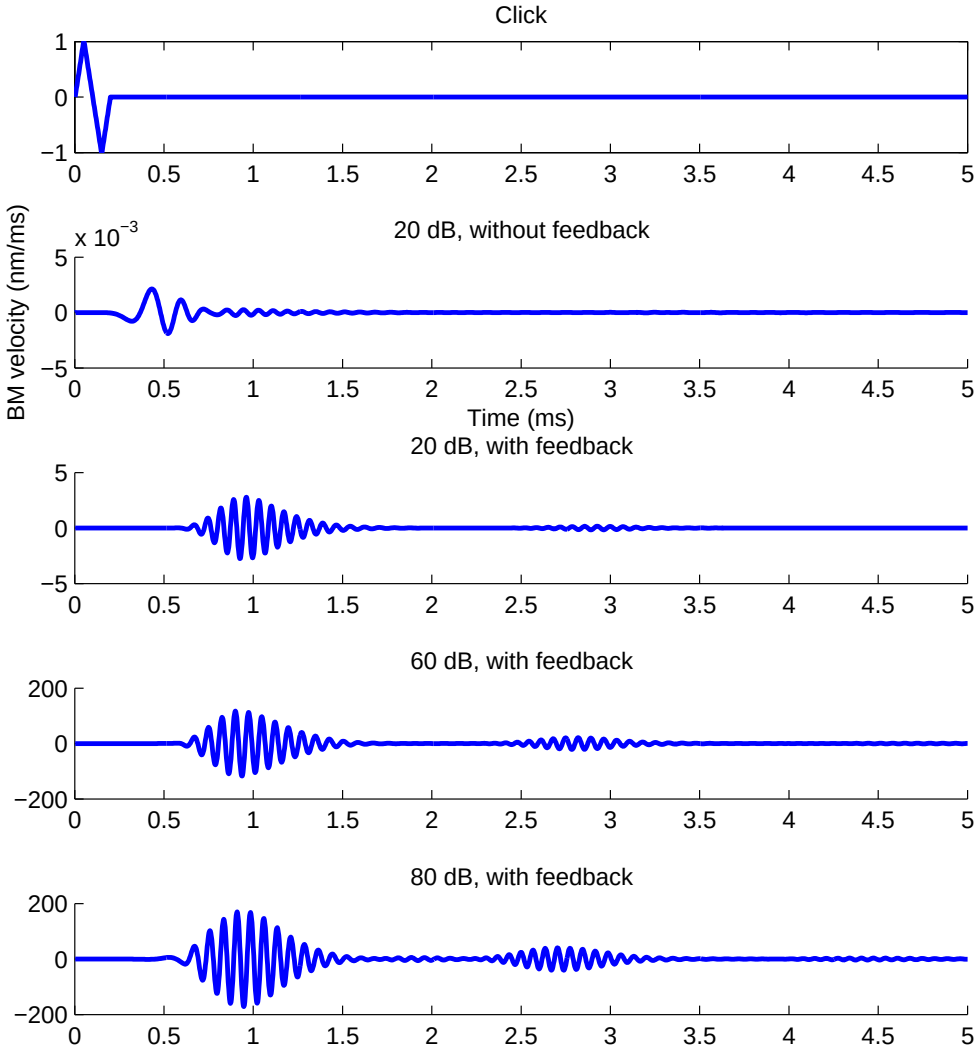

Figure 4.13: Transient response to a "click" signal, sampled at $x = 1.5$ cm. Axis labels are shown only in the second graph from the top.

demonstrated by David Kemp in 1978 [38], the cochlea emits sounds back to the ear canal in response to audio inputs. Such a phenomenon is believed to originate from the amplification mechanisms in cochlea, and is only observed in healthy cochlea. Given the difficulties to conduct experiments on live cochlea, numerical simulation with the temporal-spatial cochlea model may provide means to investigate the elusive mechanisms behind *in vivo* cochlear behaviors.

Compressive Growth

Figure 4.14 illustrates the compressive growth phenomenon in the temporal-spatial model. Pure-tone signal of different sound pressure level as used as the input of the system, the BM velocity is surveyed throughout the BM boundary after a static state has reached. Frequency 2.25, 4.5, 9, and 18 kHz are used for this experiment.

It can be observed from the graph that all the BM profiles demonstrates a peaked curve with the peak located around the corresponding CP. However, with the increase of input sound pressure level, the peak location becomes less sharp as BM segments away from the CP has greater gain in velocity than that of the CP. The curves reveal that the cochlea model possess greater frequency selectivity when a lighter sound is present, and the sensitivity grows duller with the increase of sound pressure level. The experiment results comply with the finding in numerical experiments of [39], and the physiological measurements in [57].

Two-tone Suppression

Figure 4.15 shows the effects of two-tone suppression observed in the temporal-spatial model. The input comprises of two pure-tone signals: the probe tone at 18.8 kHz, and the suppressor tone at 22.9 kHz. The signal is created with different combination of sound pressure levels, and the BM velocity is measured after the static state has reached. Measuring site is at $x = 1.25$ cm, the corresponding peak for the probe tone. It can be observed that when a strong suppressor is present, the BM response for the probe tone is generally weaker. The suppression effect diminishes with the increase of probe tone level. This result qualitatively agrees with the physiological data in Figure 2.11.

In conclusion, the solutions of the temporal-spatial cochlear model is presented. Experiments are conducted with the focus on comparing model performance with previously reported numerical results and physiological data. In general, the simulation results agree qualitatively with past works and the results of the spatial cochlear

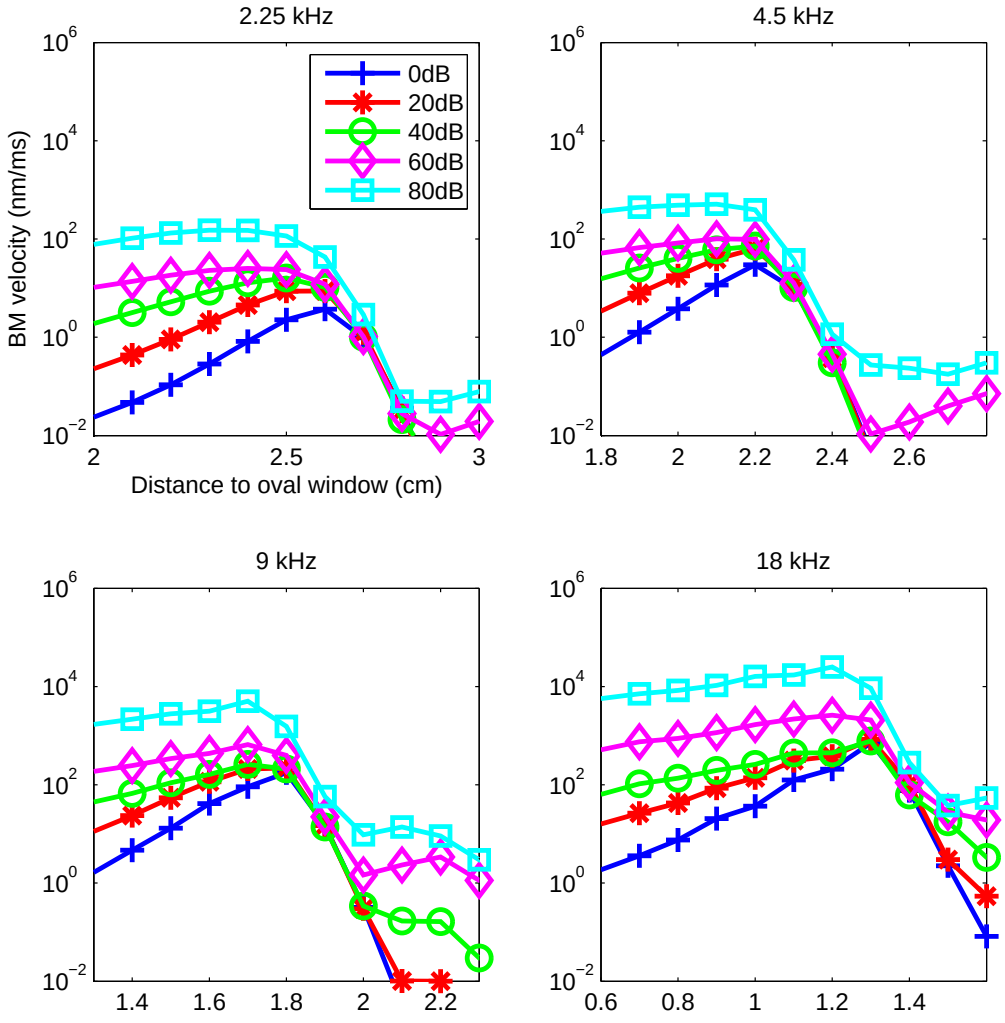

Figure 4.14: Compressive growth of model response for increasing sound level. Signals of 2.25, 4.5, 9, and 18 kHz are used as input. Legend and axis labels are shown only in the top-left graph.

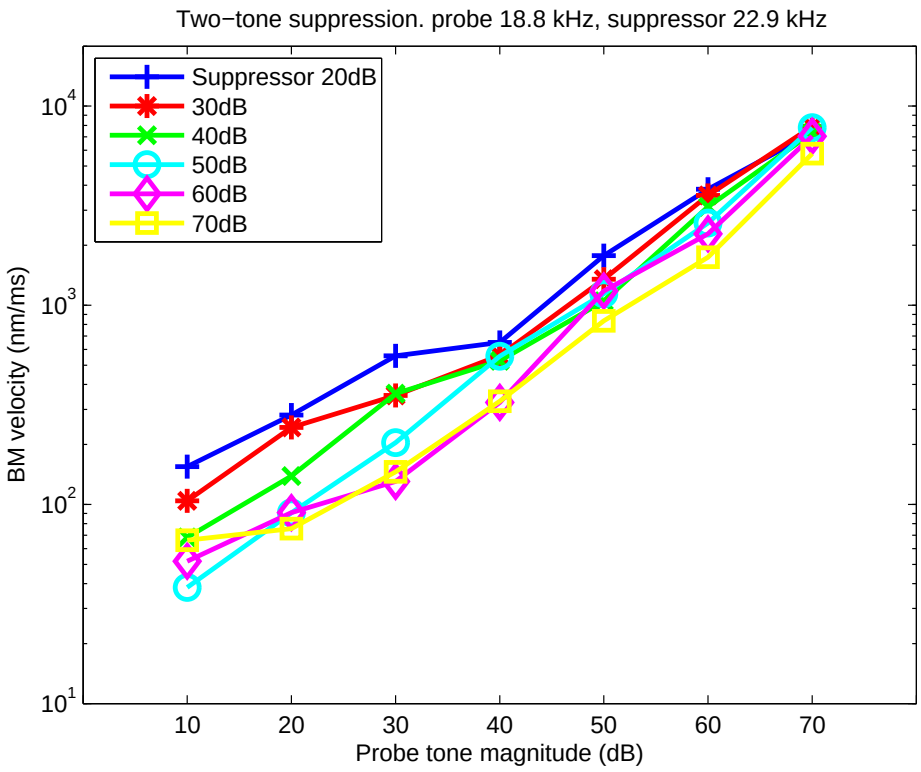

Figure 4.15: Two-tone suppression experiment with probe tone 18.8 kHz and suppressor tone 22.9 kHz. BM velocity is measured at $x = 1.25$ cm.

model, but a large discrepancy is found in the location of CP for input frequencies. We believe that the difference is due to the solution techniques we employ. Because the exponential–linear relationship is preserved for the frequency–location map, the discrepancy can be easily remedied with the change of system parameters. A thorough parameter adjustment may be conducted so that the cochlear model agrees better with existing medical data. The simulation results of a transient "click" input also suggest an possible approach to study the mechanism behind oto-acoustic emissions.

Chapter 5

Future Work

Future development of this work can be carried out in the following aspects:

First, proving the convergence of the temporal-spatial model. The temporal-spatial model used in this work is identical to the one used in [39], while the solution technique is different. In [39] the temporal-spatial model was solved using FDM, for which the convergence of the temporal simulation is proved. Although our own solution gives results comparable to that of simulation results and physiological data, the proof of convergence for simulation is still lacking, yet it is required to underpin the correctness of the solution. Proving the convergence for the solution scheme also help optimizing the simulation results by selecting appropriate time-step size which guarantees both convergence and fast simulation.

Second, studying the location of CP in the temporal-spatial model with changes in the OHC active feedback factor. In our temporal-spatial solutions, the location of CP appears to be offset by the addition of the OHC feedback factor, which deviates from past simulation results and physiological data. We suspected the change of CP is due to the complex fluid interaction in the two dimensional domain, which can be further investigated using analytical and numerical methods. Likewise, values of parameters such as the OHC tilt distance, OHC feedback structure, etc., are asserted so as to conduct temporal simulations. Relationships between simulation results and the OHC feedback parameters can be further deduced.

Third, solving more complex models. This thesis demonstrates general procedures to solve two types of cochlear models. The solution technique and the properties we discover can be extended to the solution of other cochlear models which encompass more complex features. For example, a three dimensional cochlear model may offer performance closer to the biological cochlea. The spiral shape of the cochlea, and the feed-backward factors [14] can be incorporated to better represent the actual structure

of the cochlea.

Fourth, developing a signal processing model from the model simulations. One ultimate goal of the cochlear study is to create a signal processing tool which gives similar performance to the human cochlea, so that better hearing aids and audio processing applications can be developed. The temporal-spatial model demonstrates desirable signal processing ability of analyzing audio signals of complex composition. However, the simulation time is unacceptably long for signal processing applications, for the analysis of a 40 millisecond signal requires 10 minutes of computation time (*MATLAB* codes on a 2000 MHz AMD processor). The temporal-spatial model and its solution scheme can be potentially simplified, so that similar simulation results can be obtained with shorter simulation time. Computational techniques such as domain decomposition and parallel computing may also be employ to speed up the analysis process.

Chapter 6

Conclusion

Two cochlear models and their numerical solutions have been presented in this thesis. For the spatial cochlear model, collocation schemes of various basis functions are proposed to obtain solutions. As is observed in experiment results, the two types of global RBF are not suitable choices for collocation basis functions. Because of the elongated shape of the problem domain, and because the specification of the BM boundary condition with OHC active feedback factor, solutions with global RBF are challenged by severe numerical instability. On the other hand, spline basis functions demonstrate favorable numerical stability. The experiment results appear to be qualitatively consistent with the variation of grid width and boundary conditions. Remarkable agreements are found between the experiment results obtained by cubic spline basis function and physiological data.

The temporal-spatial cochlear model has also been studied. The solutions are obtained by proper discretization in both the spatial and temporal domain, where the cubic spline collocation method and the second order backward difference method are used, respectively. The experiment results deviate from past experiments and physiological data, for the location of CP appeared to be offset by the addition of OHC active feedback factor. We believe the phenomenon is due to our solution scheme, yet further investigation are required to fully determine the source of the effect. Apart from the discrepancy found in CP locations, the experiment results of the temporal-spatial cochlear model agrees qualitatively to past experiments and physiological data. The cochlear model exhibits high frequency selectivity, nonlinear growth of signal magnification, and special phenomena such as otoacoustic emission and two-tone suppression that are typically found in live cochlea.

This work has presented a general procedure for solving cochlear models. The results and techniques can be extended to complex cochlear models that incorporate

more biological features. The experiment results of the temporal-spatial cochlear model can be used in development of a cochlear-based, audio signal processor, which can be employed to construct better hearing aids and audio processing applications.

Bibliography

[1] Jont Allen. Cochlear modeling. *ASSP Magazine, IEEE*, 2(1):3–29, 1985.

[2] William E Brownell, Charles R Bader, Daniel Bertrand, and Yves de Ribaupierre. Evoked mechanical responses of isolated cochlear outer hair cells. *Science*, 227(4683):194–196, 1985.

[3] Richard L Burden and J Douglas Faires. Numerical analysis. 2001. *Brooks/Cole, USA*.

[4] Yidao Cai and C Daniel Geisler. Suppression in auditory-nerve fibers of cats using low-side suppressors. i. temporal aspects. *Hearing research*, 96(1):94–112, 1996.

[5] Christina C Christara. Quadratic spline collocation methods for elliptic partial differential equations. *BIT Numerical Mathematics*, 34(1):33–61, 1994.

[6] Charles C.K. Chui. *Multivariate splines*. SIAM, 1988.

[7] Dallos, He, Evans, and Clark. Dynamic characteristics of outer hair cell motility. In *Biophysics of hair cell sensory systems*, pages 167–174. World Scientific, 1993.

[8] Peter Dallos. *The Mechanics and biophysics of hearing: proceedings of a conference held at the University of Wisconsin, Madison, WI, June 25-29, 1990*, volume 87. Springer-Verlag, 1990.

[9] Peter Dallos. The active cochlea. *J neurosci*, 12:4575–4585, 1992.

[10] Peter Dallos. Overview: cochlear neurobiology. In *The cochlea*, pages 1–43. Springer, 1996.

[11] Peter Dallos and Mary Ann Cheatham. Nonlinearities in cochlear receptor potentials and their origins. *The Journal of the Acoustical Society of America*, 86(5):1790–1796, 1989.

[12] Egbert de Boer. On equivalence of locally active models of the cochlea. *The Journal of the Acoustical Society of America*, 98(3):1400–1409, 1995.

[13] Egbert De Boer. Mechanics of the cochlea: modeling efforts. In *The cochlea*, pages 258–317. Springer, 1996.

[14] Egbert de Boer and Alfred Nuttall. Properties of amplifying elements in the cochlea. In *Biophysics of the Cochlea. From Molecules to Models*, volume 1, pages 331–342, 2003.

[15] Egbert De Boer and Max Viergever. Validity of the liouville-green (or wkb) method for cochlear mechanics. *Hearing research*, 8(2):131–155, 1982.

[16] Li Deng. Processing of acoustic signals in a cochlear model incorporating laterally coupled suppressive elements. *Neural Networks*, 5(1):19–34, 1992.

[17] Stephen J Elliott, Guangjian Ni, Brian R Mace, and Ben Lineton. A wave finite element analysis of the passive cochlea. *The Journal of the Acoustical Society of America*, 133(3):1535–1545, 2013.

[18] N Eze and ES Olson. Basilar membrane velocity in a cochlea with a modified organ of corti. *Biophysical journal*, 100(4):858–867, 2011.

[19] DW Fawcett. W. bloom and dw fawcett: a textbook of histology, 1994.

[20] James L Flanagan. Speech analysis: Synthesis and perception. 1972.

[21] Richard Franke. Scattered data interpolation: Tests of some methods. *Mathematics of computation*, 38(157):181–200, 1982.

[22] Tatsuya Fukazawa. How can the cochlear amplifier be realized by the outer hair cells which have nothing to push against? *Hearing research*, 172(1):53–61, 2002.

[23] C Daniel Geisler. A cochlear model using feedback from motile outer hair cells. *Hearing research*, 54(1):105–117, 1991.

[24] C Daniel Geisler. Two-tone suppression by a saturating feedback model of the cochlear partition. *Hearing research*, 63(1):203–210, 1992.

[25] C Daniel Geisler. A realizable cochlear model using feedback from motile outer hair cells. *Hearing research*, 68(2):253–262, 1993.

[26] C Daniel Geisler. *From sound to synapse: physiology of the mammalian ear*. Oxford University Press, 1998.

[27] C Daniel Geisler and Chunning Sang. A cochlear model using feed-forward outer-hair-cell forces. *Hearing research*, 86(1):132–146, 1995.

[28] Donald D Greenwood. A cochlear frequency-position function for several species–29 years later. *The Journal of the Acoustical Society of America*, 87(6):2592–2605, 1990.

[29] JJ Guinan Jr and WT Peake. Middle-ear characteristics of anesthetized cats. *The Journal of the Acoustical Society of America*, 41(5):1237–1261, 2005.

[30] JL Hall. Two-tone suppression in a nonlinear model of the basilar membrane. *The Journal of the Acoustical Society of America*, 61(3):802–810, 1977.

[31] Rolland L Hardy. Multiquadric equations of topography and other irregular surfaces. *Journal of geophysical research*, 76(8):1905–1915, 1971.

[32] Kenneth G Hill. Basilar membrane motion in relation to two-tone suppression. *Hearing research*, 115(1-2):129–142, 1998.

[33] Allyn Hubbard. A traveling-wave amplifier model of the cochlea. *Science*, 259(5091):68–71, 1993.

[34] Taha SA Jaffer, Hans Kunov, and Willy Wong. A model cochlear partition involving longitudinal elasticity. *The Journal of the Acoustical Society of America*, 112(2):576–589, 2002.

[35] Edward J Kansa. Multiquadrics–a scattered data approximation scheme with applications to computational fluid-dynamics–i surface approximations and partial derivative estimates. *Computers & Mathematics with applications*, 19(8):127–145, 1990.

[36] Edward J Kansa. Multiquadrics–a scattered data approximation scheme with applications to computational fluid-dynamics–ii solutions to parabolic, hyperbolic and elliptic partial differential equations. *Computers & mathematics with applications*, 19(8):147–161, 1990.

[37] KD Karavitaki and DC Mountain. Experimental evidence does not support feed-forward outer hair cell forces. In *Association for Research in Otolaryngology MidWinter Meeting Abstracts*, 1999.

[38] David T Kemp. Stimulated acoustic emissions from within the human auditory system. *The Journal of the Acoustical Society of America*, 64(5):1386–1391, 1978.

[39] Yongsam Kim and Jack Xin. A two-dimensional nonlinear nonlocal feed-forward cochlear model and time domain computation of multitone interactions. *Multiscale Modeling & Simulation*, 4(2):664–690, 2005.

[40] Paul J Kolston and Jonathan F Ashmore. Finite element micromechanical modeling of the cochlea in three dimensions. *The Journal of the Acoustical Society of America*, 99(1):455–467, 1996.

[41] Paul J Kolston, Max A Viergever, Egbert de Boer, and Rob J Diependaal. Realistic mechanical tuning in a micromechanical cochlear model. *The Journal of the Acoustical Society of America*, 86(1):133–140, 1989.

[42] Corné J Kros. Physiology of mammalian cochlear hair cells. In *The cochlea*, pages 318–385. Springer, 1996.

[43] Randall J LeVeque, Charles S Peskin, and Peter D Lax. Solution of a two-dimensional cochlea model with fluid viscosity. *SIAM Journal on Applied Mathematics*, 48(1):191–213, 1988.

[44] M Charles Liberman. The cochlear frequency map for the cat: Labeling auditory-nerve fibers of known characteristic frequency. *The Journal of the Acoustical Society of America*, 72(5):1441–1449, 1982.

[45] Kian-Meng Lim. Physical and mathematical cochlear models. 2000.

[46] Kian-Meng Lim and Charles R Steele. A three-dimensional nonlinear active cochlear model analyzed by the wkb-numeric method. *Hearing research*, 170(1):190–205, 2002.

[47] Ram C Naidu and David C Mountain. Longitudinal coupling in the basilar membrane. *Journal of the Association for Research in Otolaryngology*, 2(3):257–267, 2001.

[48] Stephen T Neely. Finite difference solution of a two-dimensional mathematical model of the cochlea. *The Journal of the Acoustical Society of America*, 69(5):1386–1393, 1981.

[49] Stephen T Neely. Mathematical modeling of cochlear mechanics. *The Journal of the Acoustical Society of America*, 78(1):345–352, 1985.

[50] Stephen T Neely. A model of cochlear mechanics with outer hair cell motility. *The journal of the acoustical society of America*, 94(1):137–146, 1993.

[51] Stephen T Neely and Duck O Kim. An active cochlear model showing sharp tuning and high sensitivity. *Hearing Research*, 9(2):123–130, 1983.

[52] KE Nilsen and IJ Russell. Timing of cochlear feedback: spatial and temporal representation of a tone across the basilar membrane. *Nature neuroscience*, 2(7):642–648, 1999.

[53] AL Nuttall and DF Dolan. Two-tone suppression of inner hair cell and basilar membrane responses in the guinea pig. *The Journal of the Acoustical Society of America*, 93(1):390–400, 1993.

[54] Richard S Palais and Robert Andrew Palais. *Differential Equations, Mechanics, and Computation*, volume 51. American Mathematical Soc., 2009.

[55] Anand A Parthasarathi, Karl Grosh, and Alfred L Nuttall. Three-dimensional numerical modeling for global cochlear dynamics. *The Journal of the Acoustical Society of America*, 107(1):474–485, 2000.

[56] William S Rhode. Observations of the vibration of the basilar membrane in squirrel monkeys using the mössbauer technique. *The Journal of the Acoustical Society of America*, 49(4B):1218–1231, 2005.

[57] Luis Robles and Mario A Ruggero. Mechanics of the mammalian cochlea. *Physiological reviews*, 81(3):1305, 2001.

[58] Mario A Ruggero, Luis Robles, Nola C Rich, et al. Two-tone suppression in the basilar membrane of the cochlea: Mechanical basis of auditory-nerve rate suppression. *Journal of Neurophysiology*, 68:1087–1087, 1992.

[59] IJ Russell, AR Cody, and GP Richardson. The responses of inner and outer hair cells in the basal turn of the guinea-pig cochlea and in the mouse cochlea grown in vitro. *Hearing research*, 22(1):199–216, 1986.

[60] IJ Russell and PM Sellick. Low-frequency characteristics of intracellularly recorded receptor potentials in guinea-pig cochlear hair cells. *The Journal of physiology*, 338(1):179–206, 1983.

[61] J Santos-Sacchi. On the frequency limit and phase of outer hair cell motility: effects of the membrane filter. *The Journal of neuroscience*, 12(5):1906–1916, 1992.

[62] Scott A Sarra and Edward J Kansa. Multiquadric radial basis function approximation methods for the numerical solution of partial differential equations. *Adv Comput Mech*, 2, 2009.

[63] Norma B Slepecky. Structure of the mammalian cochlea. In *The cochlea*, pages 44–129. Springer, 1996.

[64] Charles R Steele and Christine E Miller. An improved wkb calculation for a two-dimensional cochlear model. *The Journal of the Acoustical Society of America*, 68(1):147–148, 1980.

[65] Charles R Steele and Larry A Taber. Comparison of wkb and finite difference calculations for a two-dimensional cochlear model. *The Journal of the Acoustical Society of America*, 65(4):1001–1006, 1979.

[66] CR Steele. Behavior of the basilar membrane with pure-tone excitation. *The Journal of the Acoustical Society of America*, 55(1):148–162, 2005.

[67] CR Steele, G Baker, J Tolomeo, and D Zetes. Electro-mechanical models of the outer hair cell. *Biophysics of hair cell sensory systems. World Scientific, Singapore*, pages 207–214, 1993.

[68] Barry Truax. Handbook of acoustic ecology, (cd-rom version). *Computer Music Journal*, 25:93–94, 2001.

[69] Mats Ulfendahl, Shyam M Khanna, Anders Fridberger, Aî Flock, Britta Flock, and Wanje Jager. Mechanical response characteristics of the hearing organ in the low-frequency regions of the cochlea. *Journal of neurophysiology*, 76(6):3850–3862, 1996.

[70] L Voldrich. Mechanical properties of basilar membrane. *Acta oto-laryngologica*, 86(5-6):331–335, 1978.

[71] Luboš Voldřich. Experimental and topographic morphology in cochlear mechanics. In *Mechanics of Hearing*, pages 163–167. Springer, 1983.

[72] Georg Von Békésy and Ernest Glen Wever. *Experiments in hearing*, volume 8. McGraw-Hill New York, 1960.

[73] Xuelin Wang, Liling Wang, Jianjun Zhou, and Yujin Hu. Finite element modelling of human auditory periphery including a feed-forward amplification of the cochlea. *Computer methods in biomechanics and biomedical engineering*, (ahead-of-print):1–12, 2012.

[74] Bo Wen. *Modeling the nonlinear active cochlea*. PhD thesis, University of Pennsylvania, 2006.

[75] Jack Xin. Dispersive instability and its minimization in time-domain computation of steady-state responses of cochlear models. *The Journal of the Acoustical Society of America*, 115(5):2173–2177, 2004.

[76] Jack Xin, Yingyong Qi, Li Deng, et al. Time domain computation of a nonlinear nonlocal cochlear model with applications to multitone interaction in hearing. *Communications in Mathematical Sciences*, 1(2):211–227, 2003.

[77] William A. Yost. *Fundamentals of Hearing, Fifth Edition: An Introduction*. Brill Academic Pub, Leiden, The Netherlands, hardcover edition, 2007.